1-1-2013

Quantifying the Impact of Various Radioactive Background Sources On Germanium-76 Zero-Neutrino-Double-Beta-Decay Experiments

Katarina Leila Mizouni
University of South Carolina

Recommended Citation

Mizouni, K. L.(2013). *Quantifying the Impact of Various Radioactive Background Sources On Germanium-76 Zero-Neutrino-Double-Beta-Decay Experiments.* (Master's thesis). Retrieved from https://scholarcommons.sc.edu/etd/1756

QUANTIFYING THE IMPACT OF VARIOUS RADIOACTIVE BACKGROUND SOURCES ON ^{76}GE $0\nu\beta\beta$-DECAY EXPERIMENTS

By

Katarina Leila Mizouni

International Baccalaureate
Champlain College, Quebec, Canada 1999
Bachelor of Science
University of New Hampshire 2003

Submitted in Partial Fulfillment of the Requirements
for the Degree of Doctor of Philosophy in
Physics and Astronomy
College of Arts and Sciences
University of South Carolina
2013

Accepted by:

Frank T. Avignone III, Major Professor

Richard J. Creswick, Committee Member

Joseph E. Johnson, Committee Member

Todd W. Hossbach, External Examiner

Harry S. Miley, External Examiner

Lacy Ford, Vice Provost and Dean of Graduate Studies

DEDICATION

To my friend Eryk.

ACKNOWLEDGMENTS

There are many people who have inspired me and made this goal possible. First and foremost, I would like to thank my sisters, Dr. Juliette S. Gervais and Sophia K. Mizouni, for their unconditional love and support throughout this journey; my parents, Hedi and Nadya, for raising me with a thirst for knowledge and education; my PhD advisor, Dr. Frank T. Avignone III, for being the best mentor any graduate student could ever wish for; my quantum physics professor, Dr. Richard J. Creswick, for simply being who he is; my good friend, Dr. Todd W. Hossbach, for his eternal guidance, patience and help; my research mentor in undergraduate school, Dr. Marc Lewis McConnell, for believing in me and giving me the confidence I needed; and finally, Dr. Albert Einstein whose baffling theories intrigued me so much I had no other choice but to explore the field of physics.

ABSTRACT

The goal of searching for $0\nu\beta\beta$-decay is to probe an absolute neutrino mass scale suggested by the mass-splitting parameters observed by neutrino oscillation experiments. Furthermore, observation of $0\nu\beta\beta$-decay is an explicit instance of lepton-number non-conservation. To detect the rare events such as $0\nu\beta\beta$-decay, half-lives of the order of 10^{25}-10^{27} years have to be probed. Using an active detector with a large volume, such as hundreds of kilograms of HPGe in the case of MAJORANA, and taking efficient measures to mitigate background of cosmic and primordial origins are necessary for the success of a sensitive $0\nu\beta\beta$-decay experiment.

One focus of the present research is the analysis of data from Cascades, a HPGe crystal array developed at Pacific Northwest National Laboratory in Richland, WA, to determine an upper bound on primordial radiation levels in the cryostat constructed with electroformed copper similar to that electroformed for MAJORANA. It will be shown, however, that there are sources of background much more serious than cryostats in ^{76}Ge experiments. Additionally, experimental applications of the Cascades detector were studied by predicting the sensitivity for a $0\nu\beta\beta$-decay experiment using GEANT4 simulations. Tellurium-130, an even-even nucleus that can undergo $0\nu\beta\beta$-decay to either the ground state or first 0_1^+ excited state of ^{130}Xe, was used as an example. The present work developed techniques that will be used for a number of measurements of $\beta\beta$-decay half-lives for decays to excited states of the daughter isotopes.

CONTENTS

APPENDIX:

LIST OF TABLES

LIST OF FIGURES

CHAPTER 1

INTRODUCTION

1.1. NEUTRINOS

1.1.1. Overview. In the 1920's, the observation of a continuous energy spectrum of electrons emitted in beta-decay (β-decay) left physicists puzzled. This continuous spectrum inferred the emitted electron was sharing its energy with an unknown particle. Pauli explained this discrepancy in 1930 by postulating the existence of a neutral, spin-1/2 particle of small mass that would ensure the conservation of energy, electric charge and angular momentum. He theorized that this particle, which Fermi later dubbed "neutrino" (meaning "little one" in Italian), was emitted with the β-decay electron such that the sum of the energies was always constant [55].

With this hypothesis, the birth of neutrino physics was born. In the years that followed Pauli's theory, nuclear physicists made significant progress in unraveling the properties of neutrinos. In 1932, Fermi proposed his theory of β-decay, which concurred with experimental data [29]. In 1934, Bethe and Critchfield described the role of β-decay in thermonuclear reaction chains powering the stars, showing that a large neutrino flux should be produced by the sun [20]. In 1956, Reines and Cowan confirmed the existence of the electron neutrino by detecting a flux of electron antineutrinos from a nuclear reactor [34]. Other flavors of neutrinos were later discovered and subsequently divided into three groups: the electron-neutrino (ν_e), muon-neutrino (ν_μ), and tau-neutrino (ν_τ). Pontecorvo first suggested the possibility of neutrino oscillations in 1952 and the concept of “mixing” between different neutrino eigenstates in 1962 with Maki.

In 1956, Lee and Yang introduced the idea that weak interactions violated parity. Madame Wu and her coworkers proved this hypothesis to be correct by observing the β-decay of ^{60}Co from oriented nuclei, confirming that all anti-neutrinos were found to be right-handed [75]. This experiment had profound implications. Since a fixed helicity demonstrated that weak interactions violated parity, it was concluded that neutrinos were traveling at the speed of light and were hence massless. This assumption was included in the development of the Standard Model (Glascow 1961, Salam 1968, Weinberg 1967), which unified electromagnetic and weak interactions.

Although observations of the weak neutral currents and intermediate vector bosons Z^0 and $W^{\pm}$ guaranteed the success of the Standard Model, incompleteness in its formulism has been found throughout the years. In the late 1960’s, an experiment led by Davis of the Brookhaven National Laboratory showed that the solar neutrino flux was between 1/3 and 1/2 of the predicted flux [11]. This inconsistency, known as the solar-neutrino problem, was supported by Super-Kamiokande experiments in 1998 by the observation of the oscillation of atmospheric neutrinos [33], followed by Subdury Neutrino Observatory experiments in 2000 [3]. The Kamioka Liquid scintillator Anti-Neutrino Detector (KamLAND) experiment showed later showed that the large mixing angle solution of the solar neutrino problem was strongly favored [25].

The mass of the neutrino has become a crucial topic in particle physics. Neutrino oscillations take place because neutrinos of a definite flavor (ν_e, ν_μ, ν_τ) are not necessarily states of a definite mass (ν_1, ν_2, ν_3) but rather a superposition of the mass eigenstates. To this day, neutrino oscillation experiments have precisely measured the difference in the square of mass eigenvalues of neutrinos that undergo a flavor change, the mixing angles entering oscillation amplitudes, and have placed a lower limit on the absolute mass scale of the neutrino (see Figure 1.1). To obtain the absolute mass scale of the neutrino, it is necessary to turn to other types of experiments, i.e.- tritium endpoint-energy measurements and neutrinoless double-beta decay ($0\nu\beta\beta$-decay). Since $0\nu\beta\beta$-decay experiments already have a sensitivity corresponding to the small neutrino mass scale, they are a much more sensitive probe to the neutrino mass range [44]. In fact, if the mass scale is below ~0.20 eV, $0\nu\beta\beta$-decay experiments could be the only way of measuring it [12]. However, for this process to proceed, neutrinos must be their own anti-particles, i.e., Majorana particles. Additionally, $0\nu\beta\beta$-decay is the only practical experiment that can determine the nature of the neutrino (Dirac or Majorana) and test for lepton-number conservation.

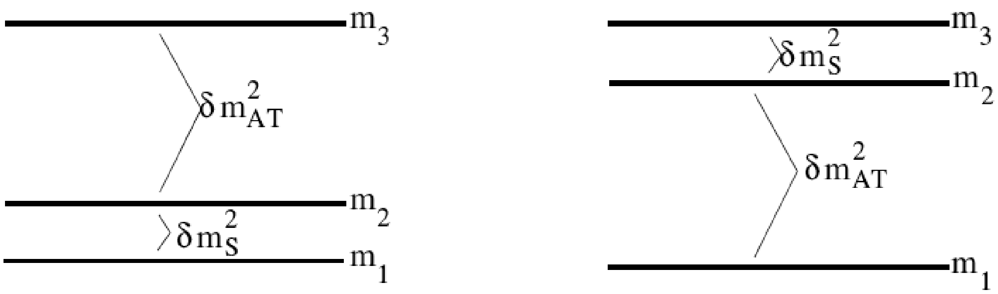

FIGURE 1.1. Normal (left) and inverted (right) mass hierarchies schemes

1.1.2. Dirac and Majorana Neutrinos. Particles differ from their anti-particles through the property of charge. Charged leptons, for instance, have opposite electrical charges from their anti-particles. In the case of electrically neutral particles, other types of charge (for example baryon and lepton number) have to be considered. The idea that some particles could be indistinguishable from their anti-particles was first suggested by Majorana in 1937 [38]. This led to the definition of a Majorana particle; a Dirac particle, on the other hand, is distinguishable from its anti-particle.

In the framework of the Standard Model, a Dirac neutrino has four different states assuming that it has mass and a leptonic charge. These four states consist of a left-handed neutrino (ν_L), which is equivalent under a CPT transformation to a right-handed anti-neutrino ($\bar{\nu_R}$). Since the Dirac neutrino has mass, a Lorentz transformation can flip the helicity of ν_L and $\bar{\nu_R}$ to yield two additional states- a right-handed neutrino ν_R and a left-handed anti-neutrino $\bar{\nu_L}$ (refer to Figure 1.2). This quadruplet of states is what defines the Dirac neutrino, ν^D.

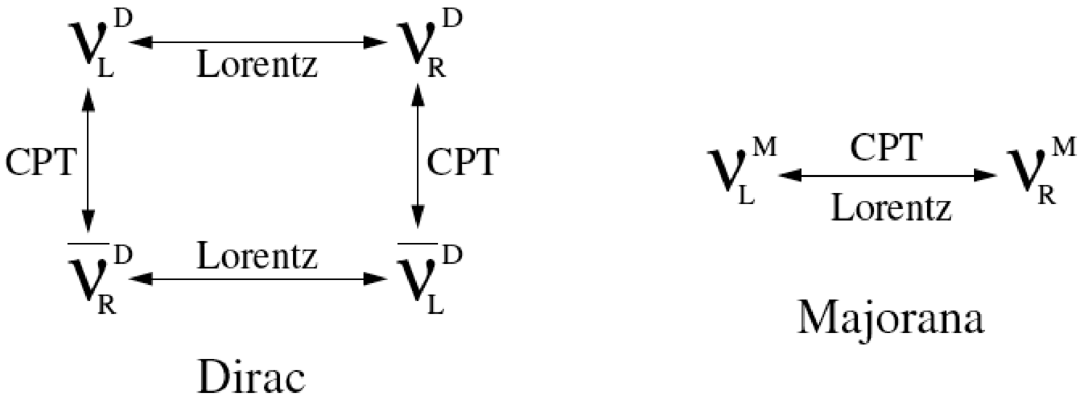

FIGURE 1.2. Transformations between neutrinos: Dirac and Majorana neutrinos are depicted on the left and right respectively [5]

The Majorana neutrino (ν^M), on the other hand, does not carry a leptonic charge, hence it is only composed of two states defined by their opposite helicities. The existence of such a neutrino is appealing for various reasons; for one the Dirac theory cannot explain the large mass difference between the neutrinos and their charged leptons, which belong to the same weak doublet. The Majorana theory, however, can explain this discrepancy through the "see-saw" mechanism- a mechanism first proposed in 1979 by Gell-Mann, Ramond, Slansky and Yanagisawa in which left-handed and right-handed Majorana particles acquire the small and large masses separately rather than form a Dirac neutrino [12].

1.2. DOUBLE BETA-DECAY

1.2.1. Overview. Double beta decay, first suggested by Wigner and reported by Goeppert-Mayer in 1935 [37], is a second-order weak interaction and one of the slowest processes in nature with half-lives usually surpassing 10^{18} years. This process would most probably be observable if single β-decay was not possible energetically or strongly inhibited by an associated large spin change. Complex nuclei become more stable by emitting electrons while the nucleus changes atomic number by two and emits two beta particles:

$$(Z, A) \rightarrow (Z+2, A) + 2\beta^- + 2\bar{\nu}_e \, . \tag{1}$$

To understand $\beta\beta$-decay, we take a look at the parameterization of nuclear mass M as a function of A and Z, known as the Weisäcker or semi-empirical formula [14], [61], [74]. This formula predicts the mass of a nucleus and accounts for the difference between its nucleons and their binding energies as seen in the following equation:

$$\begin{aligned} M(A,Z) &= NM_n + ZM_p + Zm_e - a_v A + a_s A^{2/3} \\ &+ a_c \frac{Z^2}{A^{1/3}} + a_a \frac{(N-Z)^2}{4A} + \frac{\delta}{A^{1/2}} \, , \end{aligned} \tag{2}$$

where M_p is the mass of the proton, m_e is the mass of the electron, M_n is the mass of the neutron, A is the mass number and Z is the atomic number. The volume term (a_v), surface term(a_s), Coulomb term (a_c), asymmetry term (a_a) and pairing term (δ) are all constants.

A nucleus is more stable when it is composed of an even number of nucleons to allow for coupling in pairs. This fact is accounted for in the Weisäcker formula by the pairing term δ. By considering isobars in Equation 2, the nuclear mass M(A,Z) can be plotted as a quadratic function of Z. The pairing term δ is of particular interest because it gives rises to different curves depending on the mass number A. For an odd-odd nucleus, $\delta > 0$. For an odd-even nucleus, $\delta = 0$. Finally, for an even-even nucleus, $\delta < 0$. An example can be seen in Figure 1.3, which plots Equation 2 for the case of A = 76. From this diagram, it can be

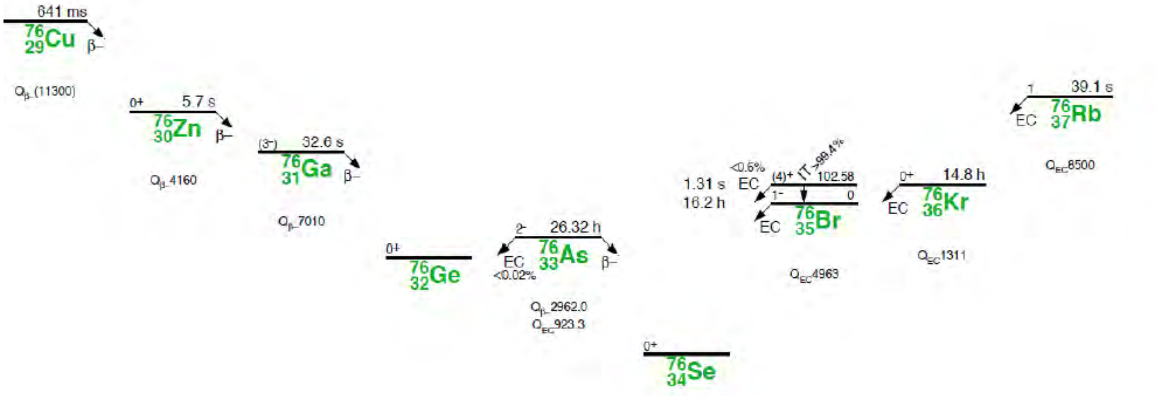

FIGURE 1.3. Mass parabola for A=76 [31]

noted how the decay of ^{76}Ge to ^{76}As is forbidden energetically, and that an odd-odd nucleus always has at least one more strongly bound even-even neighbor such that the nucleus must $\beta\beta$-decay to reach a more stable configuration. In most cases $\beta\beta$-decay proceeds from the 0^+ ground state of a nucleus to the 0^+ ground state of its daughter, however the decay to an excited state (0^+ and 2^+) is also possible energetically [62]. A list of several double-beta candidates can be found in Table 1.1.

1.2.2. Double-Beta Decay Modes. There are three modes of $\beta\beta$-decay that are commonly considered, which can be distinguished by the particles accompanying the emission of the two electrons [28].

The first mode, which was introduced in Equation 1, releases two anti-neutrinos and electrons while conserving lepton-number symmetry and adhering to the Standard Model (see Feymann diagram in Figure 1.4). This type of $\beta\beta$-decay yields a continuous electron spectrum (see Figure 1.6), in which the position of the maximum peak is determined by the type of isotope undergoing the decay, or more specifically, the Q-value ($Q_{\beta\beta}$) of the isotope which is shared by the two electrons and anti-neutrinos.

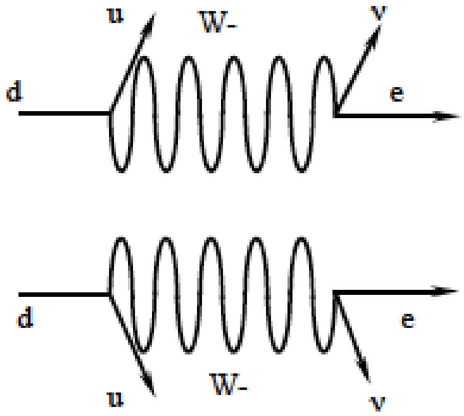

FIGURE 1.4. Feymann diagram of the $2\nu\beta\beta$-decay mode

The second mode ($0\nu\beta\beta$-decay) was first suggested by Furry in 1939 [35] and is forbidden in the Standard Model of electroweak interactions because of its implied lepton-number violation. In this mode (see Figure 1.5 for Feynman diagram), a left-handed neutrino being emitted is absorbed as a right-handed neutrino by the opposite W^- boson, and the decay is therefore neutrinoless. Only two beta particles are emitted:

$$(Z, A) \rightarrow (Z + 2, A) + 2e^- \ . \tag{3}$$

Since the two electrons carry all of the available kinetic energy, $0\nu\beta\beta$-decay

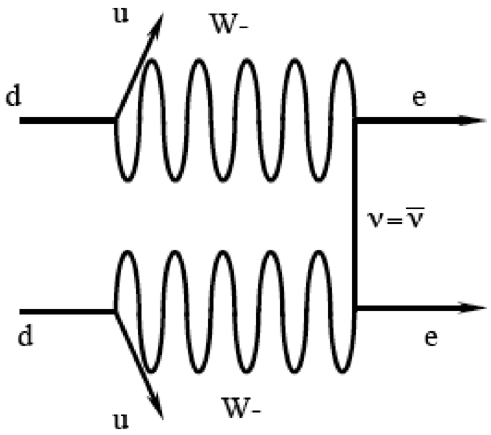

FIGURE 1.5. Feymann diagram of the $0\nu\beta\beta$-decay mode

is expected to yield a monoenergetic line (the sum of both the electron energies) at $Q_{\beta\beta}$ (see Figure 1.6). As discussed previously, observing this decay would establish the neutrino as a Majorana particle and confirm the violation of lepton-number symmetry.

Finally, the third type of double-beta decay ($0\nu\chi\beta\beta$) is also neutrinoless, but is theorized to emit a massless Nambu-Goldstone boson known as the Majoron:

$$(Z, A) \rightarrow (Z + 2, A) + 2e^{-} + \bar{\chi}\ . \tag{4}$$

This Majoron χ is said to be created in the spectrum of possible excitations as a result of the spontaneous breaking of a global symmetry, which results in the Goldstone boson [28]. Refer to Figure 1.7 for the Feynman diagram of this decay.

1.2.3. Extracting the Neutrino Mass. The objective of a $0\nu\beta\beta$-decay experiment is to measure the rate at which the parent nucleus decays to the daughter, i.e. the half-life $\mathrm{T}^{0\nu}_{1/2}$ of the decay. This rate can be expressed as follows [52]:

$$[T^{0\nu}_{1/2}]^{-1} = G_{0\nu}(Q_{\beta\beta}, Z)|M_{0\nu}|^{2}\langle m_{\beta\beta}\rangle^{2}\ , \tag{5}$$

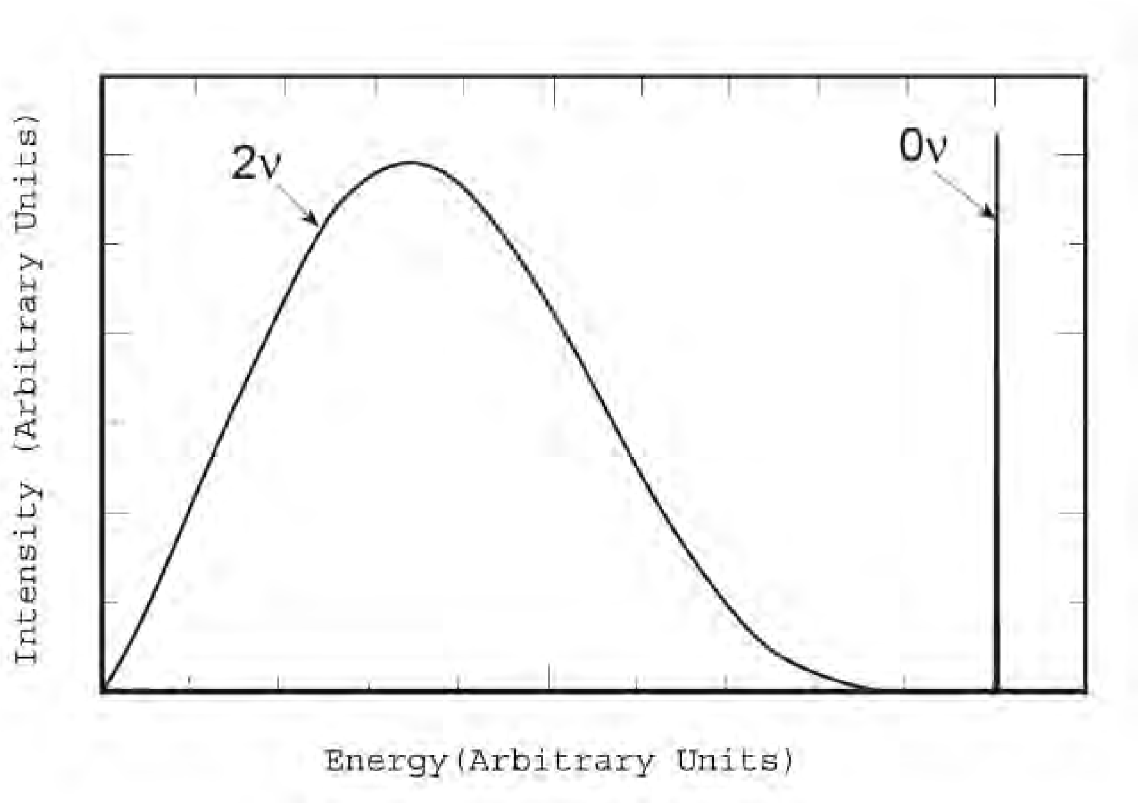

FIGURE 1.6. $2\nu\beta\beta$ and $0\nu\beta\beta$-beta spectra for an arbitrary isotope [44]

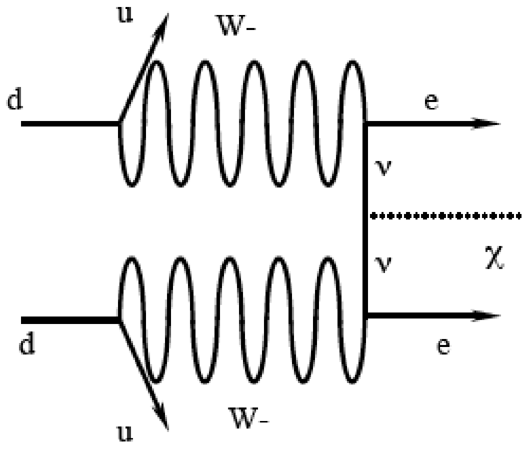

FIGURE 1.7. Feymann diagram of the $0\nu\beta\beta$-decay mode

where $G_{0\nu}(Q_{\beta\beta}, Z)$ is the phase space factor for the emission of the two electrons, $M_{0\nu}$ is the 0ν nuclear matrix element, and $\langle m_{\beta\beta}\rangle$ is the effective Majorana mass of the electron neutrino given by:

$$\langle m_{\beta\beta}\rangle \equiv |\sum_k m_k U_{ek}^2| \tag{6}$$

$$\langle m_{\beta\beta}\rangle = m_1|U_{e1}|^2 + m_2|U_{e2}|^2 e^{i(\alpha_2-\alpha_1)} + m_3|U_{e3}|^2 e^{i(-\alpha_1-2\delta)} , \tag{7}$$

where U_{ek} is the neutrino mixing matrix (also known as the Maki-Nakagawa-Sakata matrix), which describes the probability that a neutrino of a given flavor can be found in one of the three possible mass eigenstates. The imaginary terms $e^{i(\alpha_2-\alpha_1)}$ and $e^{i(-\alpha_1-2\delta)}$ introduce two phase angles, α and δ. The phase factor α is present if the neutrino is a Majorana particle, while the phase factor δ is present if CP is violated [10].

Equation 5 can be used to combine the nuclear model-dependent parameters into the nuclear structure function F_N, given by:

$$F_N = G_{0\nu}(Q_{\beta\beta}, Z)|M_{0\nu}|^2 m_e^2 , \tag{8}$$

and a simplified expression for the effective neutrino mass can be written as:

$$\langle m_{\beta\beta}\rangle = m_e[T_{1/2}^{0\nu} F_N]^{-1/2} . \tag{9}$$

The neutrino mass can then be extracted from an experimental measurement by making use of Equation 9. Table 1.1 lists eleven $\beta\beta$-decay candidates along with the best-reported limits for $\mathrm{T}_{1/2}^{0\nu}$ and $\langle m_{\beta\beta}\rangle$.

As can be seen in Equation 5, $0\nu\beta\beta$-decay rates and in their associated effective Majorana masses of the electron neutrino rely on the precise knowledge of transition nuclear matrix elements. Unfortunately, nuclear matrix elements are calculated and often have differing values depending on the model used for the calculation. A renewed interest in the Shell Model has recently emerged

TABLE 1.1. Candidate $\beta\beta$-decay isotopes with their theoretical end-point energies, limits for $T^{0\nu}_{1/2}$ and $\langle m_{\beta\beta}\rangle$values [10].

$\beta\beta$-Decay Candidates	$Q_{\beta\beta}$ (keV)	$T^{0\nu}_{1/2}$ (yrs)	$\langle m_{\beta\beta}\rangle$ (eV)
^{48}Ca	4271	$> 1.4 \times 10^{22}$	<7.2-44.7
^{76}Ge	2039	$> 1.9 \times 10^{25}$	< 0.35
^{76}Ge	2039	$(2.23^{+0.44}_{-0.31}) \times 10^{25}$	0.32 ± 0.03
^{76}Ge	2039	$> 1.57 \times 10^{25}$	$< (0.33 - 1.35)$
^{82}Se	2995	$> 2.1 \times 10^{23}$	<(1.2-3.2)
^{100}Mo	3034	$> 5.8 \times 10^{23}$	<(0.6-2.7)
^{116}Cd	2802	$> 1.7 \times 10^{23}$	<1.7
^{128}Te	868	$> 7.7 \times 10^{24}$	<(1.1-1.5)
^{130}Te	2527	$> 3.0 \times 10^{24}$	<(0.41-0.98)
^{136}Xe	2479	$> 4.5 \times 10^{23}$	<(0.8-5.6)
^{150}Nd	3367	$> 3.6 \times 10^{21}$	

due to the fast development of computer technologies, while the application of the quasiparticle random phase approximation (QRPA) method and its extensions have allowed for much progress to be made over the past few years. However, uncertainties and contradictions in the nuclear matrix elements today still present a difficult problem to overcome for the interpretations of $0\nu\beta\beta$-decay results. This remains one of the more important motivations behind measuring $2\nu\beta\beta$-decay transitions, which help test the calculations of the nuclear matrix elements in models similar to those used to extract the absolute neutrino mass from $0\nu\beta\beta$-decay experiments [64].

1.3. THE MAJORANA PROJECT

1.3.1. Experimental Techniques. The experimental signatures for $\beta\beta$-decay are in principle very clear. A continuous spectrum with a well-defined shape will result from $2\nu\beta\beta$-decay, while the observation of a mono-energetic peak at the $Q_{\beta\beta}$ value is expected in the case of $0\nu\beta\beta$-decay. However, these characteristics can yield difficult identification. In general, several considerations have to be made when designing an experiment to search for the $\beta\beta$-decay of an isotope. These considerations are as follows:

- Since a peak identifying $0\nu\beta\beta$-decay is superimposed on a continuum, the detector must have excellent energy resolution. Not only does this increase the signal-to-background ratio for the peak, but it also ensures that events in the $2\nu\beta\beta$-decay tail do not extend into the 0ν peak and contribute to an irreducible background [9].
- Experimental backgrounds from primordial and cosmogenic activity must be strictly controlled so as not to interfere with the identification of a candidate signal.
- Since cosmogenic activity can build up in the shielding, detector and source over time through nuclear reactions of cosmic-ray neutrons and their secondary products, building the detector underground will greatly reduce this background.
- Finally, it is advantageous to minimize the detector size, since the total activity of an impure material will scale with volume. This can be accomplished by designing an “active” detector, which features using the source as the detector itself [38].

1.3.2. First-Generation $0\nu\beta\beta$-Decay Experiments. Many experiments have been designed to search for $\beta\beta$-decay, however they can be categorized into three approaches: geochemical, radiochemical and direct counting measurements [27]. Radiochemical and geochemical experiments consist of searching for the presence of the daughters of $\beta\beta$-decay in old geological samples, or looking for isotopic anomalies in these $\beta\beta$-decay daughters [38]. While these experiments have an increased sensitivity due to their long exposure time, they cannot distinguish between the different modes of $\beta\beta$-decay and therefore do not contribute to new advances in the field of particle physics.

Direct counting measurements can distinguish between the $0\nu\beta\beta$ and $2\nu\beta\beta$ modes and consist of measuring the $\beta\beta$-decay energy and spectral shape while sometimes allowing for event reconstruction. There are two distinct approaches to these types of experiments: passive detectors, in which the source is distinct from the detector, and active detectors, which have been previously explained as building the detector with a material already containing the $\beta\beta$ active nuclei [38]. So far, direct experiments have consisted of various conventional counters, such as solid state devices (germanium spectrometers and silicon detector stacks), gas counters (time projection chambers, ionization and multiwire drift chambers) and scintillators (crystal scintillators and stacks of plastic scintillators) [59]. Examples of $\beta\beta$-emitters measured in direct counting experiments include ^{48}Ca, ^{76}Ge, ^{96}Zr, ^{82}Se, ^{100}Mo, ^{116}Cd, ^{130}Te, ^{136}Xe and ^{150}Nd [59].

Neutrinoless double-beta decay is even rarer than the $2\nu\beta\beta$ mode with half-lives that are predicted to range higher than 10^{25} years. Consequently, experiments aiming to measure these half-lives and their associated electron neutrino masses have to be designed with a very high sensitivity. Much progress has been made throughout the years on placing limits on the electron neutrino mass for numerous isotopes (see Table 1.2). In particular, the Heidelberg-Moscow (HM) and International Germanium Experiment (IGEX) experiments have placed a limit for $\langle m_{\beta\beta} \rangle$ ranging from (0.3 - 1.0 eV) taking into account uncertainties resulting from the variety in the values of the nuclear matrix elements [38]. By using several kilograms of 86%-enriched ^{76}Ge in a conventional, close-ended coxial geometry, both experiments achieved extremely low levels of background by operating deep underground, using radiopure materials with active and passive shielding, and employing pulse-shape analysis techniques that reduced the background rate to approximately 0.1 counts (keV-kg-y)$^{-1}$ [71].

Next-generation strategies aim to push down limits on the electron neutrino mass by more than an order of magnitude. To reach these goals, additional techniques to suppress background events have to be developed on top of excellent energy resolution and large detector size, while again operating the experiment underground [71].

TABLE 1.2. Summary of current and proposed double-beta decay experiments. The right arrow indicates the projected sensitivity [32].

Experiment	Isotope	Technique	Mass (kg)	Enriched	$Q_{\beta\beta}$ (MeV)	$\langle m_{\beta\beta} \rangle$ (eV)
HDSM	^{76}Ge	Ge crystals	9.9	86%	2.04	<0.40
IGEX	^{76}Ge	Ge crystals	9	86%	2.04	<0.44
UCI	^{82}Se	TCP foils	0.014	97%	2.99	<7.7
ELEGANT	^{100}Mo	Drift chambers	0.20	94.5%	3.03	<2.7
Kiev	^{116}Cd	$CdWO_4$ crystals	0.09	83%	2.8	<3.3
Missouri	^{128}Te	Geochemical	Te Ore	No	0.87	<1.5
Milano	^{130}Te	Cryogenic TeO_2	2.3	No	2.53	<2.6
UCI	^{150}Nd	TCP foils	0.015	91%	3.37	<7.1
NEMO3	^{82}Se, ^{100}Mo, ^{116}Cd, ^{150}Nd	Drift chambers	Varies	Yes	Varies	→0.1
Cuoricino	^{130}Te	Cryogenic TeO_2	2.3	No	2.53	→0.1
MAJORANA	^{76}Ge	Ge crystals	500	86%	2.04	→0.02
CAMEO	^{82}Se, ^{100}Mo ^{116}Cd	BOREXINO CTF	1 each	Yes	Varies	→1
MOON	^{100}Mo	Scintillator foils	3400	No	3.03	→0.02
CUORE	^{130}Te	Cryogenic TeO_2	210	No	2.53	→0.02
EXO	^{136}Xe	TPC	1000-10000	Yes	2.47	→0.3-→0.01
EXO-200	^{136}Xe	TPC	200	Yes	2.47	→1.5
DBCA-II	^{150}Nd	Drift chambers	18	Yes	3.37	→0.05

1.3.3. Second-Generation $0\nu\beta\beta$-Decay Experiments. The idea of using HPGE detectors enriched to 86% in ^{76}Ge to yield a substantially higher detection efficiency was first suggested by Ettore Fiorini [30].

The originally proposed MAJORANA project planned to search for the $0\nu\beta\beta$-decay of ^{76}Ge to ^{76}Se in high-purity Ge-diode active detectors with a technique improved by advances in signal processing, detector design, and controlling intrinsic and external backgrounds [69], [68], [70]. The proposed experiment consists of an array of Ge detectors isotopically enriched to 86% in ^{76}Ge with a total mass of hundreds of kilograms, such that a sensitivity within the quasi-degenerate neutrino mass region can be reached within a reasonable time frame. These HPGe crystals measure 62 mm in diameter, are 70 mm long, have a mass of 1.1 kg each, and will be housed in an ultra-low background electroformed cryostat cooled by liquid nitrogen. The configuration of the MAJORANA experiment is not yet fixed, however many have been evaluated based on their cryogenic performance and design to maximize background reduction and rejection [9]. Figure 1.8 depicts one the several proposed configurations consisting of 57 1-kg HPGe detectors arranged in an electroformed-copper cryostat.

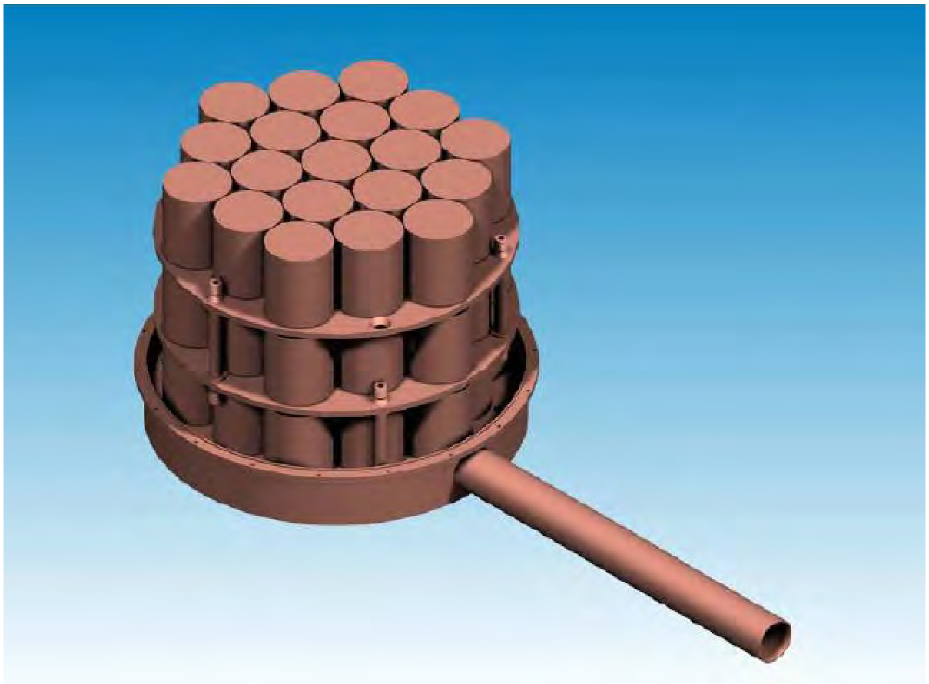

FIGURE 1.8. One of the proposed MAJORANA modules [9]

To probe the inverted mass hierarchy of the neutrino, the experiment must be designed to reach sensitivities to the order of 10^{26} - 10^{27}years. An equation measuring the discovery potential or sensitivity of a next-generation $0\nu\beta\beta$-decay experiment can be derived by requiring that:

$$C_{\beta\beta} = n_\sigma \sqrt{B}\ , \tag{10}$$

where $C_{\beta\beta}$ is the number of $0\nu\beta\beta$-decay events, n_σ is the desired standard deviation of the measurement, and B is the number of background counts in the region of interest (ROI). The following expression can then be obtained [9]:

$$T^{0\nu}_{1/2}(n_\sigma) = \frac{4.16 \times 10^{26} y}{n_\sigma} \left(\frac{\varepsilon a}{W}\right) \sqrt{\frac{Mt}{b\Delta E}}\ , \tag{11}$$

where ϵ is the event-detection efficiency, a is the isotopic abundance in the source material, W is the molecular weight of the source material (g/mol), M is the total mass of the source (kg), b is the background rate in counts (keV-kg-y)$^{-1}$, and ΔE is the spectral resolution of the experiment in keV. The factor 10^{26} results from Avogrado's number and from expressing the relation as a half-life (years).

As it can be seen in Equation 11, the parameters to optimize the experiment consist of a large source mass with a high isotopic abundance to account for the rarity of the decay, a long-enough exposure time, a high event detection efficiency, and an excellent energy resolution, which is essential for the distinction between $2\nu\beta\beta$ and $0\nu\beta\beta$ events. Lastly, a low background in the ROI (2039.006 keV [26]) remains the most crucial point to address for a successful next-generation $0\nu\beta\beta$-decay experiment.

The $0\nu\beta\beta$-decay signal rate is expected to be extremely low due to the long predicted half-life. Therefore, the only plausible way of obtaining a large-enough signal-to-noise ratio is to reduce the background from all sources [17]. These different sources can be categorized as follows in descending order of magnitude: 1) primordial radioactivity in the laboratory environment, 2) cosmic radiation, 3) primordial and manmade radioactivity in system components, 4) natural radon in the air, 5) ^{210}Pb in modern lead shielding, 6) cosmogenic radioactivities in system components, and 7) $2\nu\beta\beta$-decay of ^{76}Ge [17]. Backgrounds produced by cosmic-rays are found in the germanium crystal (^{54}Mn, ^{57,58}Co, ^{65}Zn, ^{68}Ge) and in the copper used in the cryostat and for shielding (^{54}Mn, ^{56,57,58,60}Co, ^{59}Fe). Primordial contamination, on the other hand, consist of the ^{238}U and ^{232}Th decay chains and bremsstrahlung radiation from the ^{210}Pb daughter ^{210}Bi [44]. This type of radiation is found in the cryostat, internal electronics components, and shielding materials. Cosmogenic and primordial backgrounds can both decay by emitting positrons or gamma rays with high-energy values above the $0\nu\beta\beta$-decay ROI, risking contamination in the ROI by compton-scattered events. Methods to mitigate these backgrounds include the use of ultra-pure materials, shielding, depth underground, good energy resolution, detector granularity, pulse-shape analysis, detector design and time correlations [69], some of which will be discussed thoroughly in Chapter 2. In particular, sophisticated copper electroforming techniques have been developed to ensure the use of ultra-low background material in building the copper cryostat.

Copper is an ideal element to use for building ultra-low background materials [69]. This is due to its excellent physical, chemical and electronic properties, as well as the fact it only has one relatively long-lived radioisotope. However efforts must still be made to ensure it is not contaminated by radioactive impurities or cosmic-ray-generated radioisotopes. These efforts include producing ultra-pure copper by an electroforming process deep underground for use in MAJORANA [69], which will be discussed further in Chapter 2. The total estimated background rate for the MAJORANA experiment is projected to be 1.6

counts/ROI/(ton-yr), however based on simulations and assay capabilities, a rate of 1 count/ROI/(ton-yr) could possibly be achieved [69].

The MAJORANA demonstrator, a project developed to establish the feasibility of constructing a larger tonne-scale experiment with such a low-background rate, is currently under construction at the Stanford Underground Laboratory in Lead, South Dakota. Due to the need for rejecting multiple energy depositions and differentiating efficiently between multiple scattering gamma backgrounds and single-site $0\nu\beta\beta$-decays, the MAJORANA demonstrator will use p-type point contact germanium detectors [45]. The demonstrator will begin with the construction of a prototype cryostat consisting of a few detectors comprised of non-enriched germanium. Eventually these will be replaced by one, then by two low-background cryostats with a maximum sensitive configuration of 40 kg of germanium, 30 kg of which will be enriched to $>86\%$ in ^{76}Ge [2]. In order to achieve this, the MAJORANA collaboration has developed its own method for checking the purity of the GeO_2 powder and reducing it to a metal that is zone refined (see Section 2.3.2 of Chapter 2 for a discussion on zone refinement) to a resistivity of < 47 Ohm-cm, which indicates a low concentration of electrically active impurities ($\sim 10^{13}$cm^{-3}) [2]. To test the process, 29 kg of natural isotopic abundance GeO_2 was obtained and reduced to metal with a yield of 98.3%. It was fabricated into two point-contact detectors, both of which have excellent energy resolution. In September 2011, 29 kg of GeO_2 enriched to 86% in ^{76}Ge arrived from Russia. It was reduced to metal, zone refined and sent to ORTEC Inc. in Oak Ridge, Tennessee where it has been made into point-contact detectors. On October 23 2012, the final 32.6 kg of enriched GeO_2 arrived from Russia and was reduced and zone refined just prior to this writing. While not being processed, all of the enriched GeO_2, germanium metal and detectors, detector pieces and scraps are stored in an underground facility in the Cherokee Caverns near Oak Ridge. This location has an overburden of 100 meters of water equivalent (m.w.e.) to shield against cosmogenic backgrounds [2].

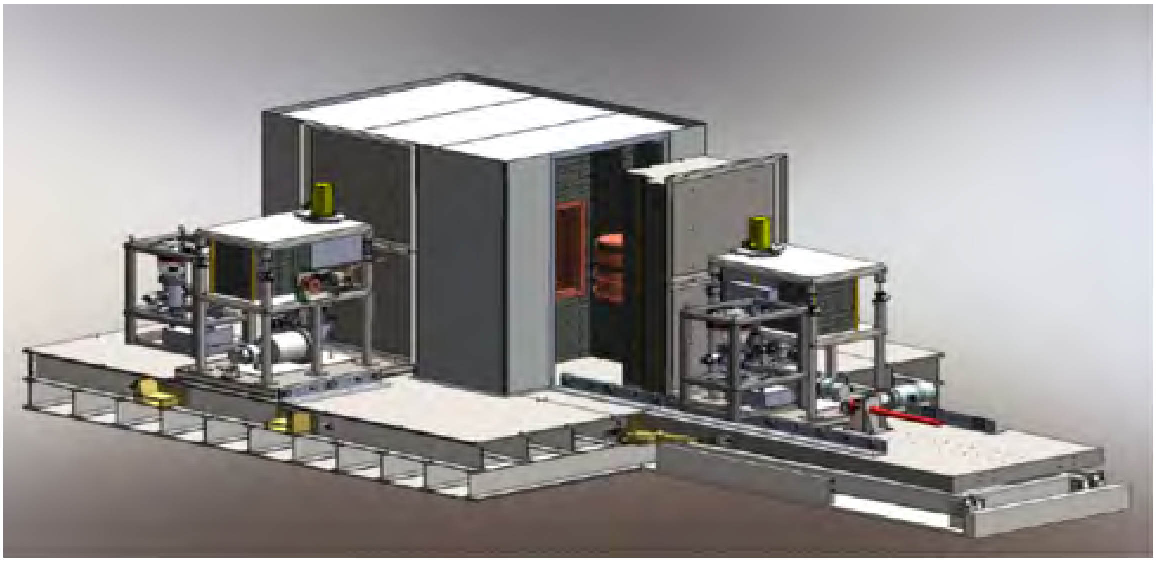

FIGURE 1.9. The MAJORANA Demonstrator [2]

The goals of the MAJORANA demonstrator are to achieve a background rate of 4 counts/ROI/(ton-yr), which Monte-Carlo simulations predict will result in a background rate of 1 count/ROI/(ton-yr) for the final MAJORANA experiment. Out of this estimated 4 counts/ROI/(ton-yr) rate, the copper cryostat is expected to contribute 0.11 counts/ROI/(ton-yr) or 7% of the total background [69]. To meet this goal, very low levels of impurities caused by primordial contamination can be present in the copper. More specifically, the levels of ^{232}Th cannot exceed 0.3 μBq/kg, which translates as an activity of 0.1 μBq/kg for ^{208}Tl (the source of a problematic 2615 keV γ-ray line) [69].

Investigating the efficiency of background mitigation methods to reduce natural levels of ^{238}U and ^{232}Th in $0\nu\beta\beta$-decay ^{76}Ge experiments is one of the motivations behind this dissertation. Simulations of the ^{238}U and ^{232}Th chains were performed to predict levels of primordial radiation in the copper cryostat of Cascades: a HPGe array constructed at Pacific Northwest National

Laboratory (PNNL), consisting of 14 HPGe crystals housed in two cryostats made of copper electroformed with the same process that will be used in the MAJORANA experiment [48]. These simulations were compared to actual background data from Cascades to analyze the reduction in background due to the copper electroforming process. As discussed later, however, it was discovered through this effort that backgrounds in the copper were not the main sources of background in Cascades. Other construction materials near the detector, as well as the lack of careful low-background construction proticol led to background levels well above those attributable to the copper. Lastly, experimental applications of the Cascades detector were studied by predicting the sensitivity for a $\beta\beta$-experiment using as an example simulations of ^{130}Te, an even-even nucleus that can undergo $2\nu\beta\beta$-decay and $0\nu\beta\beta$-decay to the first 0_1^+ excited state of ^{130}Xe producing three possible γ-cascades as it transitions to the ground state. Tellurium-130 will be discussed more thoroughly in Chapter 4.

1.4. SUMMARY

Our understanding of neutrino physics is far from complete. The absolute mass and nature of the neutrino, the observation of parity violation, possible violation of lepton-number symmetry, the extreme mass differences between neutrinos and their charged leptons, the existence of exotic particles such as right-handed gauge bosons and of the Majoron, and what role the neutrino would play as a Majorana particle in the baryon asymmetry of the universe via leptogenesis are all important aspects of neutrino physics that could be probed with $\beta\beta$-decay experiments.

MAJORANA, a next-generation $0\nu\beta\beta$-decay experiment, proposes to search for the $0\nu\beta\beta$-decay of ^{76}Ge to ^{76}Se using hundreds of kilograms of high purity germanium enriched to 86% in ^{76}Ge. The success of the experiment heavily depends on its capability to mitigate background caused by cosmogenic activity and primordial contamination, such as products of the ^{238}U and ^{232}Th decay chains present in all materials. The use of ultra-pure copper in MAJORANA could significantly lower these intrinsic levels of radiation. In the case of Cascades, errors made in the construction techniques and neglecting to reduce impurities in parts other than the copper cryostat led to high levels of primordial background. This serves as important guidance and could help achieve the goals of the MAJORANA experiment: to quantify the $0\nu\beta\beta$-decay rate and place a value on the effective Majorana electron neutrino mass by observing a sharp peak at the $\beta\beta$ endpoint for ^{76}Ge. This could open the door for a revised Standard Model, altering our understanding of fundamental interactions and the role of neutrinos in the universe.

CHAPTER 2

TECHNICAL ASPECTS

2.1. BRIEF OVERVIEW OF GERMANIUM DETECTORS

The first germanium detector was built in the 1960's using Li-donor compensation of p-type germanium crystals [60]. Since then, germanium detectors have undergone much development and remain today a detector of choice for γ-ray detection with their high efficiency, excellent energy resolution, good timing, and good signal-to-background ratio [71]. These characteristics are achieved by a combination of crystal properties that include large electron and hole mobilities, large lifetimes, the ability to grow crystals of large sizes with high purity and low crystal defects, and a small band gap for the semiconductor germanium [71].

Advances in electronics go hand-in-hand with the development of germanium detectors [69]. Improved contact segmentation techniques have allowed for high accuracy and efficiency measurements of the positions, energies and paths of photon interactions in the detector, as well as the development of low-noise electronics for better energy resolution (particularly at low energies), low-noise signal amplification and filtering, and fast digitization [71]. Fast digitization enables the precise analysis of pulse shapes in germanium detectors to obtain additional information, such as the positions and energies of interactions and the distinction between full-energy and partial-energy deposition gamma-rays. Furthermore, the distinction between single and multiple interactions allows for electrons and Compton-scattered γ-rays interacting in the detector to be differentiated [69]. This helps suppress γ-rays and unwanted backgrounds for sensitive experiments, such as searching for the $0\nu\beta\beta$-decay using HPGe detectors enriched in ^{76}Ge.

Today large-volume germanium detectors are built thanks to advances in the field of crystal growth and purification [71]. First suggested in 1971 by Hall, the idea of growing germanium crystals of high purity was developed as a result of the main drawback of Ge(Li) detectors- the high mobility of lithium donors in germanium which, to keep the detector operable, required a time-consuming re-drifting process that would limit the size of the germanium detectors [39]. It took another ten years for HPGe crystals to replace Ge(Li) detectors. Today, refinement in the crystal growth process has allowed for crystals to be grown up to almost 100 mm in diameter [71].

Gamma-ray detection in germanium detectors is detected through the interaction of radiation with germanium atoms [53]. This can occur through three different processes: photoelectric absorption, which is more significant at low energies (<150 keV), Compton scattering, which dominates at energies ranging between 150 keV and 8 MeV, and pair production, which is most likely to occur for energies higher than 8 MeV [53]. Through the ionization of the germanium atoms, these three interactions produce primary charge carriers (electron-hole pairs). Electron-hole pairs drift under the influence of an external electric field towards their respective electrodes, where their motion is recorded as displacement current provided this displacement current is larger than the leakage current caused by the small band gap and thermal excitation of the charge carriers [53]. To ensure this is the case, a germanium detector is operated as a reverse-bias diode, in which a voltage V_d is applied to deplete the crystal of most free charge carriers and increase the sensitive volume of the detector. This voltage V_d is given by:

$$V_d = \frac{Nd^2}{2\epsilon} \,, \tag{12}$$

where N is the electrically active net-impurity concentration in the crystal, d is the depletion depth equal to the wafer thickness, and ϵ is the external electric field [53]. The low leakage current is further reduced by cooling the HPGe crystals to below 120 K [71].

2.2. BACKGROUNDS

To detect the rare $0\nu\beta\beta$-decay of ^{76}Ge to ^{76}Se, half-lives of the order of 10^{25}-10^{27} years have to be probed. Using an active detector with a large volume (hundreds of kilograms in the case of MAJORANA) and further enriching the 7.83%-naturally abundant germanium to 86% is necessary for the success of the experiment. More importantly, the detector must compete with processes in the environment that are much more prolific, such as background [56]. Background greatly reduces the sensitivity of a counting experiment. If an experiment with counting time t is composed of a detector with N $\beta\beta$-decay active nuclei, the experimental upper limit on the effective majorana neutrino mass $\langle m_{\beta\beta}\rangle$ scales as $\langle m_{\beta\beta}\rangle \approx 1/(\mathrm{Nt})^{1/2}$ assuming zero-background, but as $\langle m_{\beta\beta}\rangle \approx 1/(\mathrm{Nt})^{1/4}$ assuming the background is directly proportional to Nt [32]. One can easily see that it is necessary to make background mitigation a primary objective of any sensitive $\beta\beta$-decay experiment.

In order to take efficient measures, the causes and sources of backgrounds must be well understood. The following sections deal with categorizing the sources of background present in a germanium experiment, followed by an in-depth discussion of experimental methods used to mitigate these backgrounds.

2.2.1. Background Sources. Backgrounds in germanium-based experiments fall into two categories: cosmogenic backgrounds and primordial contamination.

2.2.1.1. *Cosmogenic Backgrounds.* Cosmic radiation on Earth is a subject that has been studied for many years [54]. Cosmic-rays originate from various extrasolar sources, such as active galactic nuclei, radio galaxies, quasars, pulsars, supernovae and black holes. These "primaries", approximately composed of 90% protons, 9% α-particles and 1% heavier particles, hit the Earth's atmosphere at a rate of 1000 $m^{-2}s^{-1}$ [66]. Their interactions with the atmosphere at high altitude create showers composed of neutrons, electrons, neutrinos, protons, muons and pions (secondaries). The relative intensity of charged pions:protons:electrons:neutrons:muons is approximately 1:13:340:480:1420 by the time these particles reach sea level, although their flux depends on the geomagnetic latitude and the 11-year solar cycle [41]. Secondary cosmic-rays directly interact with the detector itself and/or with other secondary neutrons and photons resulting from other showers produced in non-detector components such as the rock or shielding [32]. Most photons and electrons are absorbed by the detector shielding or the amount of rock above the detector, commonly referred to as overburden, such that the relevant backgrounds of concern for underground experiments are generally induced by muons, neutrons, and the production of radioisotopes.

Muons created in the atmosphere lose energy through ionization, bremsstrahlung, e^+e^- pair production and photoproduction as they interact with the overburden and shielding of the detector. This energy loss, however small compared to the fraction of the primary energy, combined with the relativistic extended effects of the muons' decay lifetime, enable the muons to penetrate deep underground. The muon flux can therefore be significantly reduced at greater depths, with a differential muon spectrum shifted to higher energies at larger depths [21].

Although muon events can be vetoed as they pass through the detector by using active shielding, they are still considered a nuisance as they contribute to the experiment's dead time and produce tertiary neutrons at the event site. This tertiary neutron production is enhanced in high Z material, such as lead shielding at a depth of a few meters water equivalent (m.w.e.), while fission and (α,n)-derived neutrons produced by the concentrations of ^{238}U and ^{232}Th in the continental upper crust (refer to Section 2.2.1.2) dominate at a depth of below a few hundred meters water equivalent [41]. Neutrons from secondary cosmic-rays can also directly interact with the detector through inelastic scattering and radiative capture (see radioisotope production further below).

Tertiary neutrons are created via several different mechanisms, such as electromagnetic showers produced by the passage of muons through matter resulting in the emission of photons and electrons from bremsstrahlung and pair production. Other processes that produce neutrons involve muon interactions with nuclei through the exchange of virtual photons (muon spallation), muon-nucleon quasielastic scattering and secondary neutron production from any of these interactions [32]. Figure 2.1 shows the flux of secondary cosmic-rays and tertiary neutrons in a typical lead shield vs. the overburden of the detector in meters water equivalent.

Secondary cosmic-rays can also contribute to background by the production of radioisotopes through neutron capture (the dominant process at the Earth's surface), photodisintegration, in which high-energy gammas knock out a proton or neutron from a nucleus, and other reactions due to muons and alpha particles [32]. Radioisotopes produced in this manner in germanium-based experiments include ^{54}Mn, ^{57,58}Co, ^{65}Zn, ^{68}Ge in the germanium crystal, and ^{54}Mn, ^{56,57,58,60}Co, ^{59}Fe in copper used in the cryostat and for shielding. Backgrounds created by these shorter-living radioisotopes generally dominate the background at the beginning of an underground experiment [6]. For a detailed listing of γ-ray lines caused by cosmogenic activity typical to germanium experiments, refer to Tables 2.1 - 2.8 at the end of this chapter.

For the sake of completeness, we add that neutrinos can also contribute to the background of germanium experiments, though their contribution is fairly

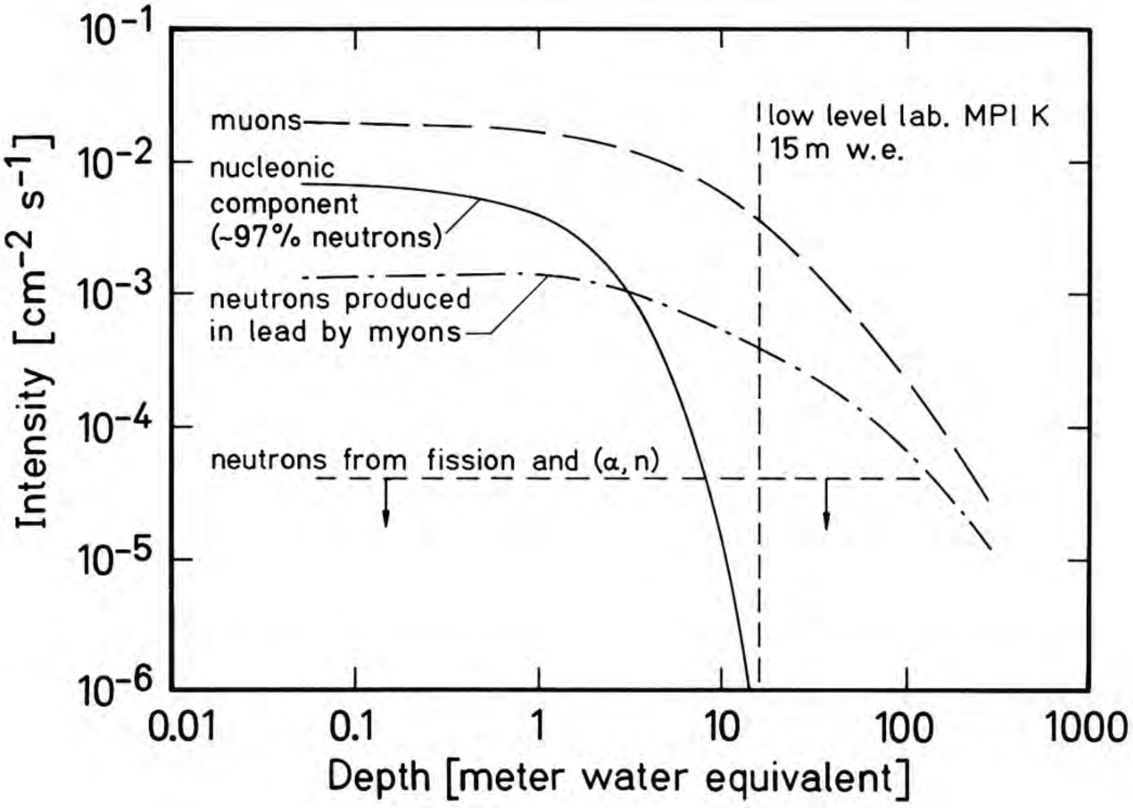

FIGURE 2.1. Flux of muons, tertiary neutrons, and neutrons produced from fission and (α,n) reactions shielded in lead vs. the shielding depth (m.w.e.) [41]

minimal compared to muons and neutrons. Neutrinos can interact with the detector in the following ways:

$$\bar{\nu}_l + \mathrm{p} \rightarrow l^+ + \mathrm{n} \,, \tag{13}$$

$$\nu_l + \mathrm{n} \rightarrow l^- + p \,, \tag{14}$$

$$\bar{\nu}_l + \mathrm{N} \rightarrow \bar{\nu}_l + \mathrm{N}^* \,, \tag{15}$$

where l can take on any leptonic flavor (e, μ, τ) and N is a target nucleus [32]. Methods to mitigate cosmogenic backgrounds will be discussed in Section 2.3.

2.2.1.2. *Primordial Backgrounds.* On some level, primordial radiation contaminates all rock environment, detector components, and shielding materials.

The most important primordials consist of three long-lived isotopes with half-lives to the order of 10^9 years: ^{40}K, ^{238}U, and ^{232}Th. They are found in the continental upper crust with an average concentration of 850 Bq/kg, 36 Bq/kg and 44 Bq/kg respectively, and their concentrations are approximately halved in soil with the exception of ^{232}Th which remains the same [41]. The three primordials emit a variety of by-products (other types of nuclei, neutrons, α-particles, β-particles and γ-rays) in a wide-ranged spectrum. Most γ-rays from which detectors must be shielded are emitted from the decays of these three primordials, as the cosmic-ray flux only constitutes a small fraction ($\ll$1%) of the total photon flux (approximately 10 photons cm^{-2}s^{-1} at sea level) [41].

Potassium-40 β-decays to the stable isotope of ^{40}Ca or undergoes electron capture to the stable isotope of ^{40}Ar [31] as seen in Figures 2.2 and 2.3. The natural abundance of ^{40}K is only 0.0117% and normally occurs in rock and concrete as K_2O and K_2CO_3, both of which are present at a level of around 1% [32]. These low concentration levels and low γ-ray energies render ^{40}K the least troublesome of the three primordials.

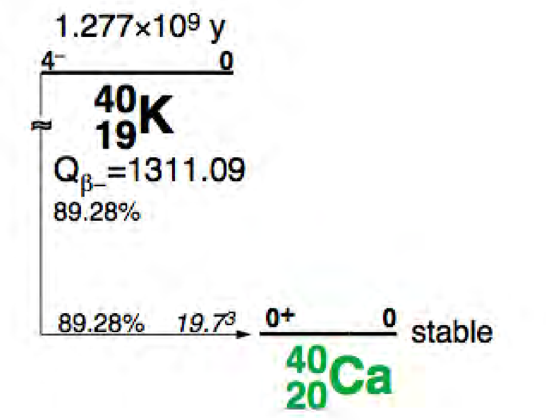

FIGURE 2.2. The β-decay of ^{40}K [31]

More dangerous sources of background are the long-lived isotopes ^{238}U and ^{232}Th, which eventually decay to the the stable isotopes ^{206}Pb and ^{208}Pb after

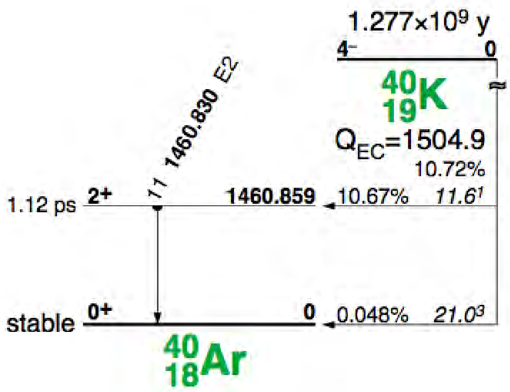

FIGURE 2.3. ^{40}K undergoing electron capture [31]

a complex series of decays. Simplified schemes are depicted in Figures 2.4 and 2.5, along with a list of γ-ray energies with intensities higher than 5%.

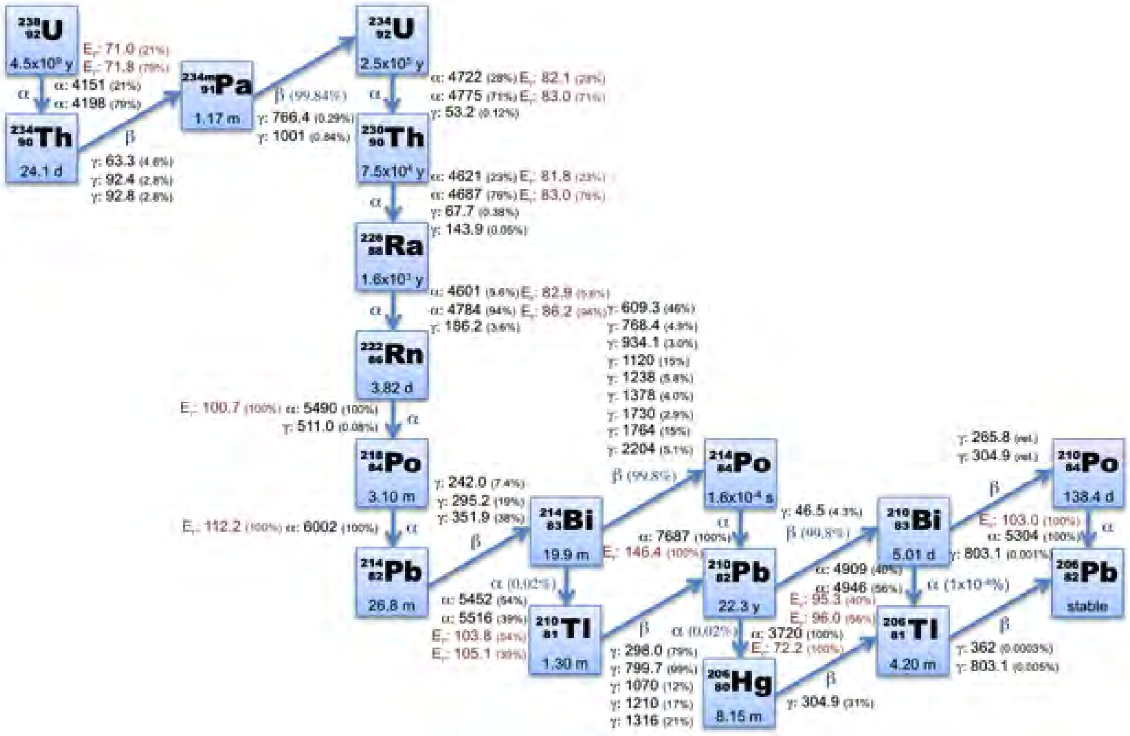

FIGURE 2.4. Scheme of the ^{238}U-chain to the stable ^{206}Pb with energies (keV) listed for the highest intensities (%)

Decay chains of ^{232}Th and ^{238}U produce radon gas (^{222,220}Rn), which is of great concern. Radon can escape solid formation by either recoil on ejection

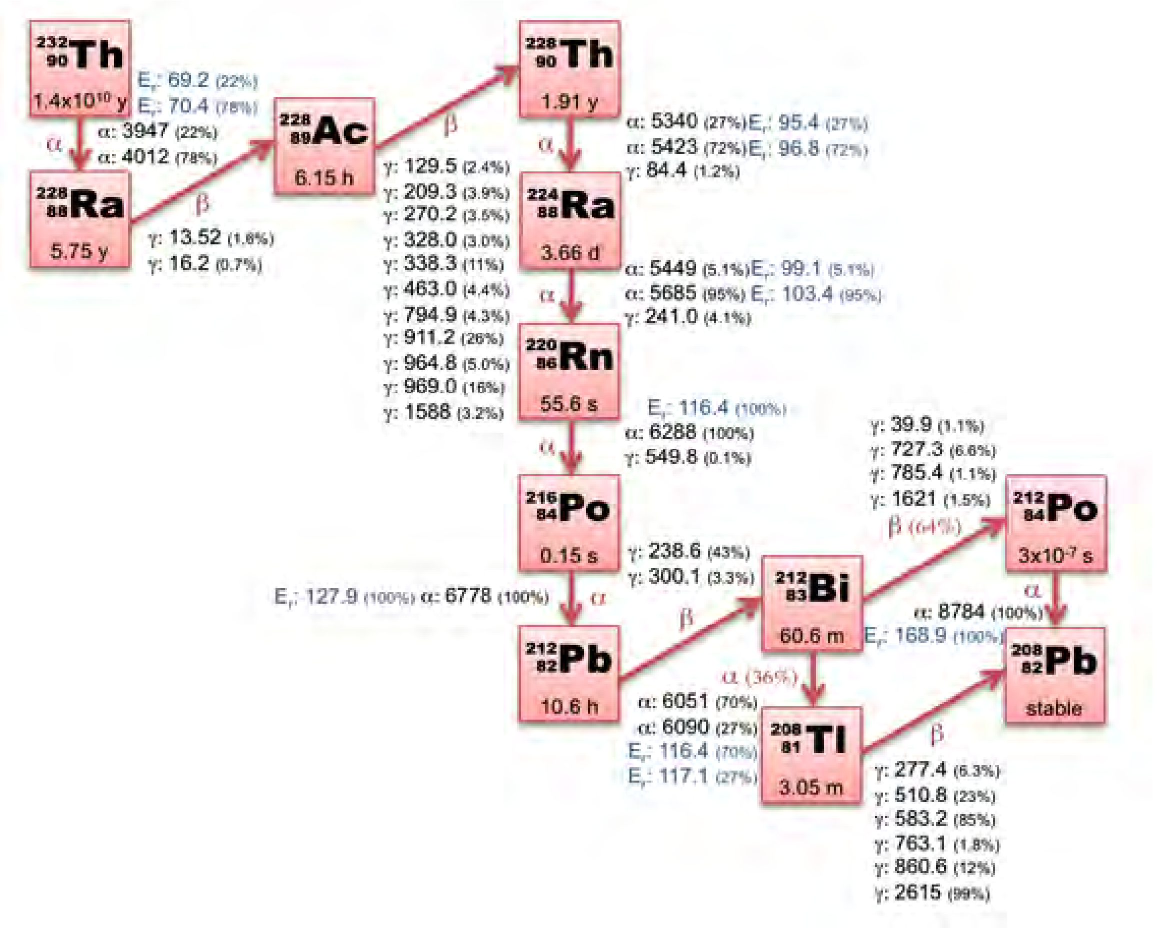

FIGURE 2.5. Scheme of the ^{232}Th-chain to ^{208}Pb (stable) with energies (keV) listed for the highest intensities (%)

of an α-particle or by diffusion, which threatens to contaminate the detector's sensitive region [41]. The concentration of radon present in the air varies, but average levels of 40 Bq/m^3 are common in underground experiments [41].

The most prominent source in airborne radioactivity is ^{222}Rn, which is released at a rate of approximately 1300 Bq m^{-2}day^{-1} [46] through the ^{238}U decay chain. Radon-222 feeds into ^{214}Bi, a problematic isotope with its γ-ray lines of 2204.21 keV (4.86% intensity) and 2447.86 keV (1.5% intensity). The ^{222}Rn family dies out with the production of ^{214}Pb ($\tau_{1/2}$ = 26.8 m) which eventually decays to the stable isotope ^{206}Pb. Although ^{222}Rn has a relatively short half-life of 3.82 days, it also is a distant parent to ^{210}Pb, another long-lived isotope with $\tau_{1/2}$ = 22.3 years. Lead-210, which can also be a source of contamination from the shielding of the detector, feeds into the daughter nuclides ^{210}Bi and ^{210}Po. Out of these two isotopes, ^{210}Po is the least problematic as its radiation hardly ever escapes self-absorption [41]. The β-decay of ^{210}Bi, however, releases an electron with energy 1.16 MeV which produces bremsstrahlung and characteristic x-rays in lead and can severely contaminate the background at low energies. This can interfere with dark matter and axion searches.

Radon-220 has a shorter half-life than ^{222}Rn with $\tau_{1/2}$=55.6 s and a concentration level in air usually lower than ^{222}Rn. Radon-220 eventually feeds into the production of ^{208}Tl, the source of another problematic 2614.53 keV γ-ray emitted with a 99% relative intensity. Unlike ^{222}Rn, the ^{220}Rn family dies out quickly with its daughter ^{212}Pb ($\tau_{1/2}$=10.64 h) which eventually decays to the stable isotope of ^{208}Pb [41]. The importance of eliminating radon in low-level experiments cannot be overstated, and methods to mitigate radon-induced backgrounds and other backgrounds from environmental activity and radioimpurities in the detector will be discussed in Section 2.3.

Uranium-238 and ^{232}Th are also responsible for low-energy neutron and photon backgrounds in underground experiments through α-decays present in the decay chains [32]. For ^{238}U, these alpha emitters include ^{216,212}Po with α-particles of energies 6.8 MeV and 6.0 MeV respectively. In the case of ^{232}Th, the most important α emitters are ^{218,214,210}Po with energies 6.0 MeV, 7.7 MeV and 5.3 MeV. The dominant production mechanism is usually (α, n), but direct fission neutrons can also be created from ^{238}U and ^{232}Th in the rock above the detector [32]. The intensity and energy range of this neutron flux is dependent upon the the type of rock and the natural levels of ^{238}U and ^{232}Th present.

For a detailed listing of γ-ray lines caused by primordial backgrounds, refer to Tables 2.1 - 2.8 at the end of this chapter. This list is neither complete nor are all lines expected to be present in each germanium spectrum.

2.3. METHODS TO MITIGATE BACKGROUNDS

The difficulty inherent to all $0\nu\beta\beta$-decay experiments is the extremely low-background levels required to reach the needed sensitivity. These necessary low-background levels are driven by the extremely long half-lives of the candidate isotopes. Fortunately, most backgrounds can be mitigated in carefully constructed experiments with the use of several techniques and methods of analysis developed and studied over the years [69]. The specific techniques discussed in this section will include passive shielding, underground depth, radon purging and using ultra-pure materials through material treatment.

2.3.1. Passive Shielding.

2.3.1.1. *Outer and Inner Shield.* Although decay products of the ^{232}Th and ^{238}U chains make up the largest portion of background radiation, they are also the easiest to mitigate by the use of a massive lead shield [69]. This will cause an additional background source of bremsstrahlung radiation from the ^{210}Bi beta particle up to approximately 850 keV [15]. The shield should be lined with ancient lead to minimize background from the few hundred Bq/kg of ^{210}Pb that make up contemporary lead [16]. An inner shield of electroformed copper is also generally used to screen out contributions from the bulk lead itself, as well as any additional cosmic background [69].

2.3.1.2. *Underground Depth.* The most effective way to protect a sensitive $\beta\beta$-decay experiment against cosmic radiation is to operate the detector deep underground as to reduce the background contribution from fast neutron elastic and inelastic scattering, cosmogenic radioactive isotope production and muon capture [69]. Figure 2.6 illustrates the importance of both depth underground and proper passive shielding.

2.3.1.3. *Radon Purging.* In order to protect a germanium detector from natural levels of ^{222}Rn and ^{220}Rn in the air, nitrogen gas is used to purge an

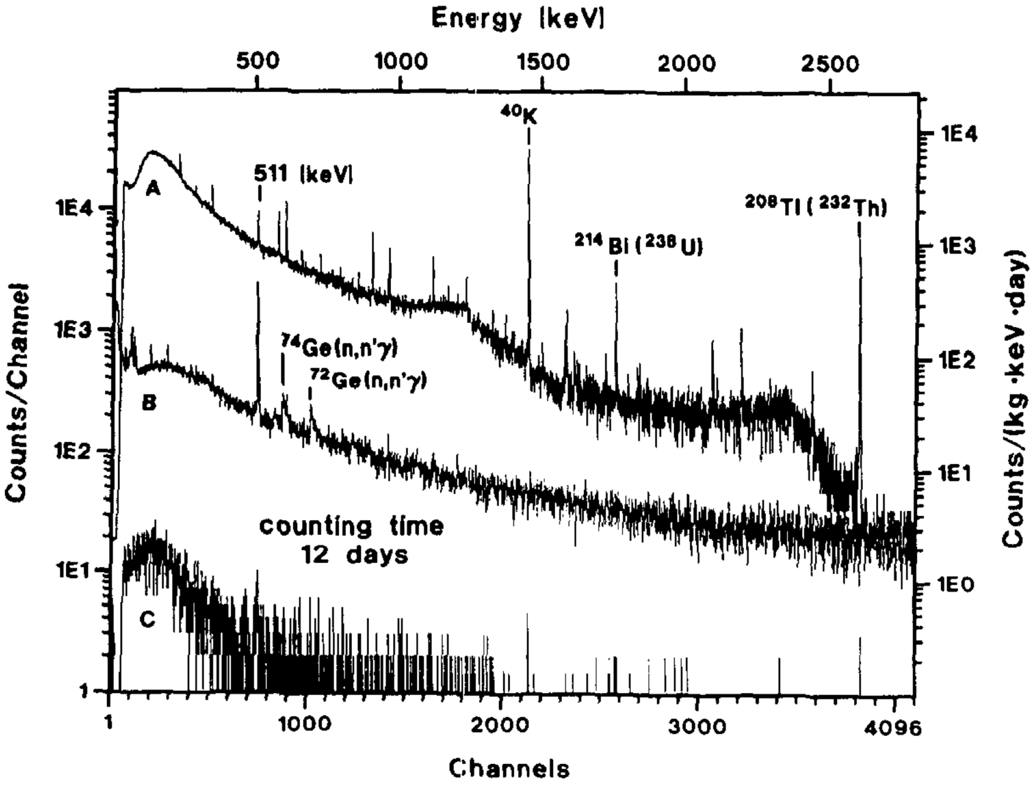

FIGURE 2.6. Background spectra for a germanium detector with 0.5 kg of active volume without shield (top spectra), with a 15-cm lead shield (middle spectra) and with the same shield at around 500 m.w.e. [41].

environment of radon. The physical properties of radon versus nitrogen, such as radon being heavier than nitrogen and having a lower boiling point, ensure that boil-off gas in a tank of liquid nitrogen remains adequately pure as radon remains in liquid form and evaporates at a slower rate. The configuration details of the radon purging system for a typical low-background germanium experiment will be discussed in Chapter 3.

2.3.2. Ultra-Pure Materials. The use of ultra-pure materials in the detector is crucial in background reduction, i.e.- the degree of radiopurity in the detector assembly, which in turn is connected to the level of improvement that can be achieved for all detector components [41]. In order to reduce levels of natural radioactive impurities in the detector, sophisticated techniques in zone refinement, crystal growth and copper electroforming have been developed over the years.

The process of zone refinement involves melting a bar of polycrystalline germanium by slowly moving a heat source (an RF induction coil) along its length while sealing this bar in a vessel to prevent oxidation [69]. Since most impurities in germanium have a segregation coefficient of less than 1, (their concentrations are higher when melting at equilibrium rather than in the solid form), electrochemical impurities are concentrated in the melt and swept down to the ends of the bar, leaving a pure central region behind [69]. Multiple passes are performed in order to reach the required low impurity concentration [69].

The Czochralski crystal growth method, named after its inventor Jan Czochralski, involves melting the zone-refined polycrystalline germanium into a silica crucible [65]. A single germanium seed is dipped into the melt and rotated while a single germanium crystal is grown onto the seed from the molten germanium [65]. All germanium in the crucible must be consumed during a crystal growth run as any remaining germanium will freeze and crack the crucible during the procedure [65]. The net impurity concentration of germanium crystals must lie within a narrow range of (0.5 - 1.5 x 10^{10}) cm^{-3} for the proper fabrication of a large-volume coaxial germanium detector, although this range depends on the detector's diameter [69]. A highly non-uniform electric field will result from an impurity concentration that is too low, while an impurity concentration that is too high creates the need of an excessive high depletion voltage and hence risks possible electrical breakdown [69]. Despite these preventative measures, products of the ^{238}U and ^{232}Th decay chains may still present on some undetectable level in the germanium, and hazardous cosmogenic isotopes, i.e.- $^{56-60}$Co and ^{68}Ge, are also accumulated while the germanium is above ground [41].

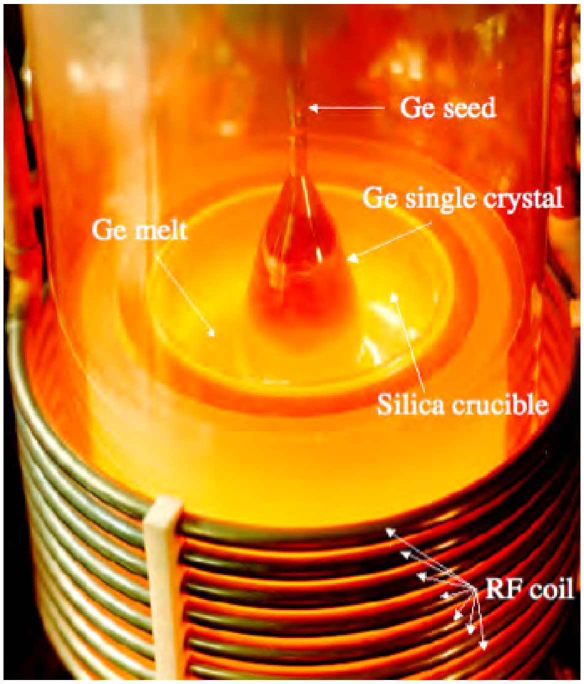

FIGURE 2.7. The pulling of a HPGe crystal from a melt contained in a silica crucible at 936^{o}C as hydrogen gas flows inside a quartz envelope [69]

Contamination is most likely unevenly spread between all electronic parts, surface coating and structural materials in the detector, however the most massive component of an ultra-low background HPGe detector is its copper cryostat [57]. The most severe cosmic-ray generated radioisotope ^{60}Co ($\tau_{1/2}$= 5.2 y, Q_β = 2.505 MeV) results from (n,α) reactions on ^{63}Cu [69], while contamination from primordial radiation measures at approximately 10 μBq/kg [57]. In order to minimize the production of these cosmogenic impurities and reach a desired level of around 1 μBq/kg in ^{238}U and ^{232}Th, all copper used in MAJORANA must be electrolyrically purified.

In the electroforming copper process, a copper anode induces the production of positive copper ions through an acidic $CuSO_4$ solution under the influence of a low-voltage. These ions reach a stainless steel mandrel that acts initially as the cathode where large high purity copper crystals are formed [69]. One of the problems of the electroforming process is that mechanically sound copper is obtained by forming smaller-sized crystals [69]. Hence factors such as bath temperature, rate of plating, pH, the use of crystal-growth inhibiting chemicals and especially the electroforming potential are carefully limited and well monitored in order to produce the best quality copper mechanical properties and purity [57].

There has been significant progress made in producing high purity copper through the electrochemical process used for copper electroforming. This progress has been recorded throughout the years as follows:

- In 1995, a limit of <9 μBq/kg for ^{232}Th was measured in IGEX electroformed copper with a 90-day radiometric measurement of $\sim$10 kg at 4000 meters water equivalent [18].
- In 2004, it was shown that recrystallization of the $CuSO_4$ starting material could extensively purify the $CuSO_4$ bath solution used in the electroforming process [69].
- In 2004, a source of commercially electroformed copper was tested to <12 μBq/kg for ^{232}Th [42].
- In 2005, a limit of <8 μBq/kg for ^{232}Th was measured on MEGA copper with a 1-minute measurement of <1 g copper with an inductively coupled plasma mass spectrometer (ICPMS) [19].
- In 2005, it was shown that levels of ^{230}Th could be suppressed by a factor of >8000 through electroforming [19].
- In 2005, assay sensitivities of 2 - 4 μBq/kg for ^{232}Th were achieved by improved methods [19].
- In 2006, levels of ^{232}Th in electroformed samples were shown to be essentially at background, indicating that <2 μBq/kg could be attainable [69].
- At this writing, the best ICPMS assay of primordial activity in copper electroformed at PNNL is currently 0.6 μBq/kg for ^{232}Th and 1.3 μBq/kg for ^{238}U, although these results are not yet published [43].

In the context of this dissertation, the goals of the MAJORANA experiment are to reach a contaminant level of 0.1 μBq/kg in ^{208}Tl and 0.4 μBq/kg in ^{214}Bi, which would correspond to an activity of 0.3 μBq/kg in ^{232}Th [69]. Research on electrochemical behavior, Th/U rejection rates and other predictive efforts will allow further insight and improvement to be made in the electroforming process needed to reach these low levels of impurities.

2.4. SUMMARY

Necessary steps to protect germanium detectors from primordial radiation and cosmogenic activity must be taken regarding depth underground, shielding, proper materials selection and materials purification, radon purging and electronic signal processing to ensure the best experimental optimization [15]. Focusing more time and resources on perfecting these background-reducing techniques will be key for the success of any $\beta\beta$-decay experiment. One focus of the present research is the analysis of data from an experiment to determine an upper bound on primordial radiation levels in Cascades, a HPGe multi-crystal array and cryostat constructed with electroformed copper similar to that electroformed for MAJORANA.

TABLE 2.1. Common background lines observed in Ge-Spectra for γ-rays with a probability of occurrence $I_\gamma \geq 5\%$ for energies ranging from 0 - 130 keV [40].

γ-line (keV)	Isotope produced	Parent Reaction reaction	I_γ (%)	Remarks
14.41	^{57}Fe	^{57}Fe(p,n)^{57}Co ^{56}Fe(p,γ)^{57}Co ^{56}Fe(d,n)^{57}Co	8.8	cosmic reaction ($\tau_{1/2}$=271.3 d)
46.50	^{210}Bi	^{210}Pb	3.65	^{238}U series ($\tau_{1/2}$=22.28h)
50.10	^{223}Ra	^{227}Th	7.28	^{235}U series ($\tau_{1/2}$=11.43 d)
53.40	^{73m}Ge	^{72}Ge(n, γ)^{73m}Ge	10.50	cosmic reaction ($\tau_{1/2}$=0.5 s)
63.32	^{234}Pa	^{234}Th	4.49	^{238}U series ($\tau_{1/2}$=24.1 d)
68.70	^{63}Ge	^{73}Ge(n,n')^{73}Ge		cosmic reaction
72.80 74.97 84.45 84.94 87.30	Pb	Pb x-ray		
84.21	^{231}Pa	^{231}Th	6.60	^{235}U series ($\tau_{1/2}$=25.5 h)
92.60	^{234}Pa	^{234}Th	5.16	^{238}U series ($\tau_{1/2}$=24.1 d)
93.32	^{67}Zn	^{65}Cu(α,2n)^{67}Ga	48.00	cosmic reaction ($\tau_{1/2}$=78.3 h)
109.89	^{19}F	^{19}F(n,n')^{19}F		cosmic reaction
122.40	^{57}Fe	^{57}Fe(p,n)^{57}Co ^{56}Fe(p,γ)^{57}Co ^{56}Fe(d,n)^{57}Co ^{57}Co(n,n')^{57}Co		cosmic reaction ($\tau_{1/2}$=271.3 d)

TABLE 2.2. Common background lines observed in Ge-Spectra for γ-rays with a probability of occurrence $I_\gamma \geq 5\%$ for energies ranging from 130 - 220 keV [40].

γ-line (keV)	Isotope produced	Parent reaction	I_γ (%)	Remarks
131.20	^{234}U	^{234}Pa	20.00	^{238}U series ($\tau_{1/2}$=6.7 h)
136.47	^{57}Fe	^{57}Fe(p,n)^{57}Co ^{56}Fe(p,γ)^{57}Co ^{56}Fe(d,n)^{57}Co ^{57}Co(n,n')^{57}Co	11.00	cosmic reaction ($\tau_{1/2}$=271.3 d)
139.70	^{75m}Ge	^{74}Ge(n, γ)^{75m}Ge	39.0	cosmic reaction ($\tau_{1/2}$=48 s)
143.80	^{231}Th	^{235}U	10.90	^{235}U series ($\tau_{1/2}$=7.05$\times$10^8 yr)
159.70	^{77m}Ge	^{76}Ge(n, γ)^{77m}Ge	11.00	cosmic reaction ($\tau_{1/2}$=52.9 s)
163.30	^{231}Th	^{235}U	5.00	^{235}U series ($\tau_{1/2}$=7.05x10^8 yr)
184.59	^{67}Zn	^{65}Cu(α,2n)^{67}Ga	62.00	cosmic reaction ($\tau_{1/2}$=78.3 h)
185.70	^{231}Th	^{235}U	57.50	^{235}U series ($\tau_{1/2}$=7.05$\times$10^8 yr)
185.91	^{66}Cu	^{65}Cu(n,γ)^{66}Cu		cosmic reaction
198.40	^{71m2}Ge	^{70}Ge(n,γ)^{71m2}Ge	99.00	cosmic reaction ($\tau_{1/2}$=22 ms)
203.10	^{64}Cu	^{63}Cu(n,γ)^{64}Cu	6.64	cosmic reaction
205.30	^{231}Th	^{235}U	5.00	^{235}U series ($\tau_{1/2}$=7.05$\times$10^{8}yr)
215.50	^{77}As	^{76}Ge(n,γ)^{77m}Ge	21.00	cosmic reaction ($\tau_{1/2}$=52.9 s)

TABLE 2.3. Common background lines observed in Ge-Spectra for γ-rays with a probability of occurrence $I_\gamma \geq 5\%$ for energies ranging from 220 - 425 keV [40].

γ-line (keV)	Isotope produced	Parent reaction	I_γ (%)	Remarks
226.40	^{234}U	^{234}Pa	5.90	^{238}U series ($\tau_{1/2}$=6.7 h)
227.20	^{234}U	^{234}Pa	5.50	^{238}U series ($\tau_{1/2}$=6.7 h)
236.00	^{223}Ra	^{227}Th	11.20	^{235}U series ($\tau_{1/2}$=11.43 d)
238.60	^{212}Bi	^{212}Pb	43.60	^{232}Th series ($\tau_{1/2}$=10.64 h)
241.98	^{214}Bi	^{214}Pb	7.50	^{238}U series ($\tau_{1/2}$=26.8 m)
256.00	^{223}Ra	^{227}Th	7.60	^{235}U series ($\tau_{1/2}$=11.43 d)
269.20	^{219}Rn	^{223}Ra	13.60	^{235}U series ($\tau_{1/2}$=11.43 d)
271.20	^{215}Po	^{219}Rn	9.90	^{235}U series ($\tau_{1/2}$=3.96 s)
277.40	^{208}Pb	^{208}Tl	6.31	β^--decay ($\tau_{1/2}$=3.05 m)
278.80	^{64}Cu	^{63}Cu(n,γ)^{64}Cu	30.12	cosmic reaction
295.20	^{214}Bi	^{214}Pb	18.50	^{238}U series ($\tau_{1/2}$=26.8 m)
351.92	^{214}Bi	^{214}Pb	38.50	^{238}U series ($\tau_{1/2}$=19.9 m)
367.94	^{200}Hg	^{199}Hg(n,γ)^{200}Hg	81.35	cosmic reaction
401.70	^{215}Po	^{219}Rn	6.64	^{235}U series ($\tau_{1/2}$=3.96 s)

TABLE 2.4. Common background lines observed in Ge-Spectra for γ-rays with a probability of occurrence $I_\gamma \geq 5\%$ for energies ranging from 425 - 610 keV [40].

γ-line (keV)	Isotope produced	Parent reaction	I_γ (%)	Remarks
427.89	^{125}Te	^{124}Sn(p,γ)^{125}Sb	29.40	cosmic reaction ($\tau_{1/2}$=2.27 a)
510.80	^{208}Pb	^{214}Tl	22.60	^{232}Th series ($\tau_{1/2}$=3.05 m)
511.00				Annihilation
558.20	^{76}Ge	^{76}Ge(n,n')^{76}Ge	79.71	cosmic reaction
563.30	^{134}Ba	^{133}Cs(n,γ)^{134}Cs	8.38	reaction waste ($\tau_{1/2}$=2.06 a)
569.50	^{234}U	^{234}Pa	10.00	^{238}U series ($\tau_{1/2}$=6.7 h)
569.79	^{207}Pb	^{207}Pb(n,n')^{207}Pb ^{206}Pb(n,γ)^{207}Pb		cosmic reaction
583.20	^{208}Pb	^{208}Tl	84.50	^{232}Th ($\tau_{1/2}$=3.05 m)
595.90	^{74}Ge	^{73}Ge(n,γ)^{74}Ge ^{73}Ge(n,n')^{74}Ge	34.65	cosmic reaction
600.55		^{124}Sn(p,γ)^{125}Sb	17.78	cosmic reaction ($\tau_{1/2}$=2.77 y)
604.70	^{134}Ba	^{133}Cs(n,γ)^{134}Cs	97.60	reactor waste ($\tau_{1/2}$=2.06 a)
606.64	^{125}Te	^{125}Sn(p,γ)	5.02	cosmic reaction ($\tau_{1/2}$=2.77 y)
609.30	^{214}Po	^{214}Bi	44.80	^{238}U series ($\tau_{1/2}$=19.9 m)

TABLE 2.5. Common background lines observed in Ge-Spectra for γ-rays with a probability of occurrence $I_\gamma \geq 5\%$ for energies ranging from 610 - 805 keV [40].

γ-line (keV)	Isotope produced	Parent reaction	I_γ (%)	Remarks
635.90	^{125}Te	^{124}Sn(p,γ)^{125}Sb	11.32	cosmic reaction ($\tau_{1/2}$=2.77 y)
651.00	^{114}Cd	^{113}Cd(n,γ)^{114}Cd	15.23	cosmic reaction
661.66	^{137m}Ba	^{137}Cs	85.00	reactor waste ($\tau_{1/2}$= 30.17 y)
669.60	^{63}Cu	^{63}Cu(n,n')^{63}Cu		cosmic reaction
691.00	^{72}Ge	^{72}Ge(n,n')^{72}Ge		cosmic reaction
727.30	^{212}Po	^{212}Bi	6.25	^{232}Th series ($\tau_{1/2}$=1.0 h)
751.80	^{65}Zn	^{63}Cu(α,2n)^{65}Ga	50.70	cosmic reaction ($\tau_{1/2}$=15 m)
768.40	^{214}Po	^{214}Bi	4.88	^{238}U series ($\tau_{1/2}$=19.9 m)
769.70	^{73}As	^{73}Ge(p,nγ)^{73}As		cosmic reaction
770.80	^{65}Cu	^{65}Cu(n,n')^{65}Cu		cosmic reaction
794.90	^{228}Th	^{228}Ac	4.34	^{232}Th ($\tau_{1/2}$=6.15 h)
795.80	^{134}Ba	^{133}Cs(n,γ)^{134}Cs	85.40	reaction waste ($\tau_{1/2}$=2.06 a)
801.90	^{134}Ba	^{133}Cs(n,γ)^{134}Cs	8.73	reaction waste ($\tau_{1/2}$=2.06 a)
805.00	^{114}Cd	^{113}Cd(n,γ)^{114}Cd	5.10	cosmic reaction

TABLE 2.6. Common background lines observed in Ge-Spectra for γ-rays with a probability of occurrence $I_\gamma \geq 5\%$ for energies ranging from 810 - 930 keV [40].

γ-line (keV)	Isotope produced	Parent reaction	I_γ (%)	Remarks
810.80	^{58}Fe	^{59}Co(γ,n)^{58}Co ^{59}Co(n,2n)^{58}Co ^{58}Fe(p,n)^{58}Co ^{57}Fe(p,γ)^{58}Co ^{57}Fe(d,n)^{58}Co ^{58}Fe(n,p)^{58}Mn		cosmic reaction ($\tau_{1/2}$=63 s)
833.95	^{77}Ge	^{72}Ge(n,n')^{72}Ge		cosmic reaction
834.60	^{54}Cr	^{54}Cr(p,n)^{54}Mn ^{53}Cr(d,n)^{54}Mn ^{53}Cr(p,γ)^{54}Mn	100.00	cosmic reaction ($\tau_{1/2}$=312.2 d)
846.80	^{56}Fe	^{56}Fe(n,n')^{76}Fe	19.00	cosmic reaction
846.80	^{56}Fe	^{56}Fe(p,n)^{56}Co		cosmic reaction ($\tau_{1/2}$=78.76 d)
860.60	^{208}Pb	^{208}Tl	12.42	^{232}Th series ($\tau_{1/2}$=3.05 m)
868.1	^{73}Ge	^{72}Ge(n,γ)^{73}Ge	30.12	cosmic reaction
880.51	^{234}U	^{234}Pa	9.00	^{238}U series ($\tau_{1/2}$=6.7 h)
883.24 ($\tau_{1/2}$=6.7 h)	^{234}U	^{234}Pa	15.00	^{238}U series
911.20	^{238}Th	^{228}Ac	26.60	^{232}Th series ($\tau_{1/2}$=6.15 h)
926.00	^{234}U	^{234}Pa	11.00	^{238}U series ($\tau_{1/2}$=6.7 h)
927.10	^{234}U	^{234}Pa	11.00	^{238}U series ($\tau_{1/2}$=6.7 h)

Table 2.7. Common background lines observed in Ge-Spectra for γ-rays with a probability of occurrence $I_\gamma \geq 5\%$ for energies ranging from 930 - 1240 keV [40].

γ-line (keV)	Isotope produced	Parent reaction	I_γ (%)	Remarks
946.00	^{234}U	^{234}Pa	12.00	^{238}U series ($\tau_{1/2}$=6.7 h)
962.10	^{65}Cu	^{63}Cu(n,n')^{63}Cu		cosmic reaction
964.80	^{228}Th	^{228}Ac	5.11	^{232}Ht series ($\tau_{1/2}$=6.15h)
969.00	^{228}Th	^{228}Ac	16.20	^{232}Ht series ($\tau_{1/2}$=6.15h)
1039.50	^{70}Ge	^{70}Ge(n,n')^{70}Ge		cosmic reaction
1063.64	^{207}Pb	^{207}Pb(n,n')^{207}Pb ^{206}Pb(n,γ)^{207}Pb		cosmic reaction
1097.30	^{116}Sn	^{115}In(n,γ)^{116m1}	55.70	cosmic reaction ($\tau_{1/2}$=54.1 m)
1115.50	^{65}Cu	^{65}Cu(n,n')^{65}Cu ^{65}Cu(p,n)^{65}Zn	50.75	cosmic reaction ($\tau_{1/2}$=244 d.
1120.40	^{214}Po	^{214}Bi	14.80	^{238}U series ($\tau_{1/2}$=19.9 m)
1124.51	^{65}Cu	^{70}Ge(n,α2n)^{65}Zn	50.75	cosmic reaction ($\tau_{1/2}$=244 d)
1173.20	^{60}Ni	^{59}Co(n,γ)^{60}Co	100.00	reaction in steel ($\tau_{1/2}$=5.172 y)
1204.10	^{74}Ge	^{74}Ge(n,n')^{74}Ge		cosmic reaction
1238.26	^{56}Fe	^{56}Fe(p,n)^{56}Co	13.40	cosmic reaction ($\tau_{1/2}$=78.76 d)
1238.80	^{214}Po	^{214}Bi	5.86	^{238}U series

TABLE 2.8. Common background lines observed in Ge-Spectra for γ-rays with a probability of occurrence $I_\gamma \geq 5\%$ for energies ranging from 1240 - 2615 keV [40].

γ-line (keV)	Isotope produced	Parent reaction	I_γ (%)	Remarks
				($\tau_{1/2}$=19.9 m)
1291.65	^{59}Co	^{58}Fe(n,γ)^{59}Fe	57.00	cosmic reaction ($\tau_{1/2}$=45.1 d)
1293.50	^{116}Sn	^{115}In(n,γ)^{116m}In	85.00	cosmic reaction ($\tau_{1/2}$=54.1 d)
1293.64	^{41}K	^{40}Ar(n,γ)^{41}Ar	99.16	cosmic reaction ($\tau_{1/2}$=1.83 h)
1327.00	^{63}Cu	^{63}Cu(n,n')^{63}Cu		cosmic reaction
1332.50	^{60}Ni	^{59}Co(n,γ)^{60}Co	100.00	($\tau_{1/2}$=5.172 y)
1377.60	^{57}Co	^{58}Ni(γ,n)^{57}Ni ^{58}Ni(n, 2n)^{57}Ni	30.00	$\tau_{1/2}$=36 h
1412.10	^{63}Cu	^{63}Cu(n,n')^{63}Cu		cosmic reaction
1460.80	^{40}Ar	^{40}K	99.16	$\tau_{1/2}$=1.277$\times$10^{8} y
1481.70	^{65}Cu	^{65}Cu(n,n')^{65}Cu		cosmic reaction
1547.00	^{63}Cu	^{63}Cu(n,n')^{63}Cu		cosmic reaction
1764.50	^{214}Po	^{214}Bi	15.96	^{238}U series $\tau_{1/2}$=19.9 m
2204.10	^{214}Po	^{214}Bi		^{238}U series ($\tau_{1/2}$=19.9 m)
2223.20	^{2}H	^{1}H(n,γ)^{2}H	100.00	cosmic reaction
2614.60	^{208}Pb	^{208}Pb(n,n') ^{208}Pb^{208}Tl	99.20	^{232}Th series cosmic reaction $\tau_{1/2}$=3.05 m

CHAPTER 3

THE CASCADES DETECTOR

3.1. OVERVIEW

The Cascades detector was constructed at PNNL (Pacific Northwest National Laboratory) in Richland, Washington and was developed following guidelines from the MEGA (Multi-Element Gamma-Array) project [47]. Its primary goals are to measure atmospheric particulates collected on filter paper samples and to quantify radionuclides of interest, hence improving γ-ray analysis capabilities for nuclear detonation detection applications [49]. The inherent excellent energy resolution of germanium combined with ultra-low background construction techniques, such as the use of ultra-pure materials and highly effective shielding, should increase the signal-to-noise (S/N) ratios of measurements [48]. Additionally, the detector was designed to have the potential to measure the extent to which samples are chemically purified, and contribute to other basic nuclear physics research such as the study of rare decay events through γ-γ coincidence analysis [50]. The design requirements for Cascades can be summarized as followed: 1) a maximum background reduction such that sample activity dominates the signal in the detector; 2) the highest possible γ-ray detection efficiency; 3) multiple HPGe crystal arrays packaged to maximize the detection of both single and coincident gamma-rays [48].

The Cascades detector consists of two vacuum cryostats facing one another and constructed with electroformed copper, each housing a hexagonal array of seven p-type semi-coaxial HPGe crystals operated in a reverse-biased diode configuration. The crystal arrays face each other in their individual cryostats and are mounted on a cold plate connected to a liquid nitrogen dewar that maintains the temperature of the germanium crystals near 87 K with a coldfinger. Schematics of the total assembly housed in a lead shield (see Section 3.6 for further detail on shielding) and attached to the dewar are shown in Figures 3.1 and 3.2. The lower cryostat and its components can be observed in Figure 3.3,

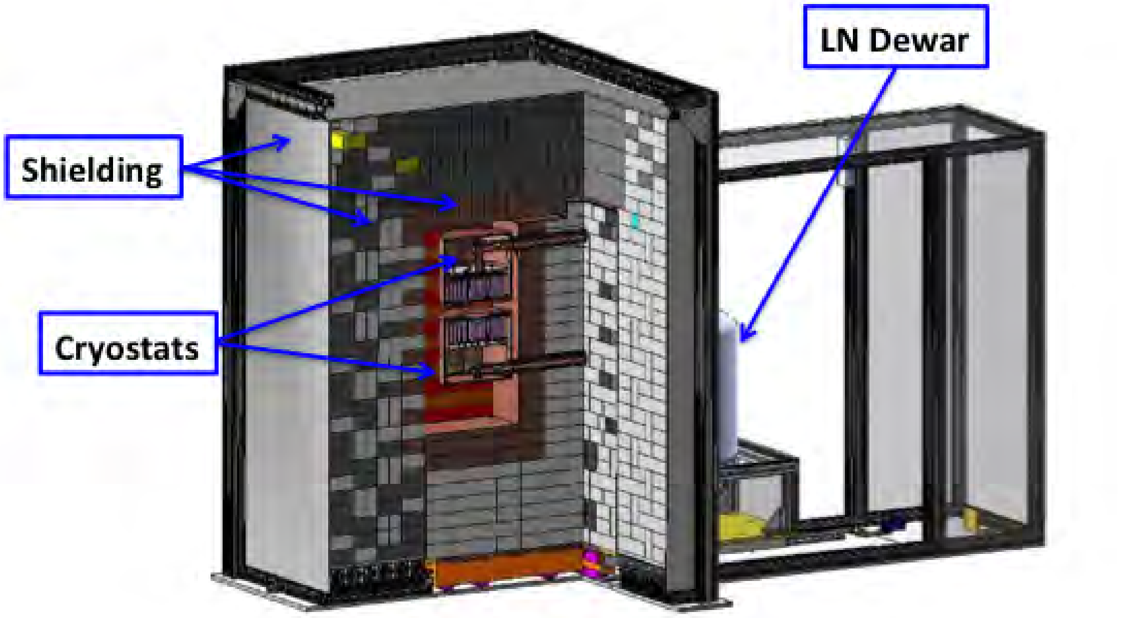

FIGURE 3.1. Depiction of two 7-crystal arrays surrounded by the lead cave

including a thin copper entrance window to improve the detection efficiency for lower-energy gamma rays (refer to Figure 3.4). The HPGe crystals each have a ∼70% relative efficiency and are arranged in a hexagonal pattern, as observed in Figure 3.5. Housing these germanium crystals in a close-packed array in large vacuum cryostats allows for a closer placement of crystals, improving the detection efficiency for both single and coincident gammas and increasing the solid-angle coverage of the detector [58]. One unfortunate drawback of this design is that the entire 7-crystal array needs to be warmed and opened should a single crystal require maintenance [48]. However, typical cryostats can operate

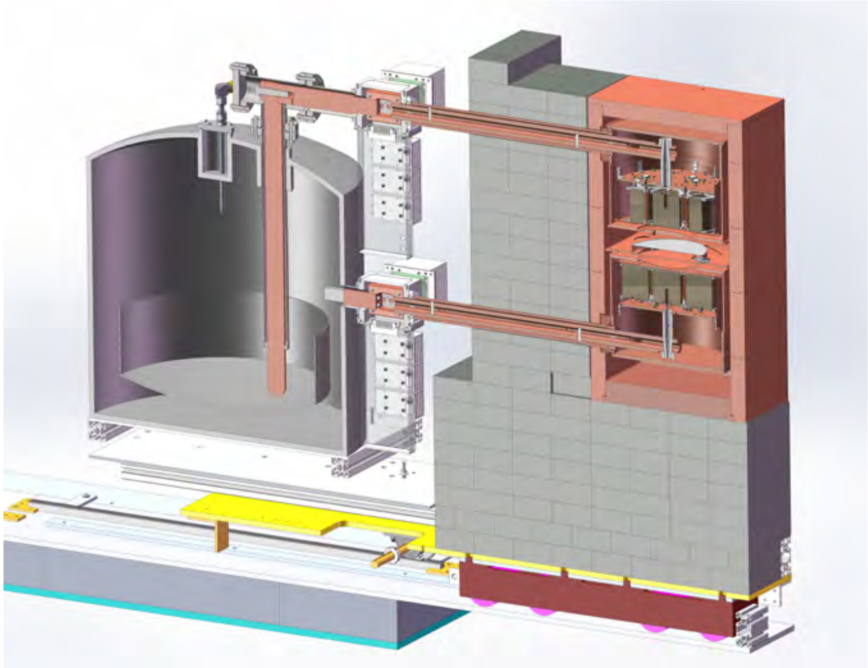

FIGURE 3.2. Schematic of Cascades surrounded by its lead cave and attached to the LN dewar

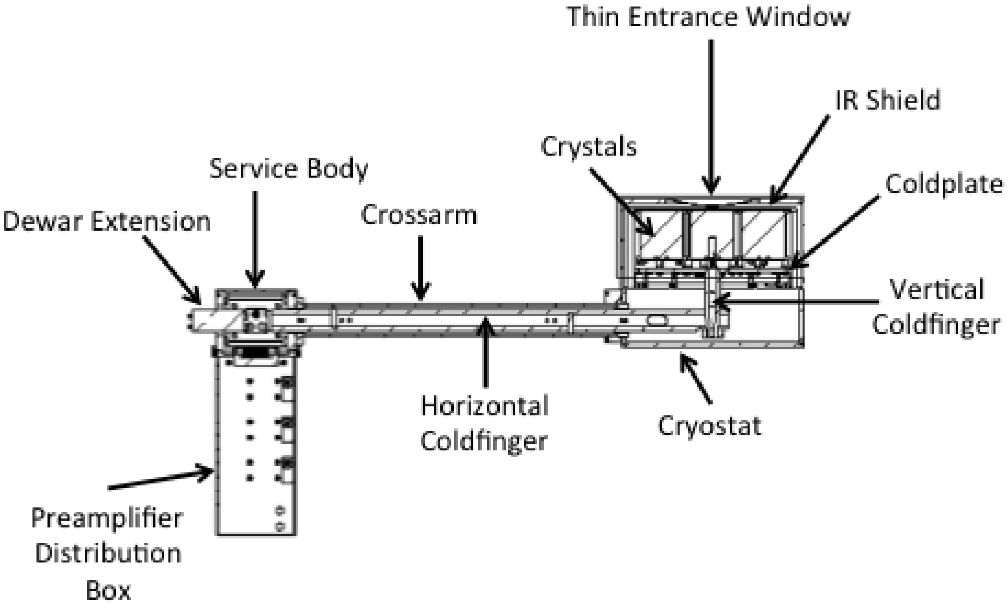

FIGURE 3.3. Detailed parts of the lower cryostat

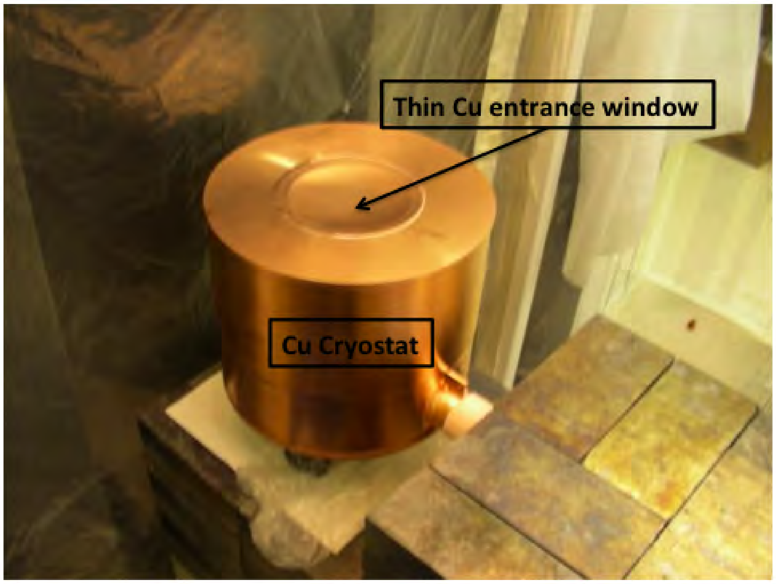

FIGURE 3.4. Thin copper entrance window of the bottom cryostat

for many years without encountering difficulties, such that the advantages of using two arrays packed with HPGe crystals outweighs the risks of one of the cryostats requiring service [48].

To facilitate their cooling, the seven crystals of each array are enclosed in an infrared (IR) shield, which is coupled tightly to the cold plate. Each crystal is mounted in an individual mounting package that minimizes materials between crystals (see Figure 3.6), improving the detection efficiency of γ-rays that scatter from one crystal into an adjacent crystal. Additionally, the lack of materials between the crystals could allow the reconstruction of pair production events where one or both annihilation γ-rays escape the crystal.

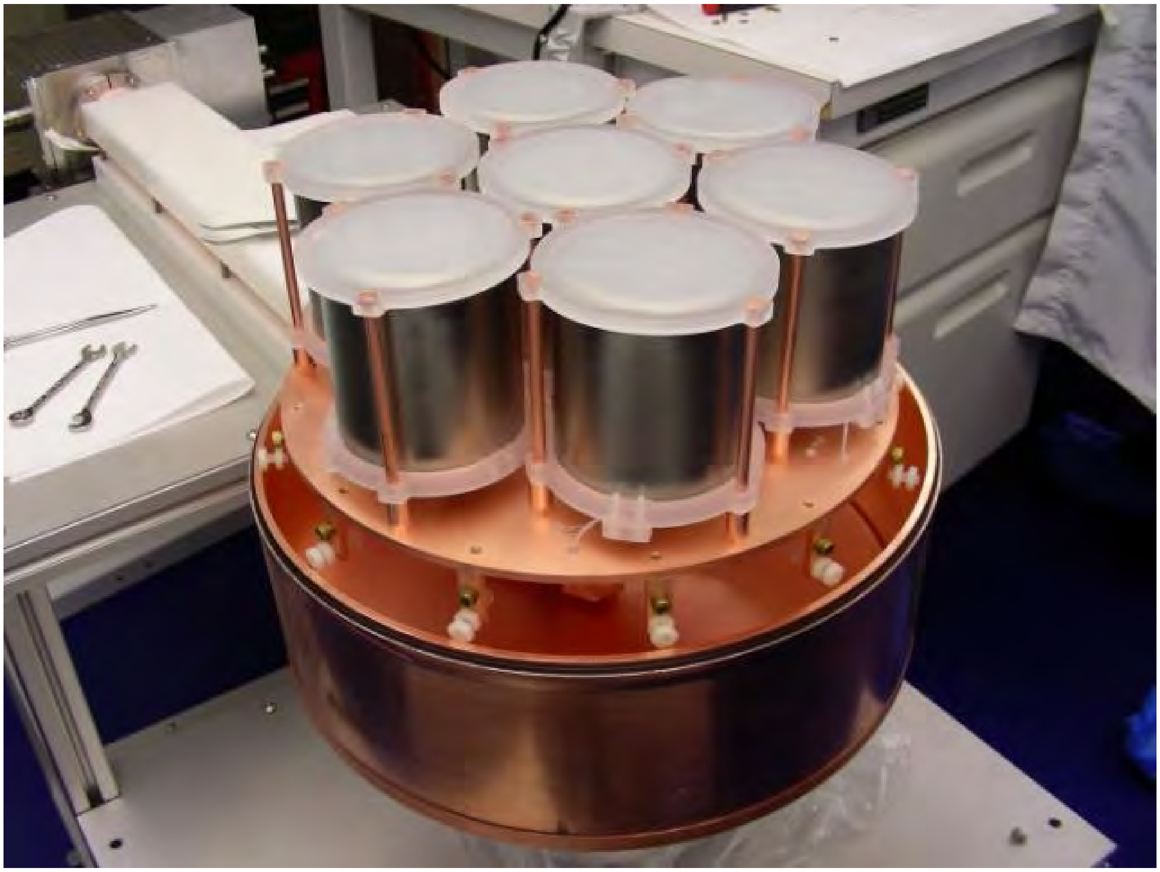

FIGURE 3.5. Lower detector array with seven crystals mounted on cold plate and arranged in a hexagonal pattern

3.2. DETECTOR ASSEMBLY

It was intended traditional methods for the construction of low-background detectors would be practiced, such as using materials with low radioactive contaminants and ultra pure reagents, as well as following clean room assembly protocol. Using PNNL-improved methods of electroforming, copper was electroformed for the main body of the cryostats, as well as long parts such as the cross arm and coldfinger [48]. Based on inductively coupled plasma mass spectrometry analysis (ICPMS), the electroformed copper for Cascades has estimated impurity levels 0.6 μBq/kg for ^{232}Th and 1.3 μBq/kg for ^{238}U, although these results are not yet published [43]. This is important to the conclusion of this work.

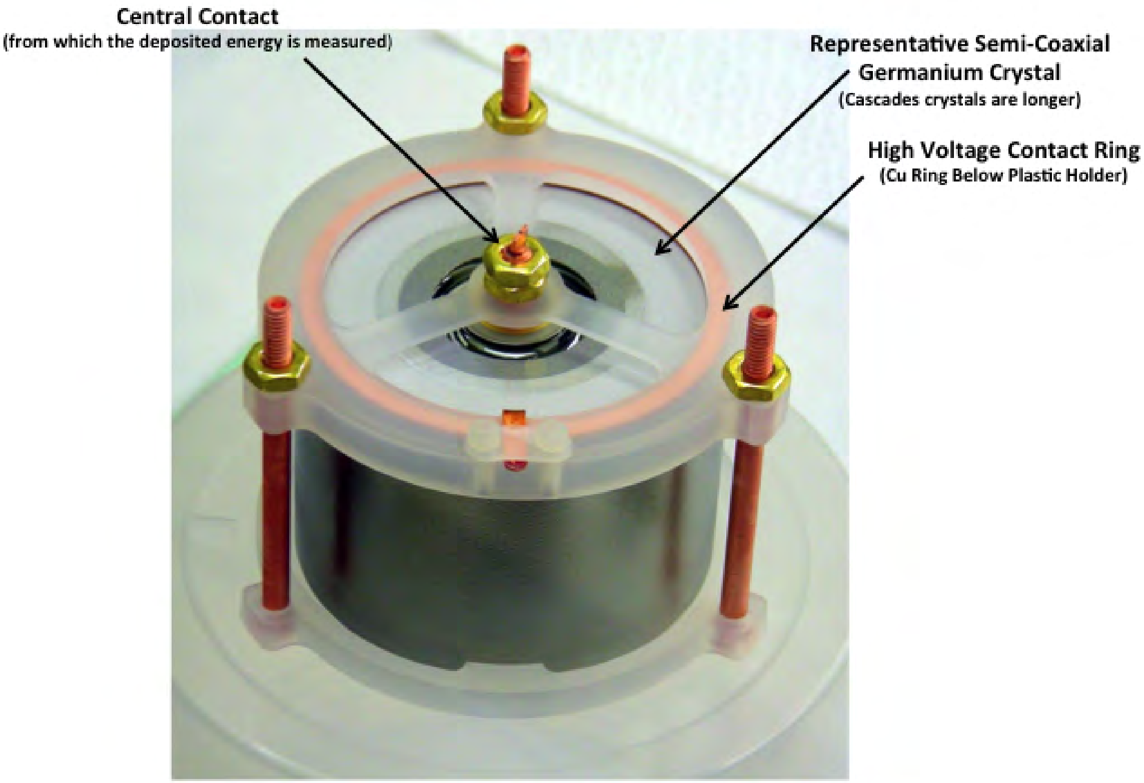

FIGURE 3.6. Mounting packages for individual crystals

With the exception of the IR shield and HPGe crystals, the first cryostat was assembled in 2009 with the installation of the Low-Background Front-End Electronics Package (LFEP), which will be discussed in Section 3.4, wiring, and preamplifiers [48]. Prior to installing the HPGe crystals, cryostat vacuum and thermal performance were tested successfully (see section 3.3). By mid-May of 2010, the first seven HPGe crystals were installed in the bottom cryostat following these steps: the cryostat was first disconnected from the dewar, then high-voltage (HV) wires were attached to the center connection of each crystal, fed through the appropriate hole in the cold plate and attached once again [50]. Electroformed nuts were used to bolt the crystals onto the coldplate, after which they were inverted one-by-one to allow crimping of the HV wire to leads attached to the gates of the LFEP [50]. Figure 3.7 details the installation of the HPGe crystals.

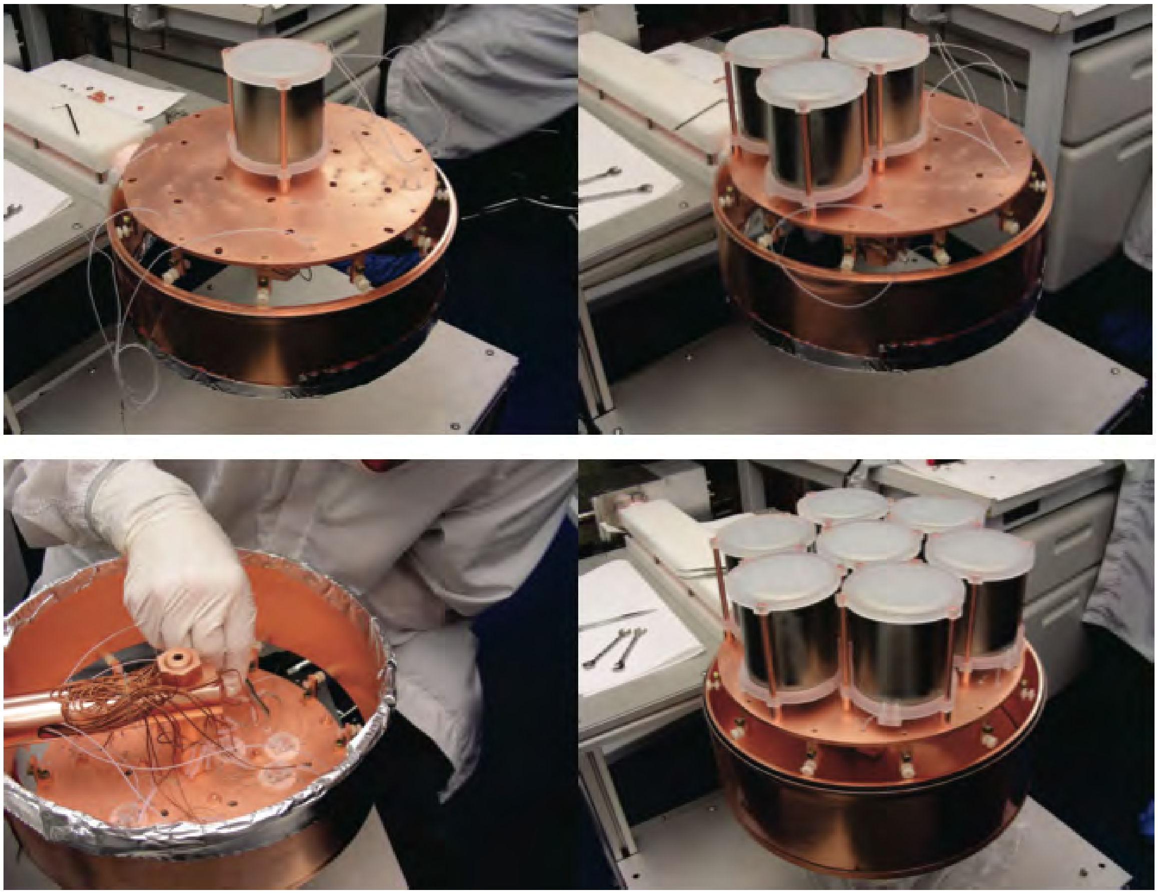

FIGURE 3.7. Installation of HPGe crystals and crimping of HV wires [50]

Electroforming the thin IR shields and domed entrance of the copper window was initially challenging due to the heating process used to remove the thin copper from the stainless steel (SS) mandrels. Removing an electroformed piece from its mandrel requires heating the piece to ∼300°C before rapidly cooling it in a bath of cold water. However since this proved to be problematic for parts electroformed on 304 SS mandrels, an alternative process was used. Hardened steel rollers were run over the surfaces of the electroformed IR shields, stretching the thin copper and thus removing it from the 304 SS mandrels [49]. The thin copper dished portion of the cryostat was electroformed separately and electron-beam welded onto an annular plate, producing a ∼0.04”-thick window over a 5”-diameter window [48], as shown in Figure 3.4.

Although the construction of the entire Cascades detector was originally scheduled to be completed in 2010, problems mentioned above and throughout this chapter delayed the completion of the project. The construction of the second array in 2012 was delayed when thermal testing of a custom commercial dipstick revealed the crystals would not reach a low-enough temperature at which to operate [51]. The temperature with no thermal load stabilized at 83 K; however when a 8.1 W thermal load was applied to the dipstick with a Zener diode, the temperature stabilized at 135 K [51]. Some further analysis indicated the problem laid with the diameter of the vertical portion of the cold path, hence a new dipstick had to be designed and fabricated at PNNL [51].

3.3. VACUUM AND THERMAL PERFORMANCE

A liquid-nitrogen dewar with a 100 liter capacity was custom-built by Technifab corporation and provides cooling for both cryostats [49]. The dewar, seen in Figure 3.8, uses about 1 kg of liquid nitrogen per day with no external load but around 7 liter/day when both cryostats are attached [50]. For proper thermal testing, a known thermal load was injected into the system with a Zener diode and measured by a Lakeshore silicon diode (located along the cold path

FIGURE 3.8. The liquid nitrogen dewar of Cascades prior to being attached to the lower cryostat with a thermal connection

from the dewar to the cold plate) and four silicon resistance temperature detectors (RTDs) located on the cold plate [49], [43]. Upon this initial test, it was noted the first cryostat did not cool sufficiently for the operation of the HPGe crystals, and also caused ice to form on the cross arm. The problem was identified as a thermal short between the horizontal cold finger and cross arm, caused by contact between the inner cold finger (kept at ∼87 K) and the cross arm (the outer vacuum jacket). Figure 3.9 illustrates this thermal short. This problem was resolved by modifying the section of the copper that directly connects to the dewar, or copper dewar extension, thus eliminating the thermal short between the cold finger and the cross arm [49]. The steel bolts fixing a clamp connecting the copper dewar extension to the cold finger were also changed from 304 SS to 18-8 SS [49]. After these changes, the cold plate reached a temperature of 89.5 K. The largest single temperature change across a material interface was reported to be ∼6 K; this was later improved by inserting gold foil at the dewar between the copper and aluminum [43].

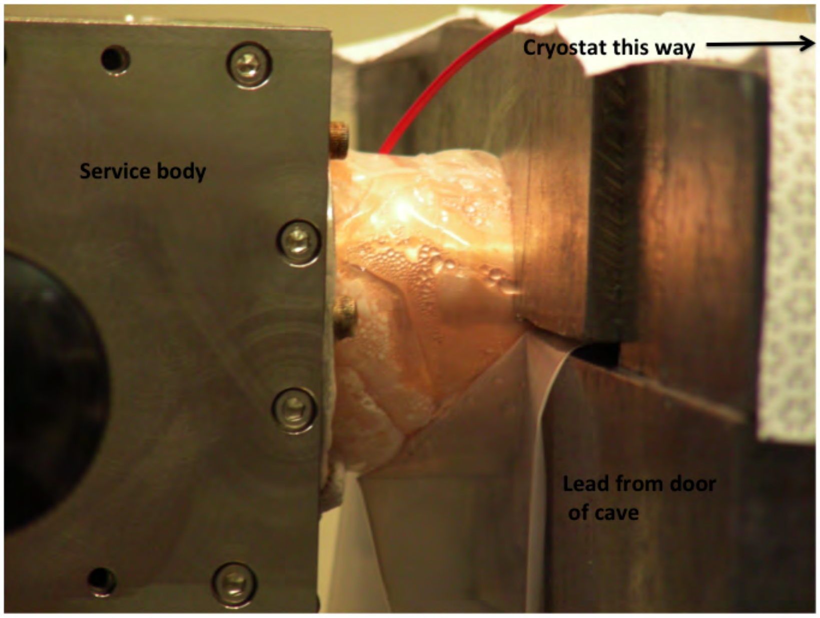

FIGURE 3.9. Ice on the cross arm after the first thermal testing

Additionally, the cryostats had to be tested for vacuum performance. In order to verify that a cryostat would not fatigue and fail under vacuum cycling, each cryostat was successfully cycled over 15 times [49]. Complications occurred with the installation of the first cryostat, as vacuum behavior was not as stable as predicted due to a loose vacuum flange [49]. Despite this, the array was successfully cooled to a temperature range of 82.5 K - 83.5 K at the copper dewar extension [49]. The HPGe crystals were then installed as discussed in Section 3.2.

3.4. LOW-BACKGROUND FRONT-END ELECTRONICS PACKAGE

Since HPGe detectors produce signals much too small to be directly measured, amplification is required to measure energies deposited in the crystals. In HPGe detector systems, this amplification occurs in two stages. The first stage is a low-level amplification, generally referred to as the “front end”, that occurs very close to the HPGe crystal so as to avoid the introduction of noise. The second stage further amplifies the signal to a degree at which the signal can be measured using modern data acquisition electronics. Since the front-end is positioned only a few centimeters away from the front of a crystal, the radiopurity of the front-end is extremely important; however, its mix of active and passive electronic components presents a bigger radiopurity challenge than electroforming the more massive copper cryostat parts [1]. Because commercial solutions are not available, custom solutions have been developed at PNNL to address this issue. Front-ends have been developed starting with commercial units and have evolved to other designs of Low-background Front-end Electronics Packages. This design evolution can be observed in Figure 3.10. For Cascades, the LFEP-II front-end was used (see Figure 3.11). Figure 3.12 illustrates a close-up on the sockets into which the LFEP-II boards are mounted with the components facing into the sockets. Figure 3.13 shows the location

FIGURE 3.10. Evolution of LFEPs from commercial units to LFEP-II for Cascades [49]

of the boards in relation to the crystals, which are hanging "down", or into the page. While it is possible to produce front-ends from low-background components, it is not yet possible to produce the second stage of amplification in similar fashion. This complication is driven by the nature of the modern amplifier design. As a result, the second stage of amplification in low-background HPGe systems must be placed away from the crystals. In the case of the Cascades detector, the second stage occurs outside of the lead shield and consists of 14 RG11B/C charge-sensitive preamplifiers from Princeton Gamma Tech (with one preamplifier per crystal). A close-up of the preamplifiers and their location with respect to the germanium components are seen in Figures 3.14 and 3.15.

To measure events, a charge-integrating loop is formed by HPGe amplifiers and LFEP units, which convert charge deposited in germanium crystals

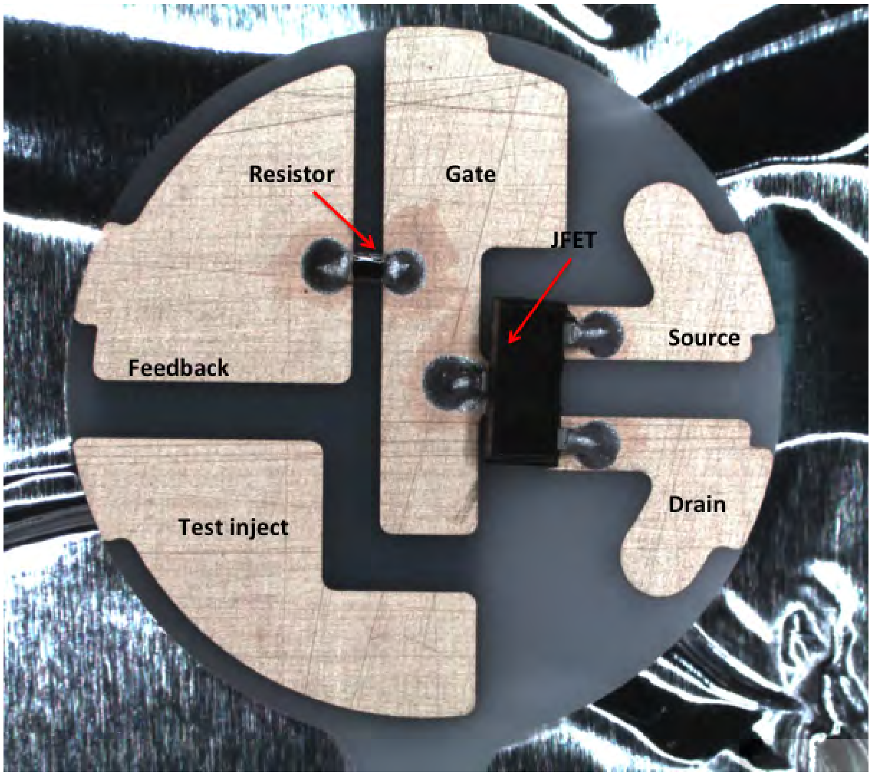

FIGURE 3.11. Assembled LFEP-II board

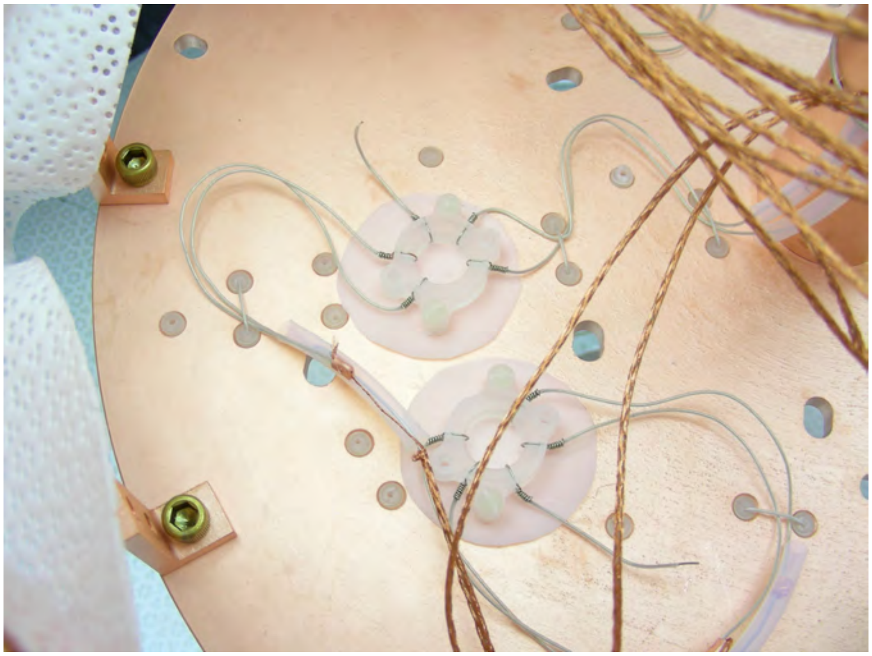

FIGURE 3.12. Close-up of sockets into which LFEP-II boards are mounted

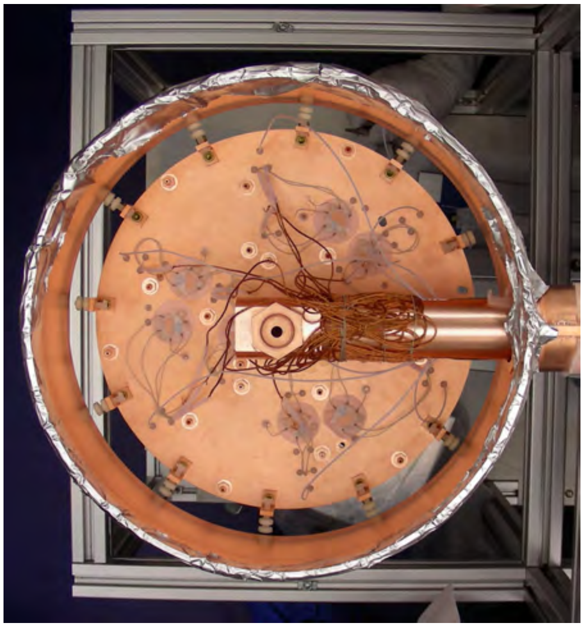

FIGURE 3.13. Location of LFEP-II boards in relation to the crystals, which are pointing into the page

FIGURE 3.14. Close-up of a RG11B/C preamplifier

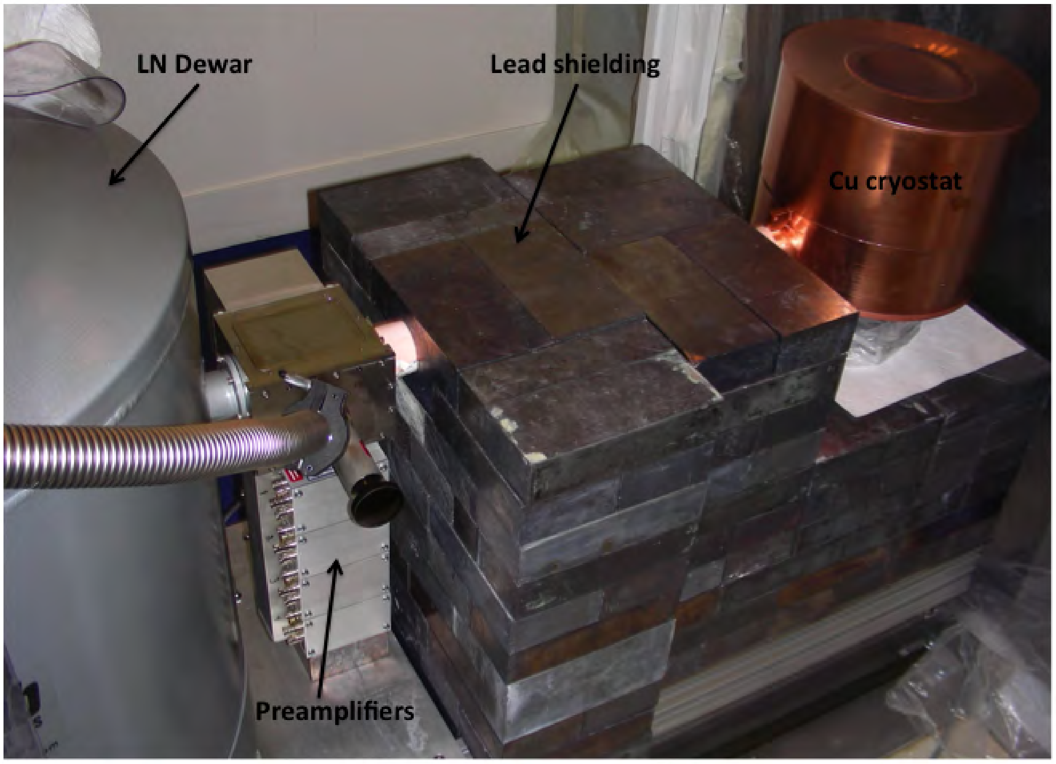

FIGURE 3.15. Location of RG11B/C preamplifiers with respect to the sensitive germanium elements

by ionizing radiation into a voltage change that is measured by digitizers described in Section 3.6. A representative circuit design of the LFEP is illustrated in Figure 3.16.

3.5. PASSIVE AND ACTIVE SHIELDING

To shield from environmental and cosmic backgrounds, the Cascades detector is operated at a depth of ∼35 meters water equivalent, and both active and passive shielding are used. The detectors are shielded by 10” of lead and copper. Lead-210 shields against ^{238}U and ^{232}Th backgrounds, while its innermost ∼2”-copper layer shields the detector from the ^{210}Pb bremsstrahlung resulting from the use of modern lead. The need to perform detector maintenance or to

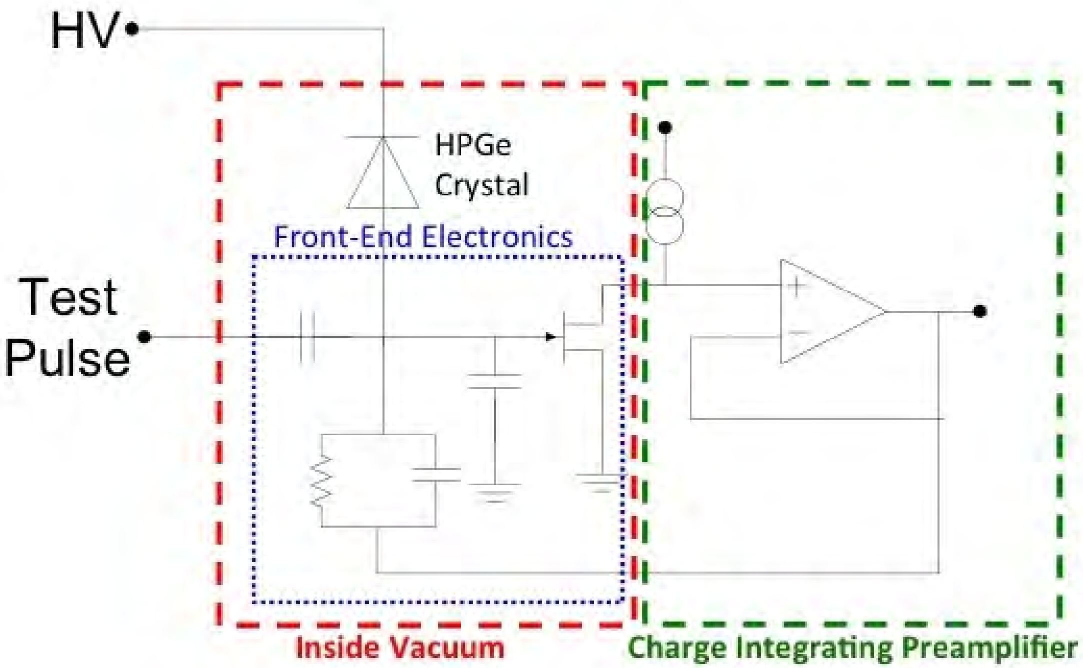

FIGURE 3.16. Circuit design of the LFEP

place a variety of samples in the detector is achieved by rolling the lead door out of the shield with the use of an electric motor [48], as seen in Figure 3.17. Because of the movable door, pieces of extruded aluminum are used at the bottom to raise the lead off the floor as well as for structural support. The lead shield is wrapped in a thin layer of cadmium (Figure 3.18), which serves to capture neutrons that are thermalized by the 6” of high-density borated polyethylene located outside the lead (Figure 3.19). In order to properly purge radon from the system, an enclosure surrounds the lead. Although this portion of the shield was designed to be sealed tightly, the radon enclosure of Cascades is not yet fully operational at this writing; however, boil-off gas nitrogen gas from a much larger dewar is used to purge the system at a rate of 9 SCFH (standard cubic feet per hour).

The goal of the active cosmic veto shield is to detect and exclude cosmic-ray generated interactions with germanium. In the case of Cascades, 15 BC-408

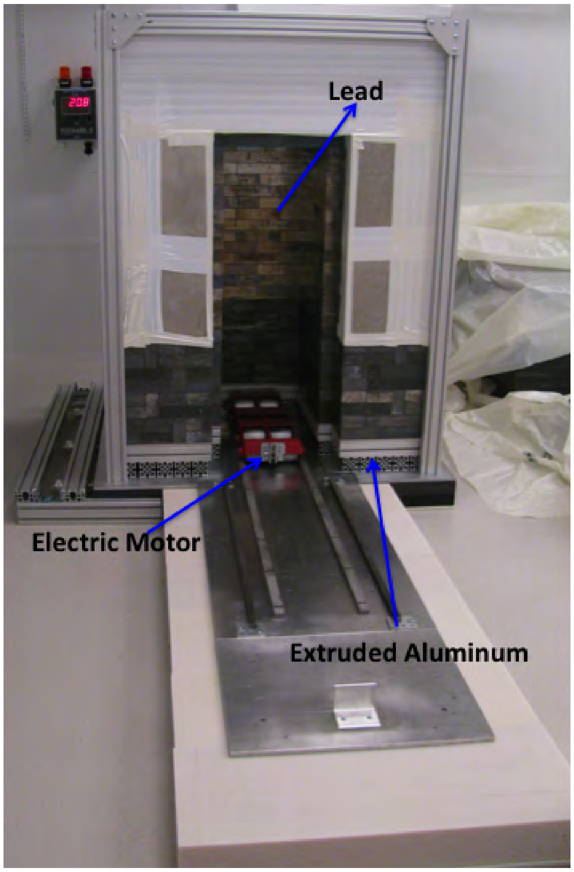

FIGURE 3.17. Electric motor used to roll the lead door in and out of the cave

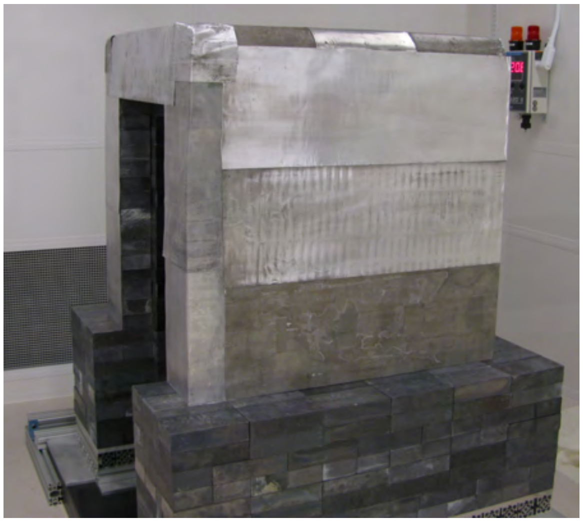

FIGURE 3.18. Lead shield wrapped in a thin layer of cadmium

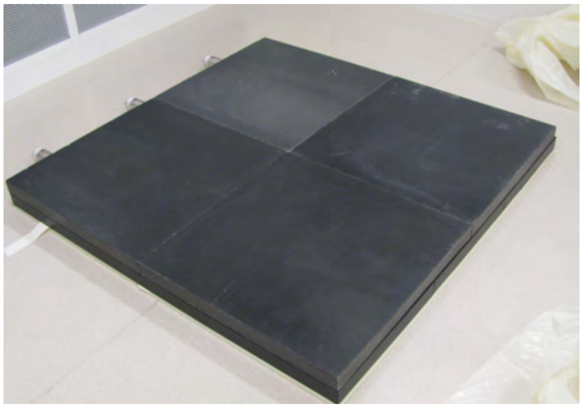

FIGURE 3.19. Sample of high-density borated polyethylene

plastic scintillator panels each measuring approximately 17.5” x 2” x 70” surround the lead shield and the door side of the detector [50]. To detect scintillation light, a single photomultiplier tube is mounted to the end of each veto panel. Three veto panels are required to cover each side of the Cascades shield. A preamplifier (Camberra model 2005) re-combines the three signals from each side, which are then read out by an XIA PIXIE-4 waveform digitizer [49]. Figure 3.20 illustrates a typical energy spectrum produced by one side of the cosmic-ray veto after matching the individual PMT gains through bias adjustments.

An excellent time resolution of a veto system is extremely important since it will decrease the inclusion of false events. The original time resolution of the veto system of Cascades was 200 ns, however the anti-coincidence window was later significantly widened to ±1 μs to decrease background [49]. The 511 keV annihilation peak was measured to be suppressed by 94.2% [50]. The background rejection rate efficiency was at first measured at 73% and was primarily dominated by ^{210}Pb-associated bremsstrahlung and radon daughter isotopes ^{222}Rn and ^{220}Rn [50]. Since this measurement, the ^{210}Pb-associated continuum has been further reduced with the addition of thick copper lining measuring slightly less than two inches [50]. Today background rates range at an average of 347 counts (keV-y-kg)$^{-1}$ in the 40-2700 keV range. Some background peaks

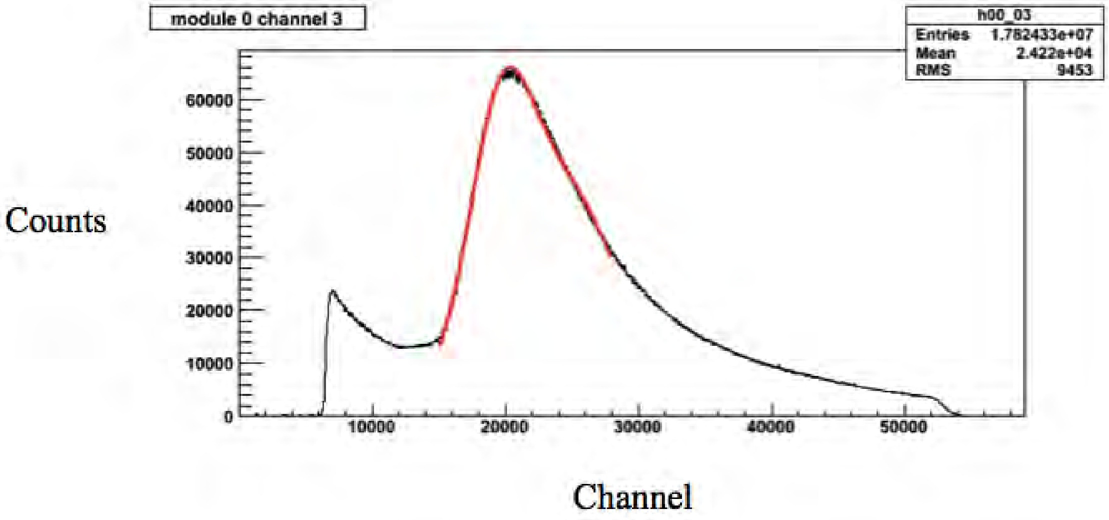

FIGURE 3.20. Muon-spectrum collected by active-veto on the top surface of the lead shield [49]

and "shark fins" associated with neutron interaction with germanium can be observed in Figure 3.21. Background features include the continuum, radon daughters ^{222}Rn and ^{220}Rn, ^{210}Pb x-rays, the 511 keV annihilation peak and other peaks from the neutron activation of germanium and lead.

3.6. DATA ACQUISITION AND ANALYSIS FRAMEWORK

The data acquisition pathway of Cascades begins near the crystal where sockets for the PNNL Low-Background Front-End Electronics Packages (LFEP) are mounted onto the cold plate. The very small signal from each detector is modestly amplified by an LFEP, as discussed in Section 3.4, and then sent through a Belden 8700 micro coaxial cable to a 50-pin vacuum feedthrough connector located on the service body (refer to Figure 3.12). In order to mitigate radioactive backgrounds, the PVC jacket of the Belden cable was removed. On the non-vacuum side of the 50-pin feedthrough, the signal is routed to a PGT RG11B/C charge-integrating preamplifier located on the distribution box mounted to the bottom of the service body. There are seven preamplifiers per

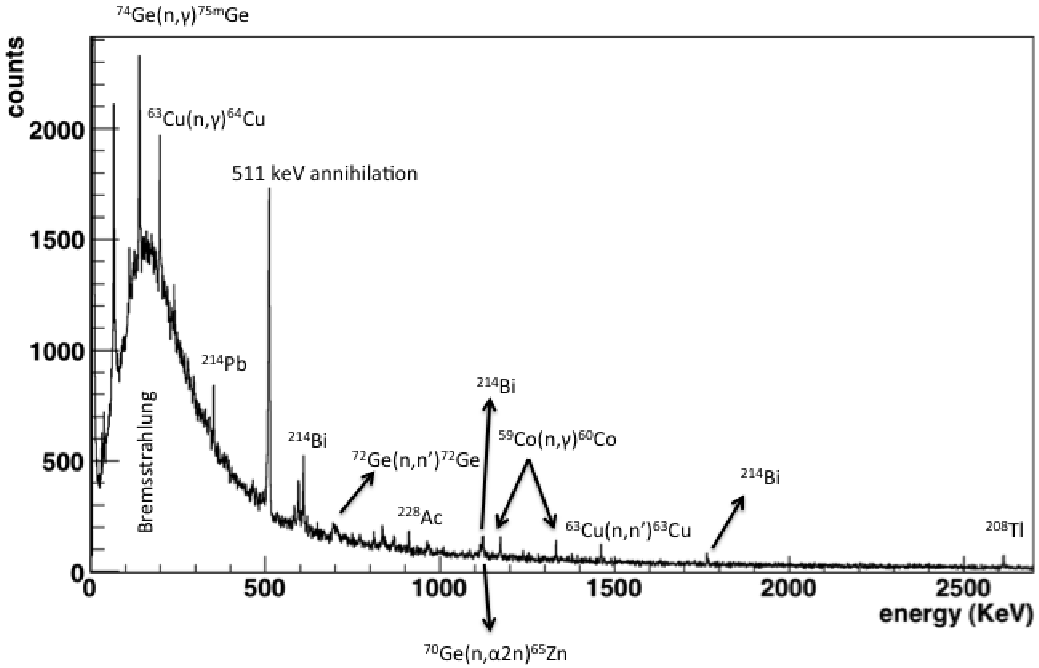

FIGURE 3.21. Background features observed in a 16.59-day background run measured with the 2 arrays of Cascades

box and one preamplifier per crystal, such that the signals from each of the 14 preamplifiers (for all 14 crystals) are digitized by an XIA Pixie-4 waveform digitizer. For Cascades, a total of five Pixie-4 4-channel digitizers are used, while the additional Pixie-4 channels are used for the veto scintillators.

A Linux-based in-house data acquisition program called NXY controls the DAQ hardware [23]. Data collection is operated by NXY and permits the user to generate basic MCA-style spectra with time and energy values for each crystal, and also has the capability of digitizing waveform data for each observed pulse [43]. Coincident hit pattern information is also recorded with NXY [50]. The data acquisition system described above permits event data from the 14 crystals of Cascades to be reconstructed in several ways. The Cascades analysis software, called “Melusine”, was developed using the C++ programming language and relies on the library tools provided by the ROOT framework [22] and on Qt for graphical user interface functionality [49]. The PNNL data acquisition software NYX receives binary data produced by PIXIE-4 digitizers and stores these data on disk [50]. The binary data are then processed using Melusine1, a preprocessor that converts XIA data format to a ROOT data structure. Melusine2, the analysis code, provides the functionality to produce histograms for individual and summed crystals. Figure 3.22 illustrates this multi-step process.

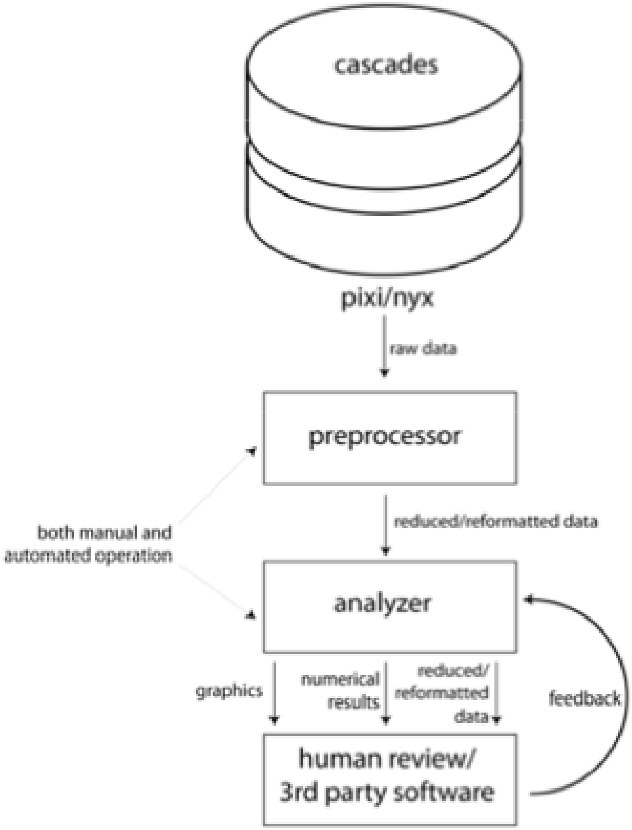

FIGURE 3.22. Cascades data processing steps [50]

Melusine2 creates configuration files that allow the user to select exactly which histograms and analyses are desired, such as performing energy calibrations, identifying isotopes, and extracting their activities and peak efficiencies from analyzing one or two-dimensional spectra. Options include establishing coincidence requirements, cuts, fits, and calibrations by either editing configuration files or using a graphical user interface (GUI). Spectra can also be restricted based on graphical cuts, channel, multiplicity, energy range, veto status and other features extended in the analysis framework of ROOT.

The Melusine software is flexible in its usage. With well-defined ROOT tree forms, the user can quickly examine the validity of data and produce simple histograms with minimal effort before diving into an extended analysis. Another clear advantage is the separation of the data formatting from the analysis tools (Melusine1 versus Melusine2); this allows the system to handle data produced by other sources such as simulations or has the potential for decoding data from other types of detector arrays [50]. Additionally, a straightforward isotope identification algorithm has been implemented in Melusine based on nuclear data files written by the Coincidence Lookup Library (CLL) [73]. This portion of the code scans an energy spectrum and identifies isotopes based on observed lines or specified centroid energy criteria [51]. In order to perform this extensive analysis, a mixed isotope standard suitable for the energy calibration of complex detectors was utilized with a single measurement and used to calibrate spectra. This will be discussed further in Chapter 5 with reference to background and calculating activities from primordial radiation in the Cascades detector.

Fitting algorithms for doublet and multiplet peaks based on Gaussian peaks and linear backgrounds were also implemented in Melusine, based on the code's ability to recognize overly-broad peaks and split them consequentially [51].

Figure 3.23 demonstrates the ability of Melusine to perform automated multiplet fitting of ^{143}Ce, ^{95}Zr and multiple ^{132}I peaks. Other code features such as adaptive ROI fitting to avoid poor background continuum caused by neighboring peaks can also be observed [51]. If the peaks under consideration are within the displayed energy range, they are also highlighted (in green with regards to Figure 3.23) by the user interface.

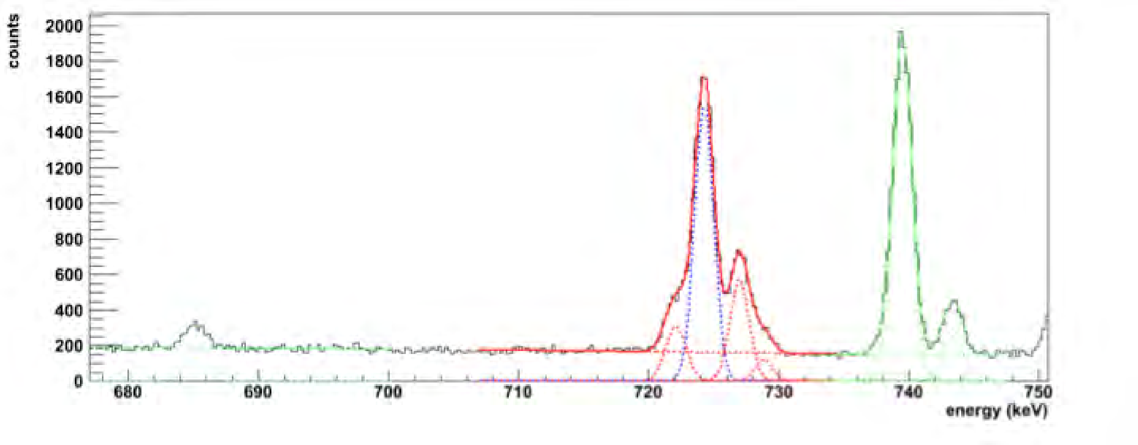

FIGURE 3.23. Multiplet fitting of Melusine code [51]

3.7. SUMMARY

As discussed in this chapter, the construction of Cascades was delayed significantly due to unforeseen problems in thermal and vacuum testing, copper electroforming, and detector assembly. A variety of measurements have been made and analyzed to date, such as standard calibration sources, mixed fission product samples, neutron activation samples, and Fukushima-related sea life samples. To illustrate the measurement sensitivity of Cascades, minimum activities of ~2 mBq for ^{60}Co and ^{137}Cs were detected by a 7-day measurement of ultra-high-molecular-weight polyethylene with the lower array [51]. Activity calculations for both single and coincident signatures, efficiency calculations, and decay calculations for half-life data can be extracted based on the CLL and Melusine algorithms. Although Melusine today shows great progress and potential, future work such as tailing functions, stepped backgrounds, more efficient coincidence analysis techniques, error propagation and other additions should be implemented to complete the software. Other tests and simulations were conducted to determine the suitability of the Cascades detector for the measurement of rare events, as will be discussed in Chapters 4 and 5.

CHAPTER 4

SIMULATIONS

4.1. PERFORMANCE MODELING

A model of the Cascades detector was built using GEANT4 (Geometry and Tracking) [67], a C++-based simulation framework that relies on random sampling by using computational algorithms to simulate the interaction of particles with matter. In this section, the configurations of the model are discussed and simulations of ^{137}Cs γ-rays are presented for validation purposes.

4.1.1. GEANT4 Model. The GEANT4 Cascades geometry consists of two arrays of seven semi-coaxial p-type HPGe crystals looking head-on. Figure 4.1 shows a cross-section view of the Cascades detector in between the center of the two arrays. It is important to note in this diagram that colors do not represent

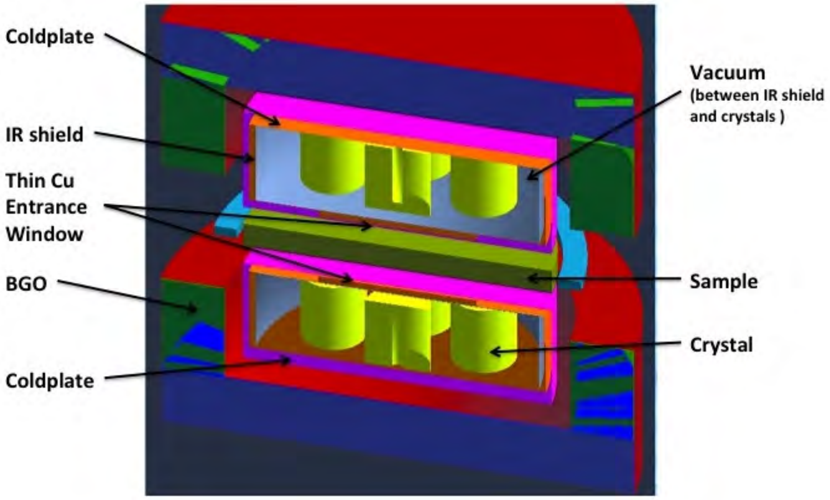

FIGURE 4.1. Cross-section view of the Cascades detector with radioactive sample in between the two arrays

specific parts of the detector, but rather boundaries between different materials. Several features of the cryostat mechanical design have been simplified in the GEANT4 model in order to reduce complexity. Attention was focused on ensuring that the crystals were located at the right coordinates and that the copper thickness was as accurate as possible. Details such as the three copper rods that are part of the crystal mount were neglected due to their low mass in comparison to the remainder of the copper in the cryostat.

In the GEANT4 model shown in Figure 4.1, the magenta represents the outer boundary of the 5-mm vacuum jacket and the orange represents the inner boundary. The space between these two bounding surfaces is defined in GEANT4 to be copper. Features such as the thin copper entrance window (with diameter 149.5 mm) are shown as a reduction in the distance between the outer magenta and inner orange surfaces. The thickness of the cold plate on the rear side of the crystals can be seen by the increase in the separation of these two surfaces. The grey shell between the copper and the crystals (yellow) is the thin 0.1-mm thick copper IR shield. All crystals are simulated with the same dimensions: 62 mm in diameter and 70 mm in height, which includes a dead layer of 0.25 mm. This is a representative size for the actual crystals. The BGO (Bismuth germanium oxide scintillator) anti-Compton shield is present to catch higher energetic events that scatter outside of the array.

4.1.2. Validating the GEANT4 Model. In order to validate the GEANT4 model of Cascades, the radioactive decay of ^{137}Cs was simulated using GEANT4 with radioactive decay data obtained from the PNNL Coincidence Look-up Library (CCL) [73] and compared to actual measurements made with the detector.

Cesium-137 β-decays to ^{137}Ba by emitting a β-particle (E_β = 513.97 keV) and a γ-ray (E_γ = 661.61 keV) with an 85.1% probability as seen in Figure 4.2. A point source of ^{137}Cs with an activity of 0.669 μCi at the time of measurement

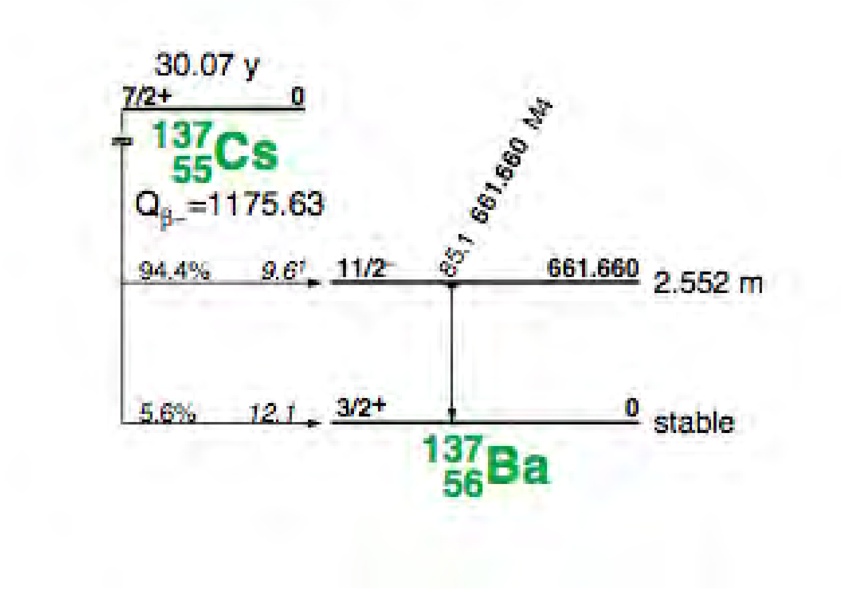

FIGURE 4.2. Decay Scheme of ^{137}Cs [31]

was placed on the face of the detector above the center crystal (Crystal 1) and two outer ring crystals (Crystal 2 and Crystal 4), then raised by 1”, then 10” above the detector face and the outer ring crystals (refer to Figure 4.3 for a vizualisation of the numbered crystals in the bottom array). These nine runs

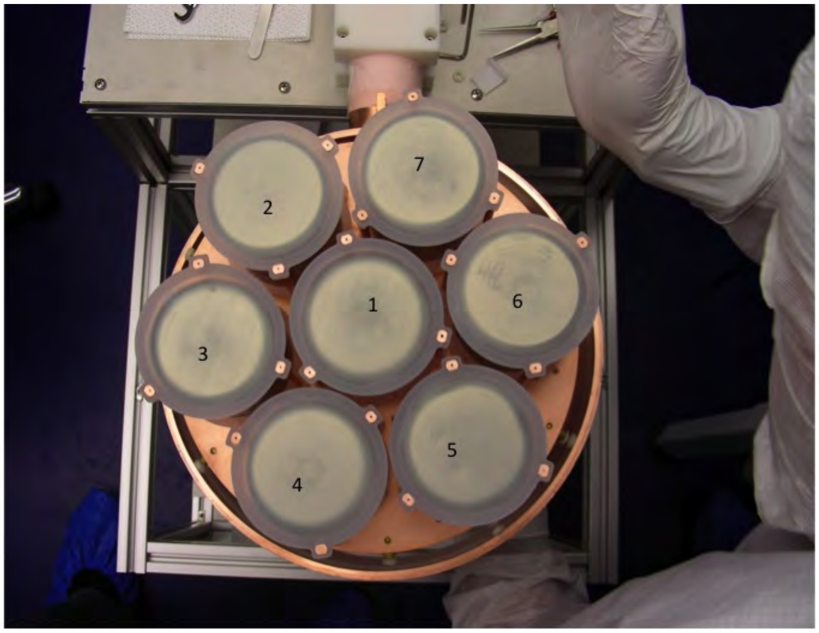

FIGURE 4.3. Numbered crystals in bottom array of Cascades

lasted 300 seconds for the on-face and 1” positions, and 600 seconds for the 10” positions with an average ~83.4% live time. Using live times, the number of γ-rays emitted based on the source activity, and peak areas and background subtractions extracted from Melusine, the software developed for Cascades (refer to Chapter 3), experimental peak efficiencies for the 661.66 keV energy peak were calculated.

At the time of this experiment, only the lower array of the Cascades detector was functional, hence one array was turned off while running simulations in order to replicate the measurements with accuracy. To obtain high-enough statistics, millions of decays were simulated for each position. These decays were emitted isotropically from a ^{137}Cs disk measuring 0.5 cm in diameter and 0.318 cm in thickness. These data files were then converted from ASCII to ROOT files with a ROOT macro, in which events forming the 661.66 keV peak were summed for each individual crystal. Peak efficiencies were calculated based on the detected number of events while subtracting a linear background estimate for the 661.66 keV region. Figure 4.4 shows an example of simulating a ^{137}Cs source placed 10” above Crystal 4 and generating a spectrum from summing the events recorded in Crystal 1. The 661.66 keV peak can be observed, as well as the continuum spectrum to the left. A linear background estimate is subtracted and calculated from averaging counts that border the left of the peak area (the continuum).

To calculate peak efficiencies for the total array, two summing methods were implemented. In the first method, referred to as “Total1”, the histogram is filled with energies deposited in each crystal; hence for one 7-crystal array, the histogram could be filled up with a maximum of seven values for one event. In the second method, referred to as “Total2”, energies deposited in each of the seven crystals are added before filling the histogram. With Total2, the true energy of an incident γ-ray that undergoes Compton scattering can be reconstructed

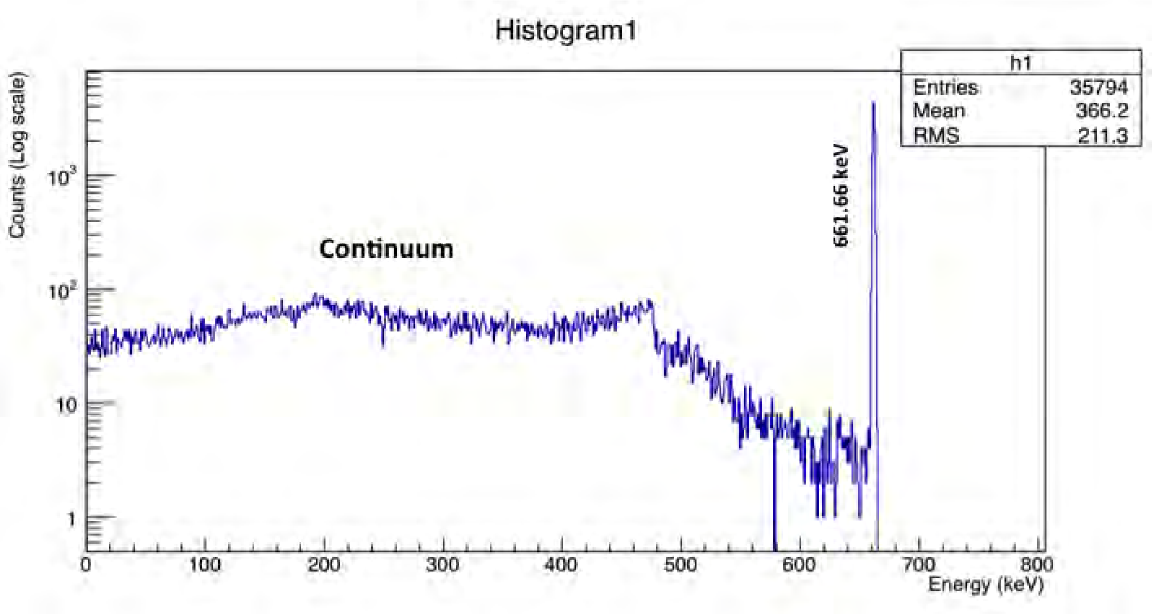

FIGURE 4.4. Events summed in Crystal 1 from simulating the decay of a ^{137}Cs source placed 10" above Crystal 4

by adding the energies of different crystals together. The disadvantage of this method arises when multiple γ-rays are incident on multiple crystals in the array for a given event. This might occur in the case of a γ-γ coincident decay, such as in ^{60}Co. In this example, adding the 1173 keV event to the 1332 keV event would reduce the detection efficiency of the individual gammas since they are summed-out of their respective peaks. Keeping this in mind, analysis and summing methods should be carefully considered and picked appropriately depending on the efficiencies they yield. Figure 4.5 shows an example of an experimental energy peak resulting from placing a ^{137}Cs source on the face of Crystal 1, then adding the events with the Melusine software from all seven crystals using the Total2 summing method. Abbreviated results comparing experimental and simulated efficiencies of individual Crystals 1 and 2 (Xtal1 and Xtal2) are shown in Table 4.1, as well as the total array efficiencies (Total1 and Total2) for two of the three positions. The percentage deviation between experimental and simulated efficiencies is calculated for validation purposes.

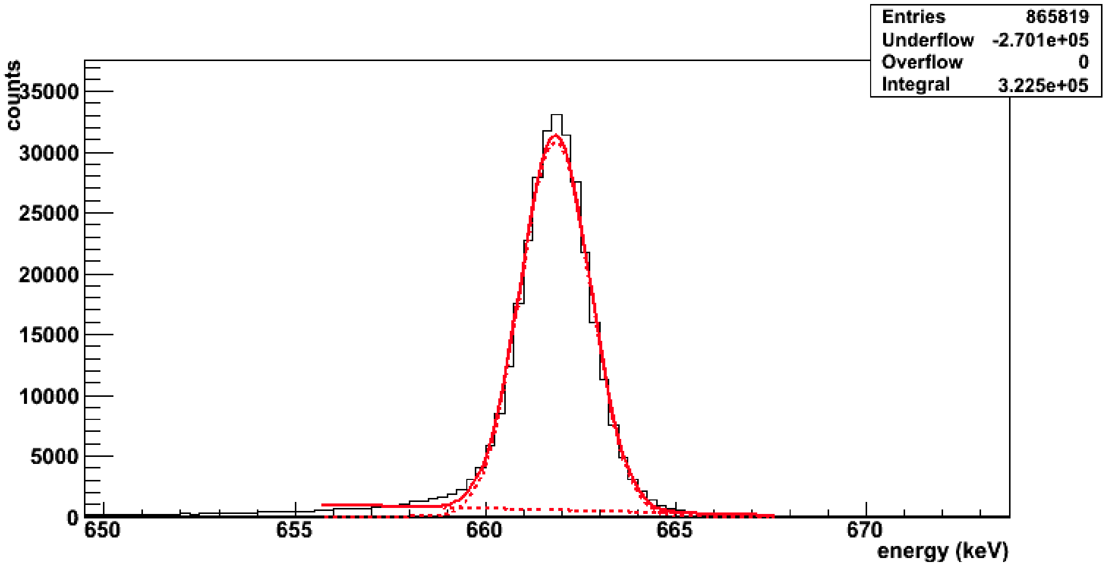

FIGURE 4.5. Experimental 661.66 keV peak in 7 crystals fitted with Melusine

4.2. SIMULATIONS OF PRIMORDIAL BACKGROUND

Chapter 2 explained in depth how primordial radiation can contaminate ROIs with the decay products of ^{232}Th and ^{238}U chains. This section focuses on simulating isotopes from these chains assuming an even distribution of ^{232}Th and ^{238}U in the copper cryostat of Cascades in order to determine if there are other main sources of primordial radiation present in the detector.

An engineering drawing of the lower cryostat can be observed in Figure 4.6. Based on these dimensions and the density of copper, each cryostat was determined to have a total mass of approximately M = 15238.85 grams and was constructed with GEANT4 in four distinct parts: the sidewalls (with m_1 = 4316.67 g), the thick entrance window (m_2 = 3406.01 g), the thin entrance window (m_3 = 106.510 g) and the coldplate (m_4 = 7409.66 g), with $M = m_1 + m_2 + m_3 + m_4$. These four parts were then coded as containing uniformly distributed primordial radioactive sources, i.e.- radiation from the ^{232}Th and ^{238}U chains was emitted from the copper cryostat itself in the simulations rather than from a source positioned above the HPGe crystals. Background events

TABLE 4.1. Experimental vs. simulated efficiencies (ϵ) in Cascades for the decay of ^{137}Cs. Xtal1 and Xtal2 refer to efficiencies of the individual crystals.

Position of sample	Analysis method	Exp.ϵ	Sim. ϵ	% dev.
Face Xtal1	Total1	0.04311 ± 0.00024	0.04204 ± 0.00006	2.5467
	Total2	0.04138 ± 0.00023	0.04107 ± 0.00005	0.74787
	Xtal1	0.01491 ± 0.00009	0.01481 ± 0.00003	0.61980
	Xtal2	0.00441 ± 0.00003	0.00440 ± 0.00002	0.26583
1” off Xtal1	Total1	0.03587 ± 0.00021	0.03585 ± 0.00006	0.06642
	Total2	0.03858 ± 0.00022	0.03850 ± 0.00006	0.21688
	Xtal1	0.00914 ± 0.00006	0.00913 ± 0.00003	0.13435
	Xtal2	0.00414 ± 0.00003	0.00412 ± 0.00002	0.38797
Face Xtal 2	Total1	0.02403 ± 0.00014	0.02336 ± 0.00004	2.8665
	Total2	0.02585 ± 0.00015	0.02493 ± 0.00004	3.6891
	Xtal1	0.00411 ± 0.00003	0.00401 ± 0.00002	2.4659
	Xtal2	0.01049 ± 0.00007	0.01015 ± 0.00003	3.3028
1” off Xtal 2	Total1	0.01999 ± 0.00012	0.01958 ± 0.00004	2.1050
	Total2	0.02184 ± 0.00013	0.02122 ± 0.00004	2.9330
	Xtal1	0.00395 ± 0.00003	0.00389 ± 0.00002	1.5860
	Xtal2	0.00551 ± 0.00004	0.00537 ± 0.00002	2.6289

were simulated using input files coded with information from the Coincidence Lookup Library [73] and the Table of Isotopes [31]. The γ-rays with the highest intensities and probabilities of being observed in primordial background spectra are presented in Table 4.2.

In order to normalize the events to the total mass M of the cryostat, a specific number of events was generated for each cryostat part based on its fraction of the total mass. The four cryostat parts were summed together for each individual chain, resulting in two separate ^{232}Th and ^{238}U background spectra (see Figures 4.7 and 4.8). To sum the events of the background, an additional summing method was implemented, which will be referred to as “Total3”. The

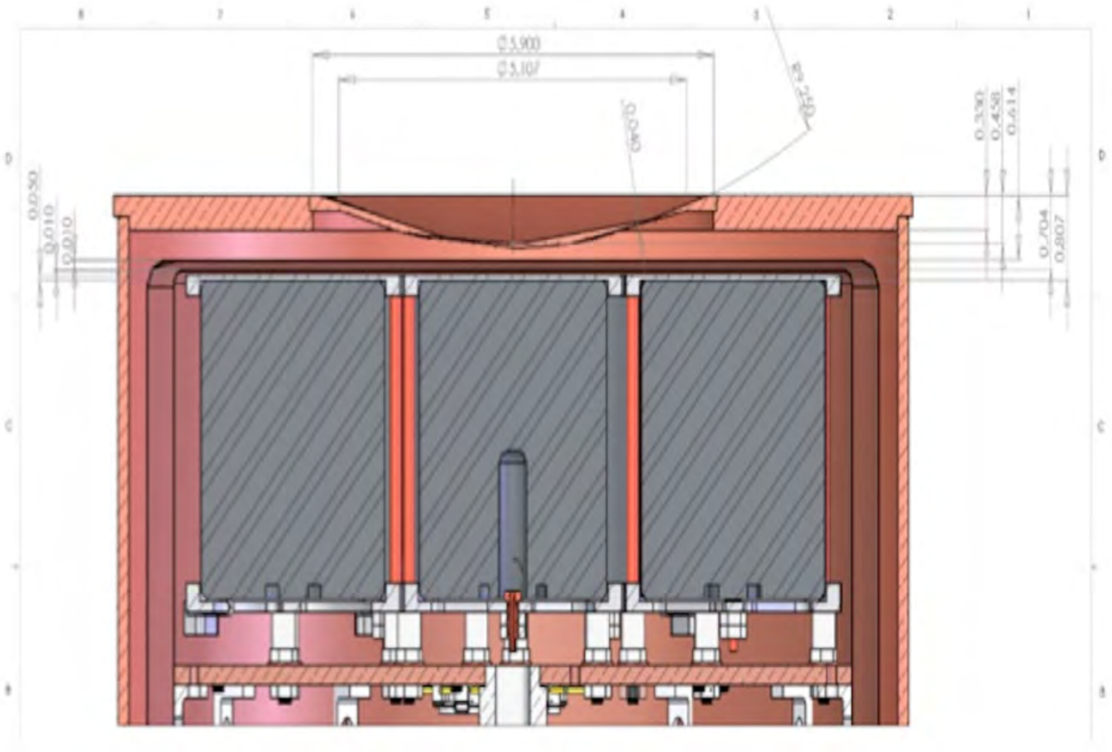

FIGURE 4.6. Cross-sectional view of lower cryostat with dimensions

TABLE 4.2. Prominent energy lines from primordial radiation chains

Parent Isotope	Daughter Isotope	Energy (keV)	Relative Intensity (%)
^{232}Th	^{228}Ac	911.2	26.6
^{232}Th	^{228}Ac	969.0	16.2
^{232}Th	^{208}Tl	583.2	84.5
^{232}Th	^{208}Tl	2615.5	99.0
^{238}U	^{214}Bi	609.31	44.8
^{238}U	^{214}Bi	1120.29	14.8
^{238}U	^{214}Bi	1764.49	15.4

Total3 summing method treats the two arrays as a single detector by summing the events in all 14 crystals before filling energy histograms in ROOT. A final simulated background spectrum was generated by adding the two ^{232}Th and ^{238}U background chains together, as seen in Figure 4.9. Analysis of these

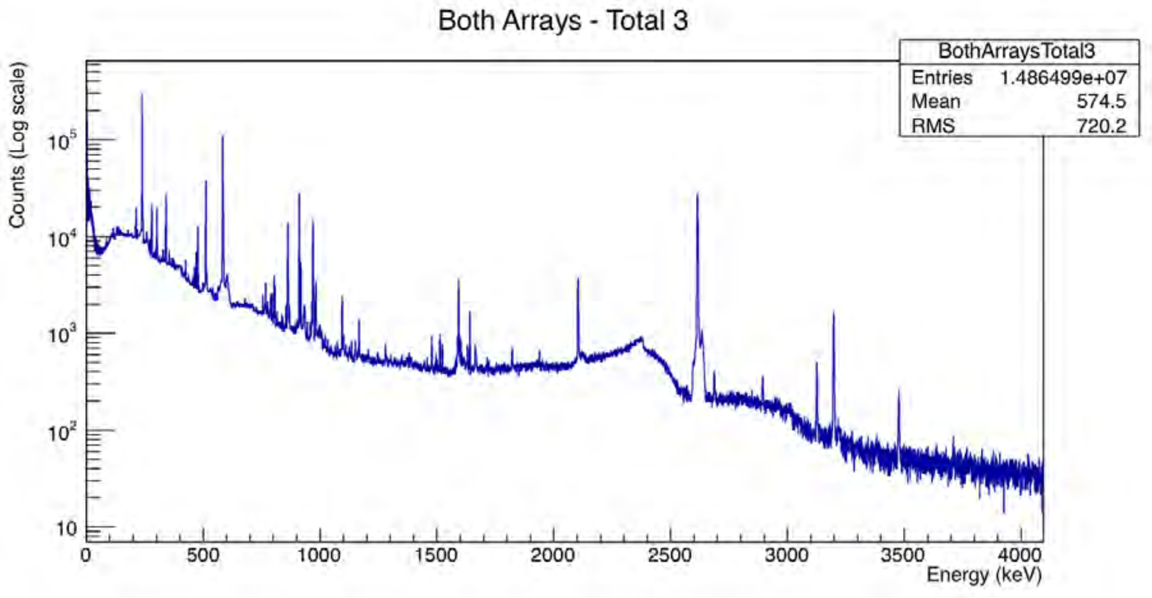

FIGURE 4.7. Simulated background from ^{232}Th decay chain

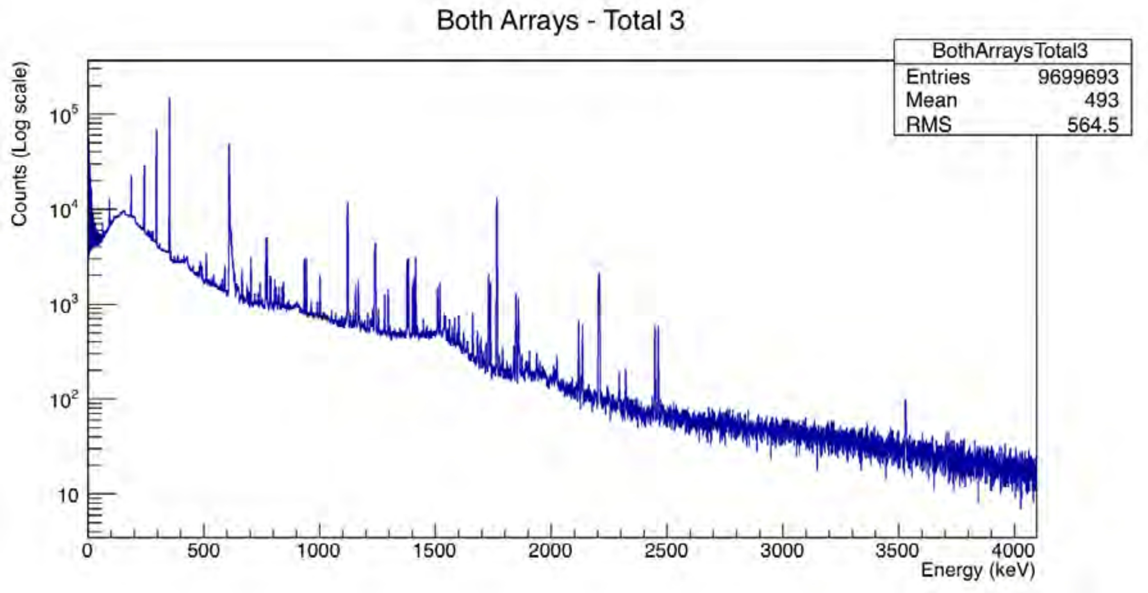

FIGURE 4.8. Simulated background from ^{238}U decay chain

simulations and comparison to experimental background spectra with calculated ^{232}Th and ^{238}U activities present in the Cascades detector will be shown in Chapter 5.

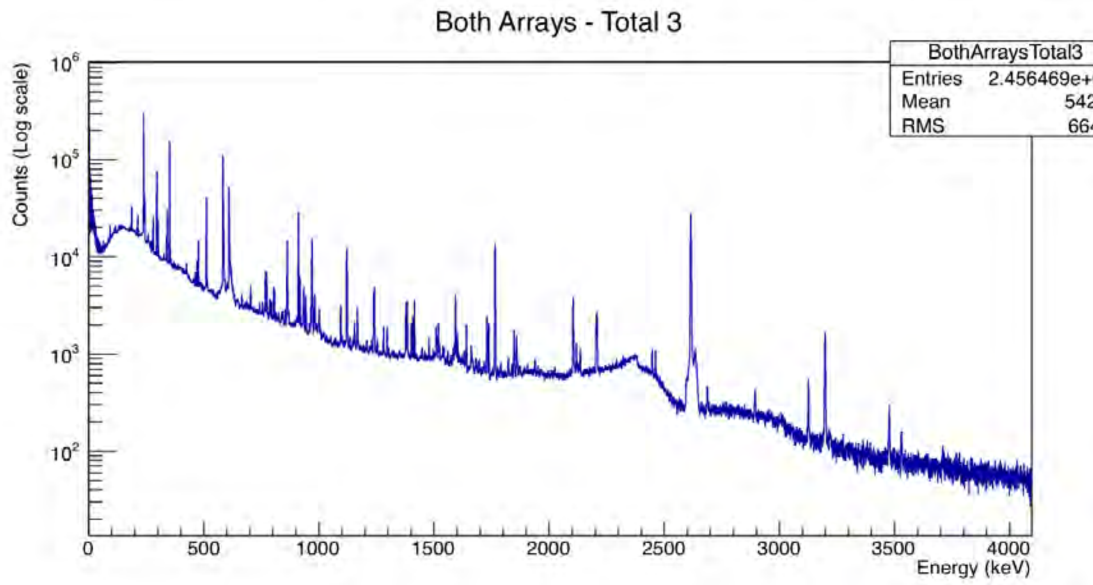

FIGURE 4.9. Simulated background from primordial radiation (^{232}Th and ^{238}U chains)

4.3. SIMULATIONS OF TELLURIUM-130

In this section, the possibility of detecting rare events such as $\beta\beta$-decay with the Cascades detector is discussed, using the $0\nu\beta\beta$-decay of ^{130}Te to the first excited 0_1^+ state of ^{130}Xe as an example.

4.3.1. Tellurium-130. As seen in Chapter 1, the goal of searching for $0\nu\beta\beta$-decay is to probe an absolute neutrino mass scale suggested by the mass-splitting parameters observed by neutrino oscillation experiments. Furthermore, observation of $0\nu\beta\beta$-decay is an explicit instance of Lepton-number non-conservation. The half-life $T^{0\nu}_{1/2}$ of the decay is expressed as follows: [52]:

$$[T^{0\nu}_{1/2}]^{-1} = G_{0\nu}(Q_{\beta\beta}, Z)|M_{0\nu}|^2\langle m_{\beta\beta}\rangle^2 \, , \qquad (16)$$

where $G_{0\nu}(Q_{\beta\beta}, Z)$ is the phase space factor for the emission of the two electrons, $M_{0\nu}$ is the 0ν nuclear matrix element, and $\langle m_{\beta\beta}\rangle$ is the effective Majorana mass of the electron neutrino. Studies of $0\nu\beta\beta$-decay have recently been extended to include transitions to excited final states. A transition to the 2_1^+ state is unlikely to be detected due to angular momentum suppression [12], so efforts have shifted to studying the $0\nu\beta\beta$-decay to the first 0_1^+ excited state of a daughter nuclide. Since decays to the excited state imply smaller transition energies, the probability of occurrence is suppressed in comparison to a transition to the ground state [13]. However, a transition to the excited state provides experimentalists exact signatures to exploit, since the excited daughter nucleus decays to the ground state via γ-ray emission. Provided isotopes with high Q values and detectors with low backgrounds are used, a $0\nu\beta\beta$-decay experiment to first 0_1^+ excited state can thus be conducted.

An excellent $0\nu\beta\beta$-decay candidate isotope is ^{130}Te with a 34.08% natural abundance, which makes the cost of enrichment viable, and a high Q-value of 2527.52 keV [63]. The latest value of the $0\nu\beta\beta$-decay of ^{130}Te to the first 0_1^+ excited state of ^{130}Xe was measured in 2012 with the CUORICINO detector as $\tau_{1/2} >$ 9.4 x 10^{23} years [4]. Both $0\nu\beta\beta$-decay and $2\nu\beta\beta$-decay are of second order weak interaction and are inherently slow. However, the phase space factor $G_{0\nu}(Q_{\beta\beta}, Z)$ scales as $\sim{Q_{\beta\beta}}^5$ for $0\nu\beta\beta$-decay versus $\sim{Q_{\beta\beta}}^{11}$ for $2\nu\beta\beta$-decay [7]. Furthermore, the ratio of $Q_{0\nu\beta\beta}[^{130}\mathrm{Te}_{gs}] \rightarrow Q_{0\nu\beta\beta}[^{130}\mathrm{Te}_{0_1^+}]$ is $\sim$ 34, (where "gs" stands for ground state), while $Q_{2\nu\beta\beta}[^{130}\mathrm{Te}_{gs}] \rightarrow Q_{2\nu\beta\beta}[^{130}\mathrm{Te}_{0_1^+}]$ is $>$ 2000 [72]. Searching for the $\beta\beta$-decay of ^{130}Te to the first 0_1^+ excited state of ^{130}Xe in the 0ν mode would therefore have a much larger detection efficiency and observation probability.

As ^{130}Te $0\nu\beta\beta$-decays to the first 0_1^+ excited state of ^{130}Xe (refer to Equation 17), the two emitted electrons peak at 735.3 keV:

$$^{130}\mathrm{Te} \rightarrow {}^{130}\mathrm{Xe} + 2\mathrm{e}^-, \tag{17}$$

which leaves the remaining 1793.50 keV to be emitted in one of three distinct γ-ray cascades as ^{130}Xe decays to the ground state (refer to Figure 4.10). Detecting the signature of interest therefore entails searching for the 1257 keV

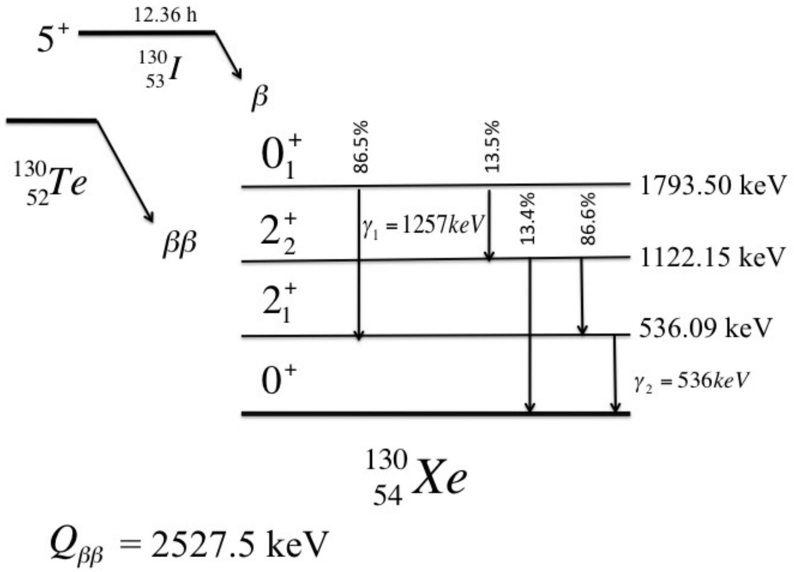

FIGURE 4.10. Decay scheme of ^{130}Te and relative γ-ray intensities

and 536 keV γ-rays either individually or as a coincidence signature, since their emission occurs with the highest probability (86.5%). In the $0^+ \to 2^+ \to 0^+$ γ-ray cascade, angular momentum conservation dictates a strong angular correlation between the two gammas which can be derived in terms of Legendre polynomials as seen in Figure 4.11.

4.3.2. Designing a Sensitive $0\nu\beta\beta$-decay Tellurium-130 Experiment.

In an ideal experiment designed to detect the $0\nu\beta\beta$-decay of ^{130}Te to the first 0^+_1 excited state of ^{130}Xe, a large sample mass should be used in order to account for the rarity of the decay and its associated long half-life. In the case of this particular experiment, it is important to understand the measurement efficiencies for having either a small diameter sample disk (matching the thin copper entrance window diameter) or a large diameter sample disk (matching the maximum diameter of the cryostats). In the latter case, adding large amounts of additional sample at large radii may only give a small increase in the measurement sensitivity due to the thicker copper cryostat walls and reduced solid

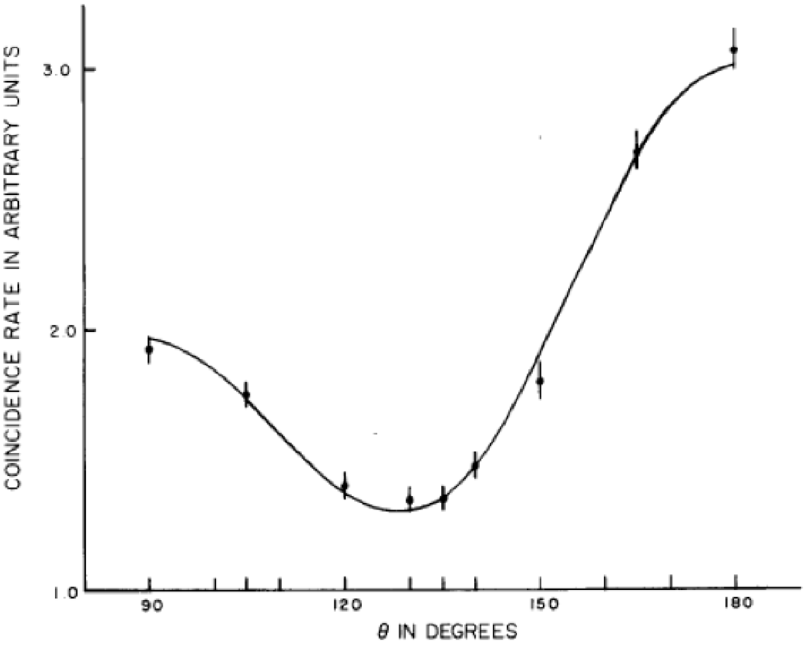

FIGURE 4.11. Angular correlation W(θ) = 1 + 0.356p_2(cosθ) + 1.14p_4(θ) between 1257 keV and 536 keV γ-rays [8]

angle for absorption of the gamma-rays emitted after decays at large sample-disk radii. To optimize the experiment, the geometrical configurations and their associated efficiencies yielding the highest sensitivity for the experiment (the longest half-life that could potentially be measured) need to be determined.

In order to determine the detector efficiency for a corresponding sample mass, simulations of the 536 keV and 1257 keV γ-ray cascade were performed. Two sets of simulations were run with a sample of ^{130}Te positioned in between the Cascades arrays of the GEANT4 model. The first set of simulations (Run 1) was performed for a ^{130}Te disk of diameter d = 14.5 cm, matching the diameter of the detectors thin copper entrance window. The thickness σ of the sample was varied from 1 cm to 5 cm (maximum vertical distance between the two arrays) to investigate self-attenuation effects. Figure 4.12 shows a ^{130}Te disk sample with d = 14.5 cm and σ = 5 cm positioned in between the two HPGe arrays. The second set of simulations (Run 2) was performed for a ^{130}Te disk of d = 29.5 cm, matching the outer diameter of the cryostat, while again varying

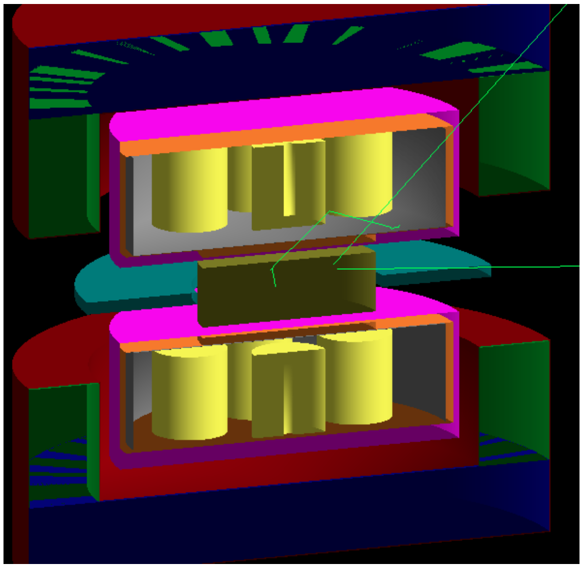

FIGURE 4.12. Three-dimensional view of a ^{130}Te sample placed between the 2 HPGe arrays

σ from 1 cm to 5 cm. The purpose of the second run was to investigate the possibility that sensitivity could be improved with a larger sample in spite of the thick copper of the cryostat attenuating the γ-rays. The strong angular correlation between the two emitted gammas ($0^+ \rightarrow 2^+ \rightarrow 0^+$) was taken into account in the simulations. Figure 4.13 shows the energy spectrum resulting from the simulation of a ^{130}Te disk with d = 14.5 cm and σ = 5 cm and the associated 536 keV and 1257 keV peaks with their 1793 keV sum peak. Simulated peak and coincidence efficiencies (ϵ) for Runs 1 and 2 for the signature of interest are calculated as seen in Tables 4.3 and 4.4 using the Total1 summing method. This summing method was selected as it yielded higher efficiencies, thus improving the sensitivity of the experiment.

The efficiency values of Tables 4.3 and 4.4 suggest the thick copper of the cryostat attenuates a significant portion of the γ-ray cascade. Tellurium-130 self-attenuation effects are also observed to play an important role in detector efficiency, since an inversely proportional relationship clearly exists between

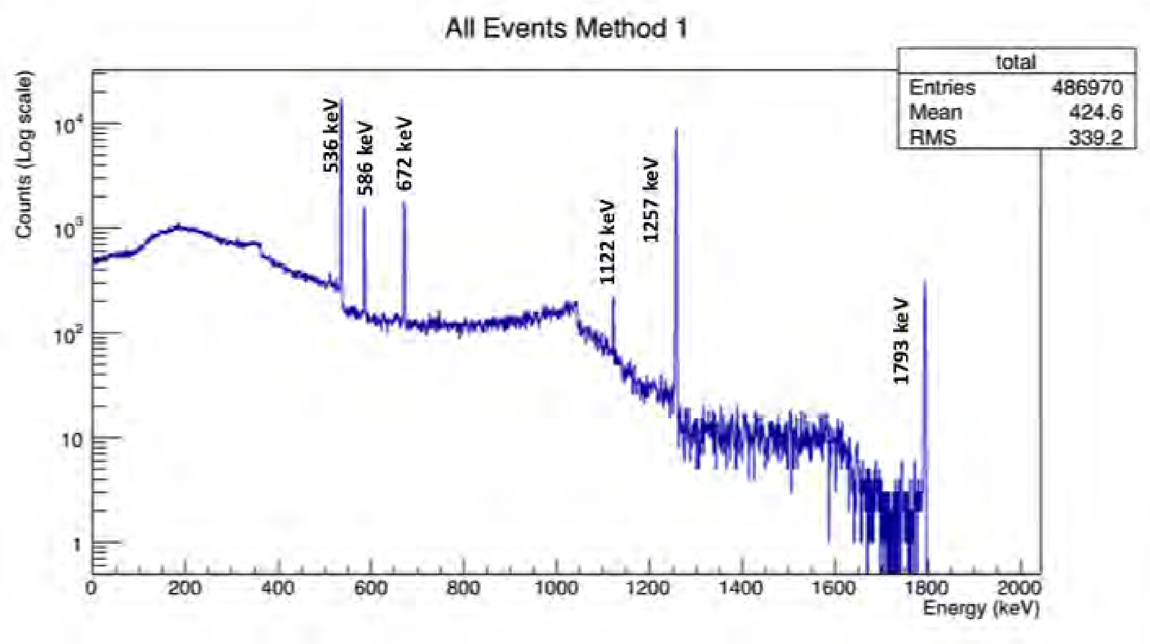

FIGURE 4.13. Simulated energy spectrum of the $0\nu\beta\beta$-decay of ^{130}Te to the first 0_1^+ excited state of ^{130}Xe with the 536 keV peak, 1257 keV peak and 1793 keV sum peak. The 586 keV, 672 keV and 1122 keV γ-rays from other much less probable cascades can also be seen.

the efficiencies and the sample's thickness. Error bars for the coincidence case are neglected due to their small values.

4.4. SUMMARY

Percent deviations between the experimental and simulated ^{137}Cs peak efficiencies range from 0.066% to 3.69% in Table 4.1. With these small deviations and errors, it can be stated that the GEANT4 model accurately portrays the performance of the Cascades detector. The simulations presented in this chapter are thus taken at face value. Further analysis, such as the calculation of the ^{238}U and ^{232}Th levels present in Cascades, along with predicting the sensitivity of an experiment measuring the $0\nu\beta\beta$-decay of ^{130}Te to the first 0_1^+ excited state of ^{130}Xe, will be presented in Chapter 5.

TABLE 4.3. Run 1 (d = 14.5 cm): simulated peak and coincidence efficiencies (ϵ) in Cascades for the $0\nu\beta\beta$-decay of ^{130}Te

σ (cm)	Peak Energy (keV)	Peak ϵ	Coincidence ϵ
1	536	0.0775±0.0002	0.0027
	1257	0.0345±0.0001	
2	536	0.0608±0.0002	0.0018
	1257	0.0289±0.0001	
3	536	0.0501±0.0002	0.0013
	1257	0.0258±0.0001	
4	536	0.0422±0.0002	0.0010
	1257	0.0231±0.0002	
5	536	0.0367±0.0002	0.0008
	1257	0.0211±0.0002	

TABLE 4.4. Run 2 (d = 29.5 cm): simulated peak and coincidence efficiencies (ϵ) in Cascades for the $0\nu\beta\beta$-decay of ^{130}Te

σ (cm)	Peak Energy (keV)	Peak ϵ	Coincidence ϵ
1	536	0.0422±0.0001	0.0009
	1257	0.0216±0.0001	
2	536	0.0329±0.0001	0.0006
	1257	0.0183±0.0001	
3	536	0.0263±0.0001	0.0004
	1257	0.0157±0.0001	
4	536	0.0219±0.0002	0.0003
	1257	0.0136±0.0001	
5	536	0.0186±0.0002	0.0002
	1257	0.0121±0.0001	

CHAPTER 5

ANALYSIS

5.1. PRIMORDIAL RADIATION ACTIVITY IN CASCADES

As seen in Chapters 1 and 2, investigating the efficiency of the copper electroforming technique to reduce natural levels of ^{238}U and ^{232}Th is one of the motivations behind this dissertation. Simulations of these chains were discussed in Chapter 4 to predict levels of primordial radioactivity in the copper cryostat of an experiment named Cascades: an ultra-low background HPGe array constructed at PNNL, consisting of 14 HPGe crystals housed in two cryostats made of copper electroformed with the same process that will be used in MAJORANA [48]. In this section, simulations of primordial radiation are compared to actual background data from Cascades. These comparisons, along with ICPMS assays of PNNL-electroformed copper, will help determine what the primary sources of primordial radiation are in the Cascades detector. Since the radon enclosure of Cascades was incomplete at the time of background collection, focus was shifted on placing upper limits as opposed to precise values on the levels of ^{238}U and ^{232}Th present.

5.1.1. Calibration and Background spectra. A background run lasting 16.59 days (with 98.28% live time) was measured with both arrays of Cascades. In order to calibrate the background, a calibration spectrum was produced using a filter paper sample containing a variety of radioactive sources, as seen in Figure 5.1. Highlighted features include a ^{241}Am x-ray peak at 59.3 keV, a ^{109}Cd peak at 88.14 keV, a ^{57}Co peak at 122.06 keV, standard 661.66

keV, 1173.23 keV and 1332.51 keV peaks from ^{137}Cs and ^{60}Co, and a number of backscatter, single-escape and double-escape peaks. Keeping in mind that

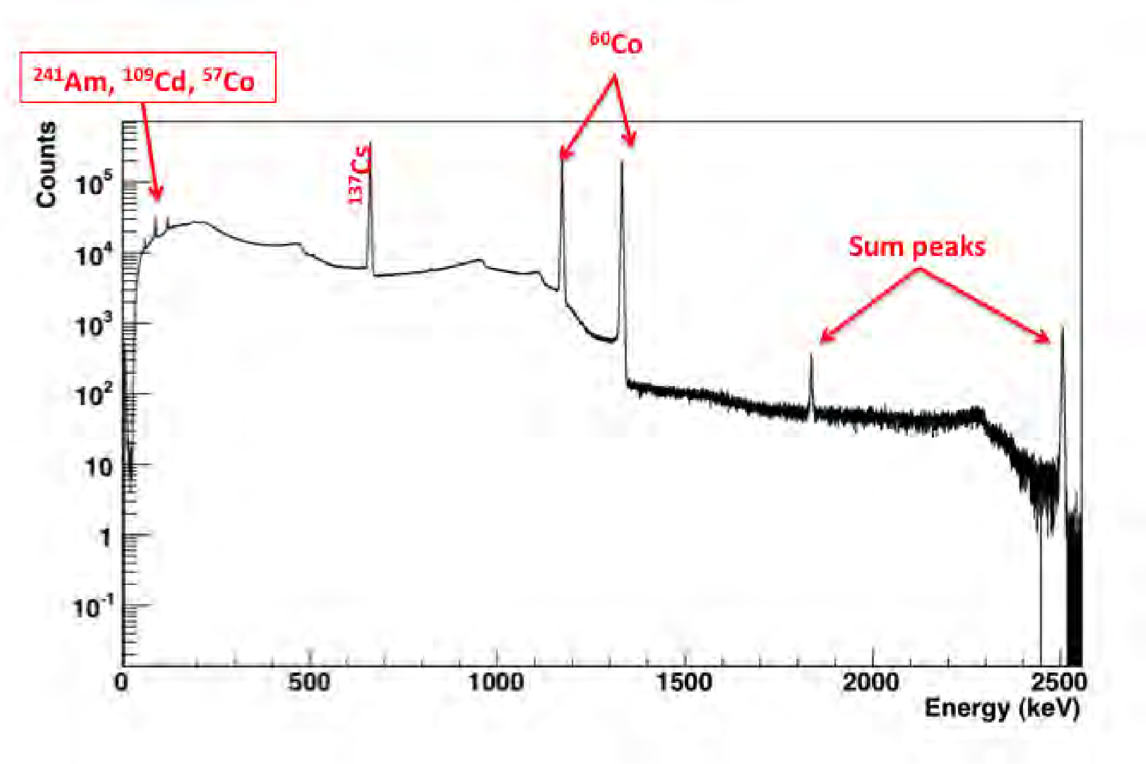

FIGURE 5.1. Features of calibration spectrum with prominent ^{137}Cs and ^{60}Co peaks

Crystal 10 was not functional at the time of background collection, the remaining 13 crystals in the two HPGe arrays were calibrated. Energy calibration curves were fitted with the standard polynomial equation ($ax^2 + bx + c$) in order to extract calibration coefficients (a, b, c) for each crystal (refer to Figure 5.2). The same coefficients were then used to calibrate the crystals individually in the background spectrum. Finally, the spectra of these calibrated crystals were summed together. Since the gammas of interest listed in Table 4.2 of Chapter 4 (emitted γ-rays from ^{228}Ac, ^{208}Tl and ^{214}Bi) are all emitted in coincidence for each isotope, the Total1 summing method was used as it allows for a better

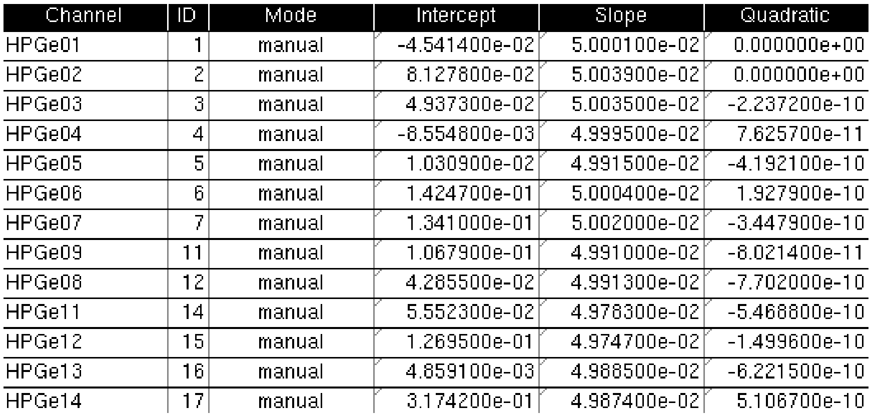

Channel	ID	Mode	Intercept	Slope	Quadratic
HPGe01	1	manual	-4.541400e-02	5.000100e-02	0.000000e+00
HPGe02	2	manual	8.127800e-02	5.003900e-02	0.000000e+00
HPGe03	3	manual	4.937300e-02	5.003500e-02	-2.237200e-10
HPGe04	4	manual	-8.554800e-03	4.999500e-02	7.625700e-11
HPGe05	5	manual	1.030900e-02	4.991500e-02	-4.192100e-10
HPGe06	6	manual	1.424700e-01	5.000400e-02	1.927900e-10
HPGe07	7	manual	1.341000e-01	5.002000e-02	-3.447900e-10
HPGe09	11	manual	1.067900e-01	4.991000e-02	-8.021400e-11
HPGe08	12	manual	4.285500e-02	4.991300e-02	-7.702000e-10
HPGe11	14	manual	5.552300e-02	4.978300e-02	-5.468800e-10
HPGe12	15	manual	1.269500e-01	4.974700e-02	-1.499600e-10
HPGe13	16	manual	4.859100e-03	4.968500e-02	-6.221500e-10
HPGe14	17	manual	3.174200e-01	4.987400e-02	5.106700e-10

FIGURE 5.2. Calibration coefficients for Crystals 1 - 14, with the exclusion of Crystal 10

reconstruction of coincidence events as discussed in Chapter 4. The final background spectrum can be observed in Figure 5.3 with annotated features of both cosmic and primordial origin.

The goals of the MAJORANA experiment are to reach a contaminant level in copper of 0.4 μBq/kg in ^{214}Bi and 0.1 μBq/kg in ^{208}Tl (the source of a problematic 2615 keV γ-ray line), which would correspond to an activity of 0.3 μBq/kg in ^{232}Th [69]. This said, the best ICPMS assay of copper electroformed at PNNL is at 0.6 μBq/kg in ^{232}Th and 1.3 μBq/kg in ^{238}U at this writing, as mentioned in Chapter 2. At first glance, however, the numerous background peaks of Figure 5.3 are of high concern and suggest the Cascades detector is not operating at an ultra-low background level. Due to the high intensity of the ^{228}Ac, ^{208}Tl and ^{214}Bi peaks, this direct counting method might not allow for a proper screening of the primordial activity in copper, since the levels of impurity appear to be coming from other small parts.

5.1.2. Activity Analysis. The background spectrum for each cryostat was first analyzed separately. It was noted the two cryostats had very different energy resolutions; this can be observed in Figure 5.4, where a 1171 keV peak

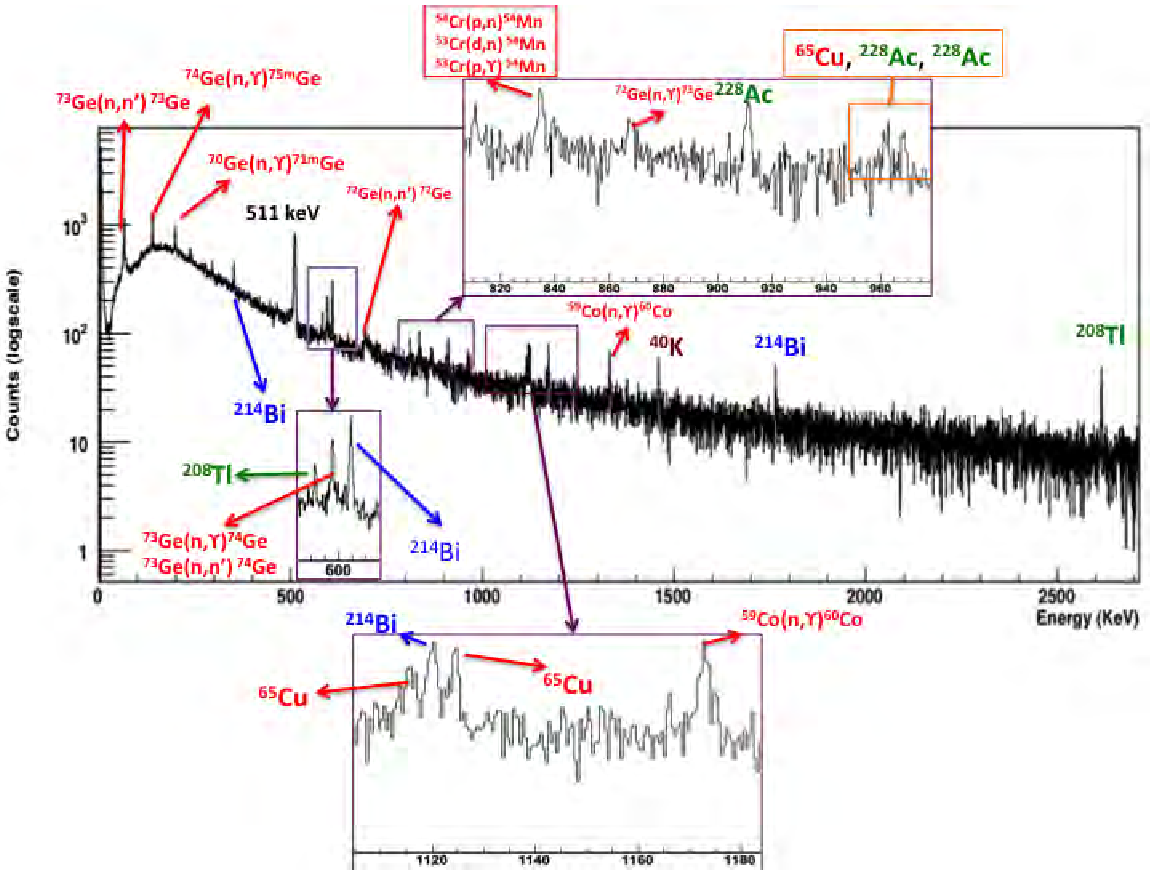

FIGURE 5.3. Background features observed in a 16.59-day background run measured with the two arrays of Cascades

is recorded separately with the upper array (blue spectrum) and the lower array (red spectrum). Since both cryostats were constructed and electroformed separately, summing the spectra of both arrays together would only result in averaging out levels of primordial radioactivity in the two cryostats. Attention was hence shifted to analyzing spectra separately from the upper and lower cryostats.

Using the parameters of Figure 5.5, peak searches were conducted with the Melusine software. Additionally, since the radon enclosure of Cascades remains incomplete at this writing, it was deemed important to calculate levels of ^{232}Th and ^{238}U choosing isotopes in the decay chains falling both before and

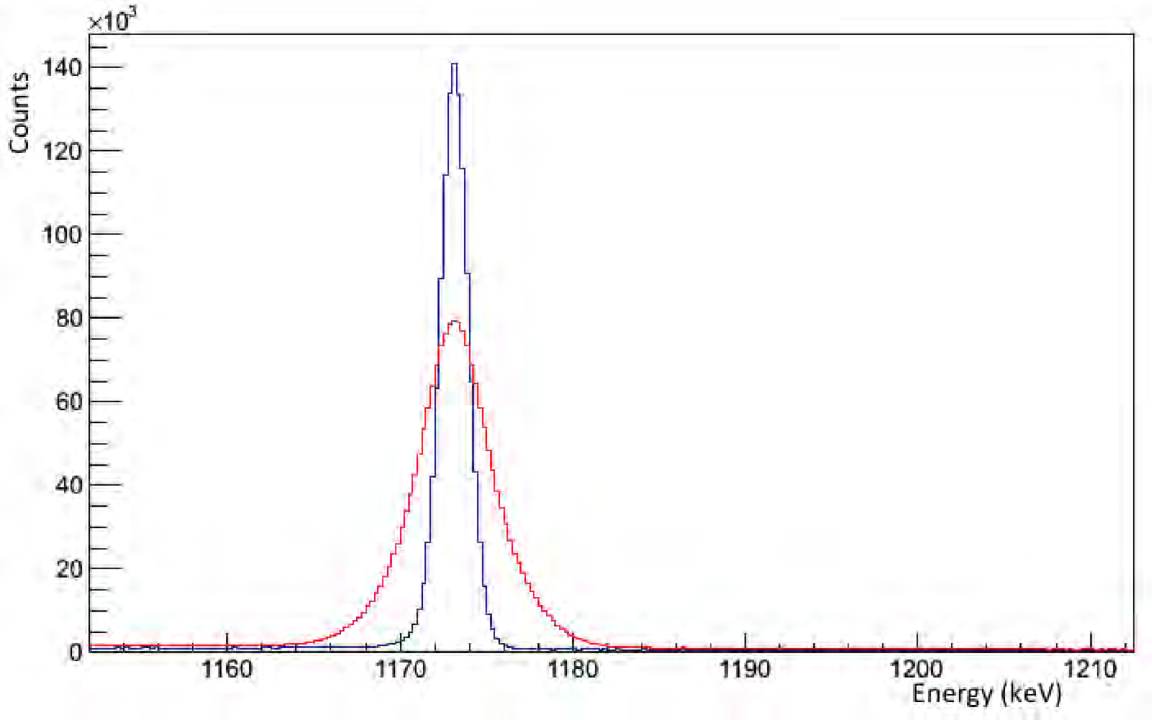

FIGURE 5.4. Difference in resolution of the two HPGE arrays of Cascades, with blue and red respectively representing the upper and lower cryostats

after the production of radon daughters ^{220,222}Rn, if statistics allowed for such analysis.

5.1.2.1. *Upper Array.* As mentioned earlier, Crystal 10 in the upper cryostat was not operational. A crystal-by-crystal examination revealed Crystal 14 had particularly poor energy resolution compared to the rest of the array. This crystal was therefore ignored in the analysis of the upper cryostat. To fit ^{232}Th peaks to the background spectrum, the following daughters were picked for the analysis: the isotope ^{228}Ac, with peaks of 911.21 keV (26.6% relative probability) and 968.97 keV (16.2%), which falls before the production of ^{220}Rn in the ^{232}Th decay chain, and the isotope ^{208}Tl, with peaks of 583.19 keV (44.8%) and 2614.5 keV (99%), which are produced post-radon from ^{212}Bi. These peaks are fitted with the Melusine software in Figures 5.6 - 5.9 using an optimal ROI window of 1.2 FWHM [24]. The optimum window ensures the background is

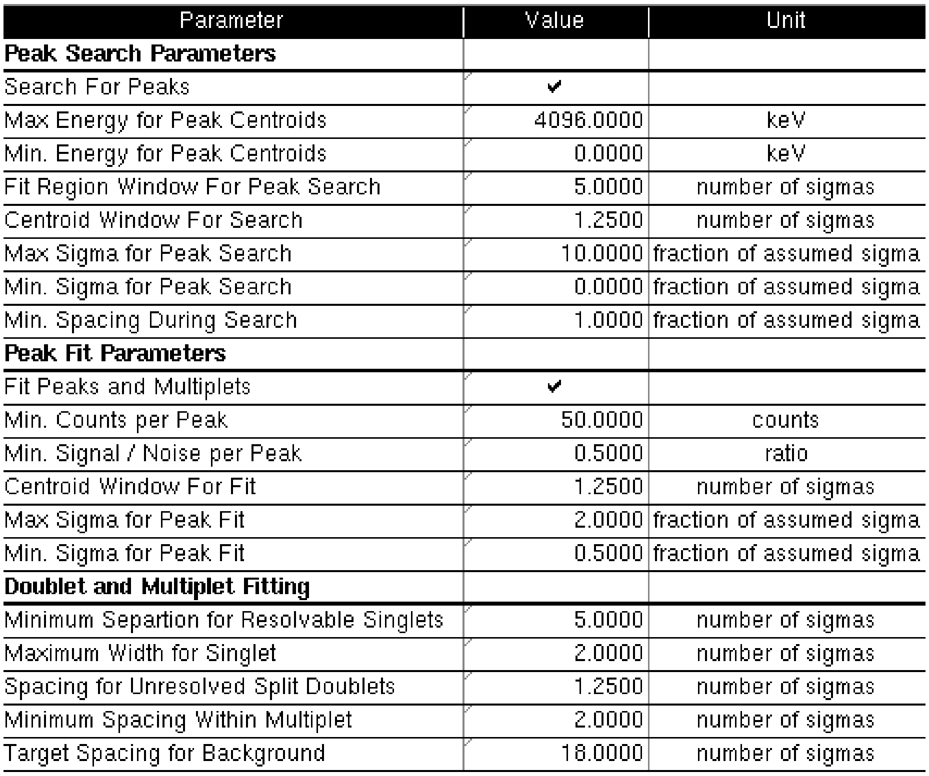

Parameter	Value	Unit
Peak Search Parameters		
Search For Peaks	✓	
Max Energy for Peak Centroids	4096.0000	keV
Min. Energy for Peak Centroids	0.0000	keV
Fit Region Window For Peak Search	5.0000	number of sigmas
Centroid Window For Search	1.2500	number of sigmas
Max Sigma for Peak Search	10.0000	fraction of assumed sigma
Min. Sigma for Peak Search	0.0000	fraction of assumed sigma
Min. Spacing During Search	1.0000	fraction of assumed sigma
Peak Fit Parameters		
Fit Peaks and Multiplets	✓	
Min. Counts per Peak	50.0000	counts
Min. Signal / Noise per Peak	0.5000	ratio
Centroid Window For Fit	1.2500	number of sigmas
Max Sigma for Peak Fit	2.0000	fraction of assumed sigma
Min. Sigma for Peak Fit	0.5000	fraction of assumed sigma
Doublet and Multiplet Fitting		
Minimum Separtion for Resolvable Singlets	5.0000	number of sigmas
Maximum Width for Singlet	2.0000	number of sigmas
Spacing for Unresolved Split Doublets	1.2500	number of sigmas
Minimum Spacing Within Multiplet	2.0000	number of sigmas
Target Spacing for Background	18.0000	number of sigmas

FIGURE 5.5. Parameters for peak searches in background spectra

still recognized with a wide-enough energy range, while making sure the significance of the background is not reduced by selecting an energy window that is too large. As Figure 5.7 reveals, the 969 keV energy peak has too much in-

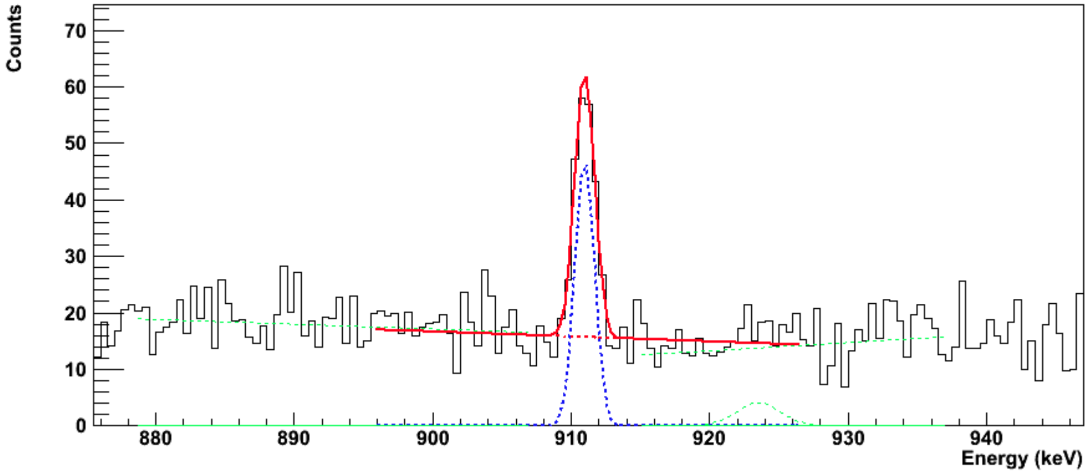

FIGURE 5.6. 911 keV peak from ^{228}Ac in the upper cryostat

terference from its neighboring 965 keV peak (also a γ-ray emitted from ^{228}Ac)

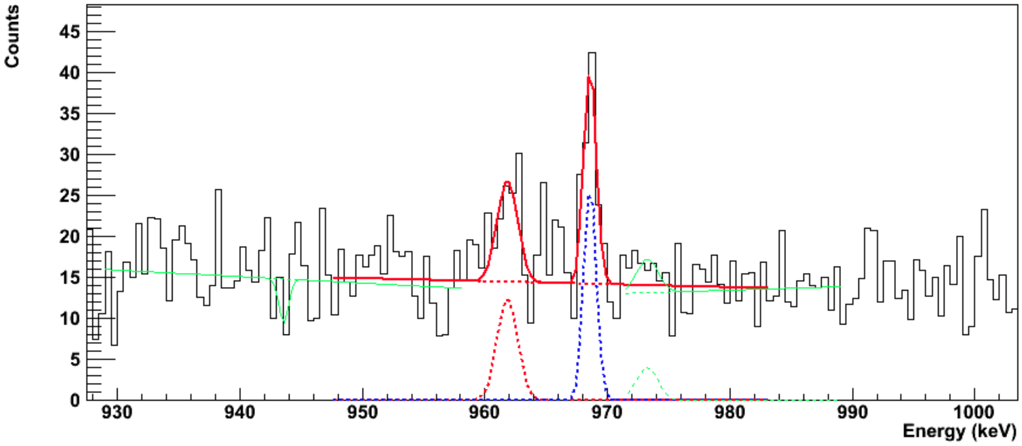

FIGURE 5.7. 969 keV peak from ^{228}Ac with the interference of a 965 keV peak in the upper cryostat

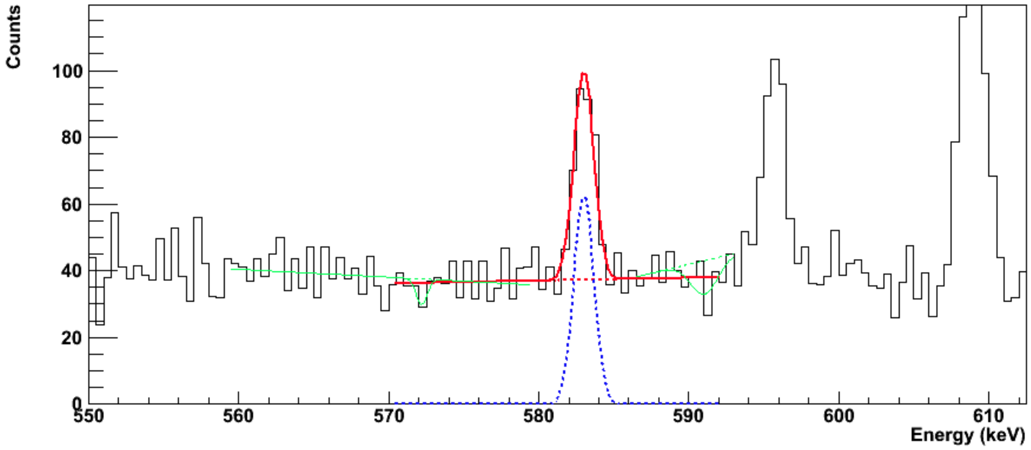

FIGURE 5.8. 583 keV peak from ^{208}Tl in the upper cryostat

and is fitted as a doublet with the Melusine software. Although the peaks both have good statistics, their interference with one another would not allow for an accurate background estimate to be made. Therefore, neither peaks are suitable candidates for the calculation of ^{228}Ac levels in the electroformed copper.

To fit ^{238}U peaks to the background spectrum of the upper array, many lower energy peaks were examined to find a suitable pre-radon isotope for the analysis of ^{238}U levels in the copper. The 63.29 keV peak from ^{234}Th (4.8%) and 186.10 keV peak from ^{226}Ra (3.50%) were selected and are fitted with the

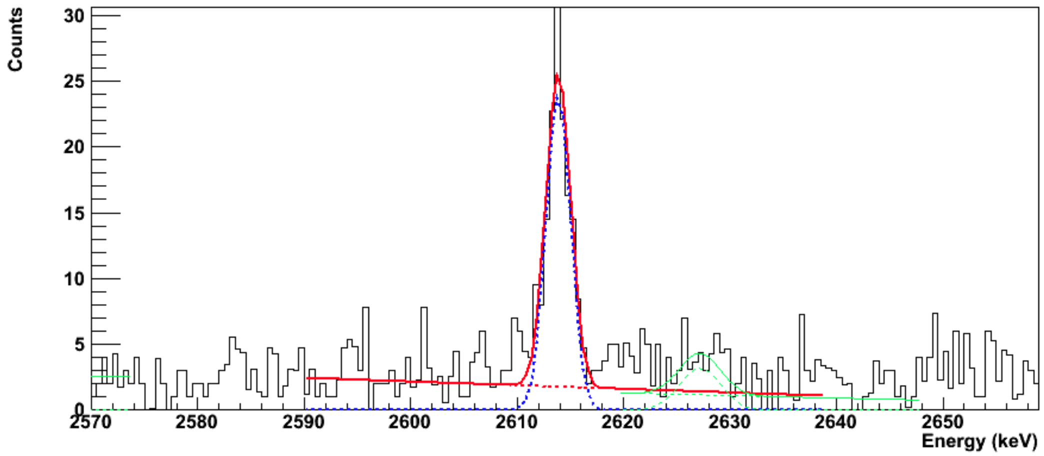

FIGURE 5.9. 2615 keV peak from ^{208}Tl in the upper cryostat

Melusine software in Figures 5.10 and 5.11. The 63 keV peak of Figure 5.10 is not deemed suitable for analysis, since it is completely dominated by the production of ^{73m}Ge at 66.7 keV [^{72}Ge(n, γ)^{73m}Ge], which results from thermalized neutrons (of cosmic origin) interacting with the germanium of the detector. As for the 186.10 keV peak, it has a rather low S/N ratio but an attempt to extract a level of ^{238}U in the copper from this fit will still be made in the upcoming analysis.

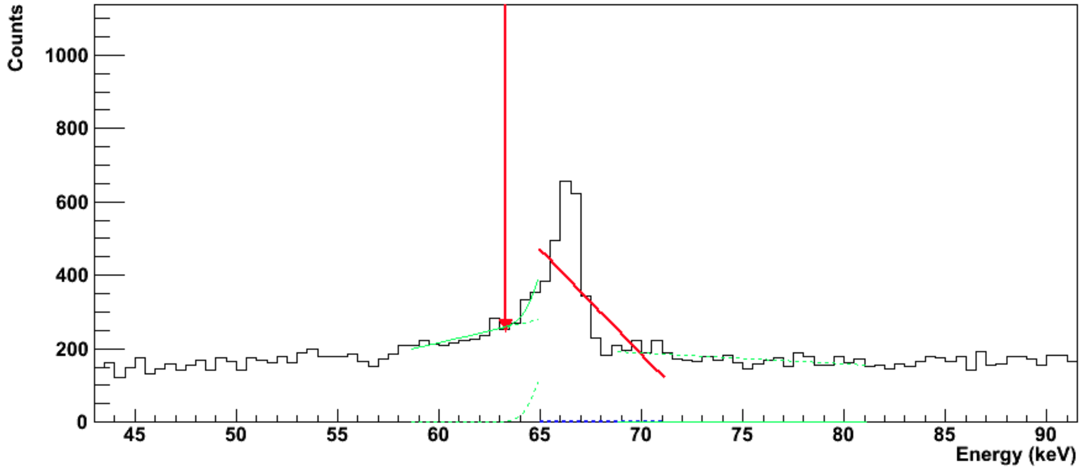

FIGURE 5.10. 63 keV peak from ^{234}Th with the interference of the production of ^{73m}Ge in the upper cryostat

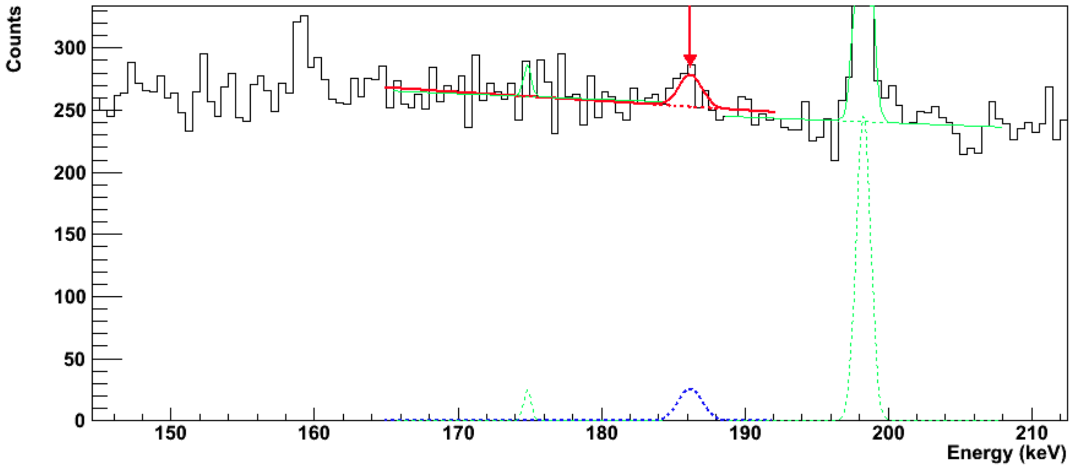

FIGURE 5.11. 186 keV peak from ^{226}Ra in the upper cryostat

The production of ^{222}Rn feeds into ^{214}Bi, from which the 609.3 keV (with 44.8% relative probability), 1120.3 keV (14.80%), and 1764.5 keV (15.36%) γ-rays were selected for the analysis (see Figures 5.12, 5.13, and 5.14). Due to the interference of ^{65}Cu production seen with γ-rays of energies 1115.5 keV and 1124.51 keV in Figure 5.13, a background estimate for the 1120 keV energy peak would not be reliable as for the other peaks, so it is disregarded from the analysis of the ^{214}Bi levels in the copper.

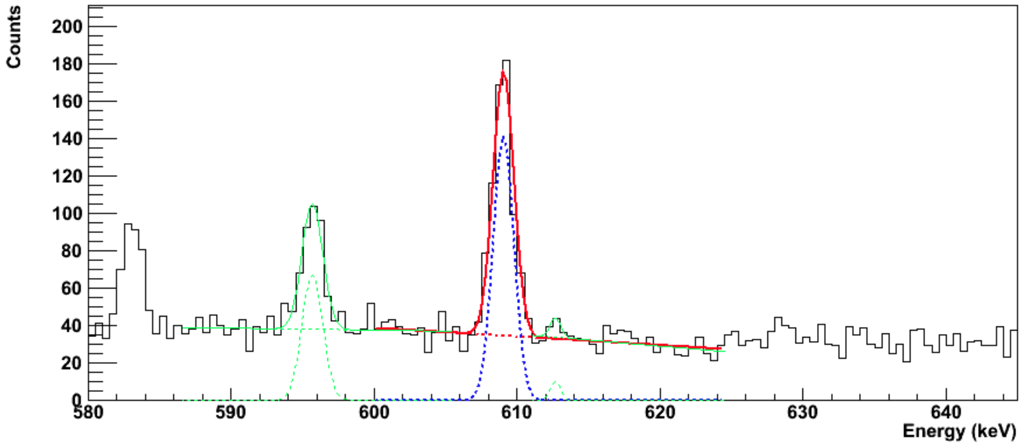

FIGURE 5.12. 609 keV peak from ^{214}Bi in the upper cryostat

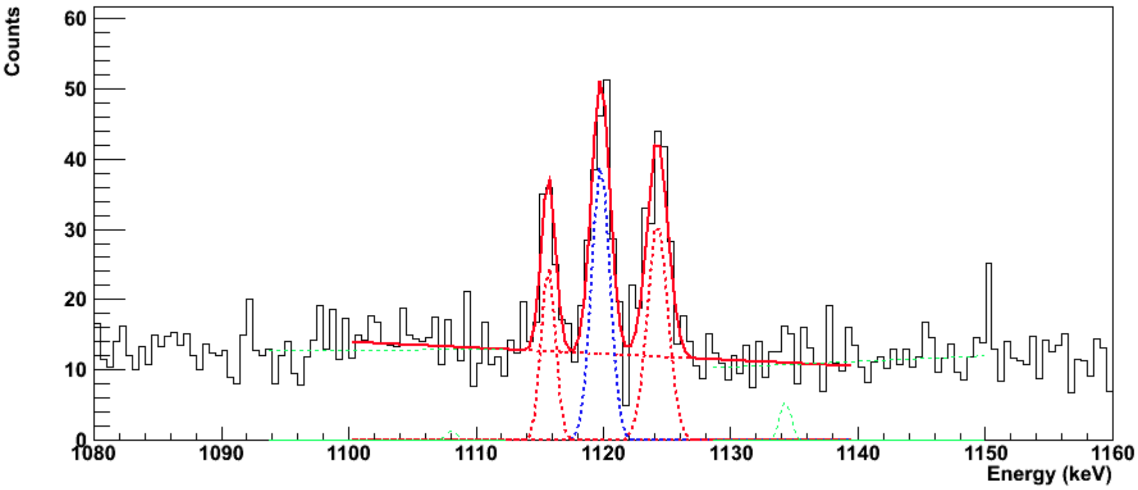

FIGURE 5.13. 1120 keV peak from ^{214}Bi with the interference of ^{65}Cu production in the upper cryostat

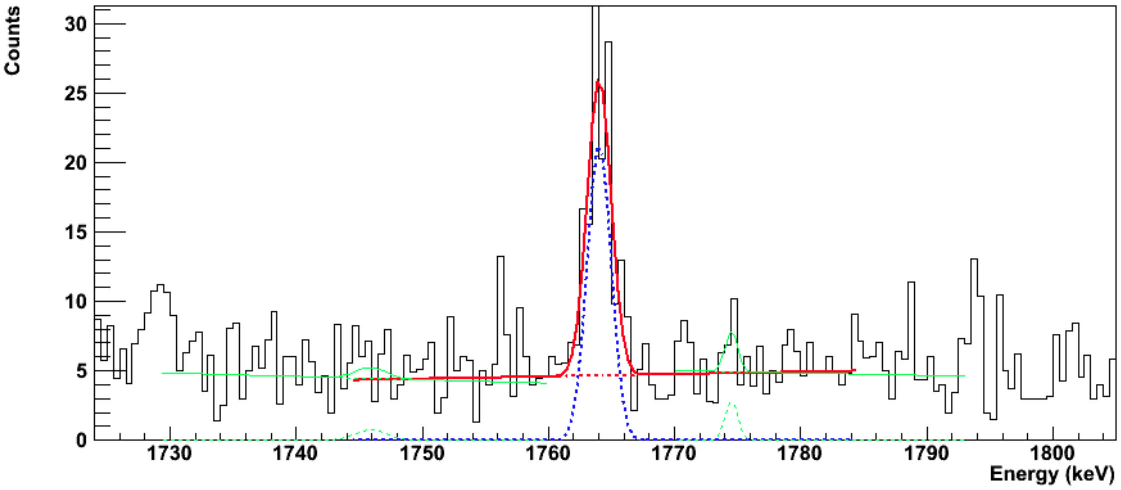

FIGURE 5.14. 1765 keV energy peak from ^{214}Bi in the upper cryostat

For each accepted peak discussed above, signal counts were extracted with algorithm-based background subtractions generated by the Melusine software. Efficiencies based on simulations presented in Chapter 4 were calculated, taking into account which crystals were being used for the analysis. Using the simulated efficiency and the intensity of the γ-ray, a number of decays was calculated as follows:

$$\text{Decays} = \frac{Signal\ counts}{\epsilon \times I}\ , \tag{18}$$

where ϵ is the simulated efficiency of the peak and I is its intensity (relative probability of being emitted). Knowing the total time t of the background run in seconds, the total mass M of the cryostat in kilograms, the activity A of an isotope can then be obtained in mBq/kg:

$$\mathrm{A} = \frac{\frac{Decays}{t} \times 10^3}{M} \ . \tag{19}$$

Final activity results in the upper cryostat are presented in Table 5.1. An in-depth discussion of these results will follow the analysis of the lower array of Cascades.

TABLE 5.1. Activity (Act.) and upper limits (Act.+) levels of ^{232}Th and ^{238}U present in the electroformed copper of the upper cryostat

Daughter nucleus	Energy (keV)	S/N ratio	Simulated efficiency	Act. (mBq/kg)	Act.+ (mBq/kg)
^{228}Ac	911	3.55	0.00801 ± 0.00010	4.26	4.60
^{208}Tl	583	2.02	0.00968 ± 0.00008	1.40	1.50
^{208}Tl	2615	16.0	0.00322 ± 0.00009	2.37	2.58
^{226}Ra	186	0.120	0.02870 ± 0.00016	5.64	6.19
^{214}Bi	609	4.90	0.01093 ± 0.00010	5.72	5.98
^{214}Bi	1765	5.53	0.00550 ± 0.00009	6.48	7.14

5.1.2.2. *Lower Array*. All seven crystals in the lower array were functional, however, as mentioned earlier, the lower cryostat had much poorer resolution than the detector's upper array. The same energy peaks were examined and fitted, with the exclusion of the ^{234}Th 63 keV γ-ray and ^{214}Bi 969 keV and 1120 keV γ-rays, which presented the same problems as discussed previously. The same optimum window of 1.2 FWHM was used. Tweaking the peak search parameters of Figure 5.5 did not amount to any significant change, as many of these peaks had to be fitted manually due to the poor energy resolution. The other peaks can be observed in Figures 5.15 - 5.20. Both the 583 keV and 186 keV peaks of Figures 5.16 and 5.18 are buried in background and result

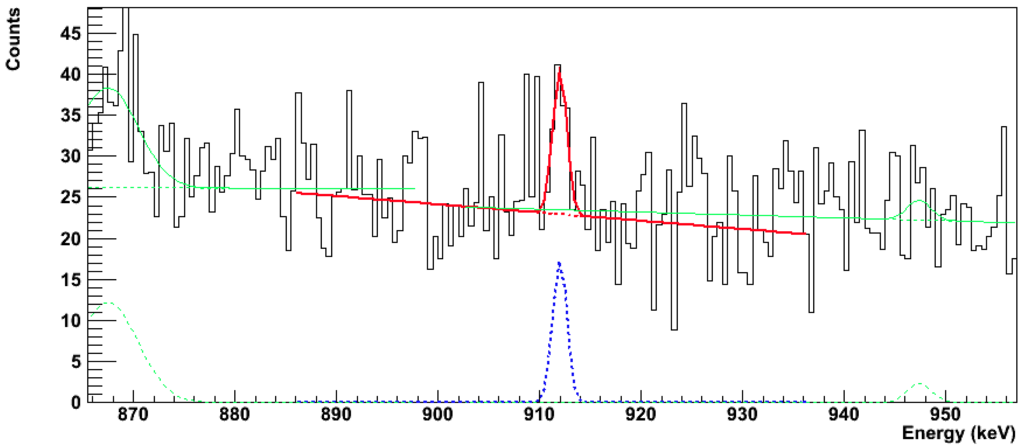

FIGURE 5.15. 911 keV peak from ^{228}Ac in the lower cryostat

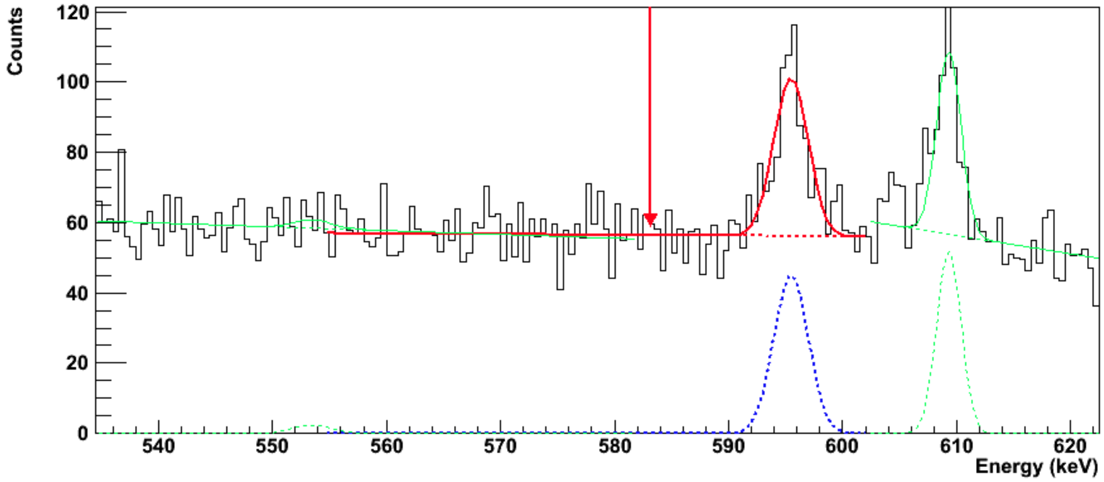

FIGURE 5.16. 583 keV peak from ^{208}Tl in the lower cryostat buried in background

in a null signal count. Signal counts were extracted from the remaining peaks using the Melusine software, and activities were calculated using Equations 18 and 19, again with simulated efficiencies corresponding to the array. Final activity results in the lower cryostat are presented in Table 5.1.

5.1.3. Discussion of Activity Results. The results of Tables 5.1 and 5.2 are about three orders of magnitude higher than the expected μBq/kg levels

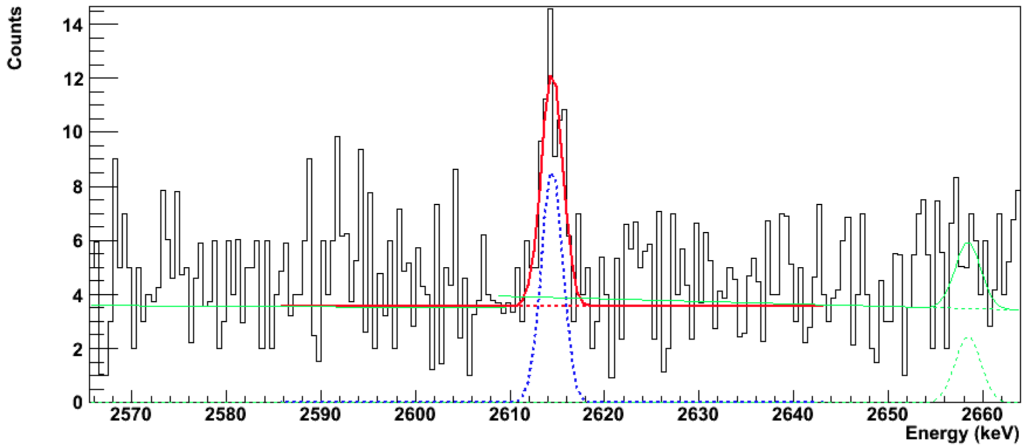

FIGURE 5.17. 2615 keV peak from ^{208}Tl in the lower cryostat

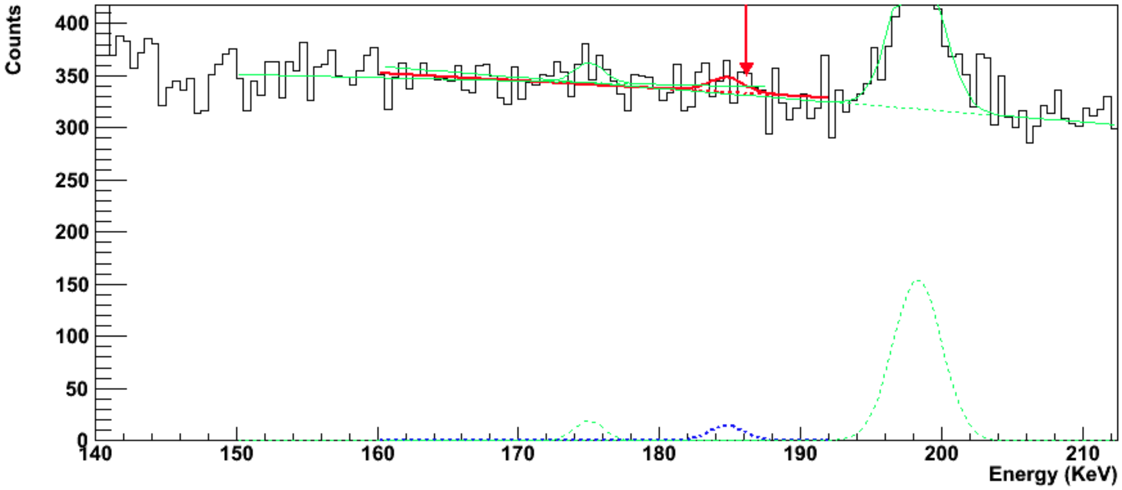

FIGURE 5.18. 186 keV peak from ^{226}Ra in the lower cryostat buried in background

TABLE 5.2. Activity (Act.) and upper limits (Act.+) levels of ^{232}Th and ^{238}U present in the electroformed copper of the lower cryostat

Daughter nucleus	Energy (keV)	S/N ratio	Simulated efficiency	Act. (mBq/kg)	Act. + (mBq/kg)
^{228}Ac	911	0.90	0.00769 ± 0.00008	1.63	1.84
^{208}Tl	2615	2.90	0.00320 ± 0.00007	0.85	0.97
^{214}Bi	609	1.09	0.01051 ± 0.00008	3.20	3.39
^{214}Bi	1765	1.79	0.00533 ± 0.00008	5.37	5.97

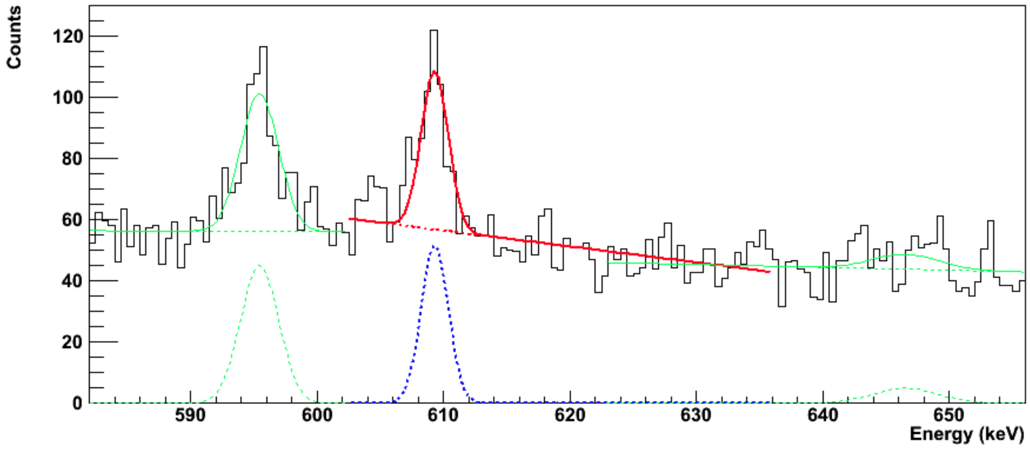

FIGURE 5.19. 609 keV peak from ^{214}Bi in the lower cryostat

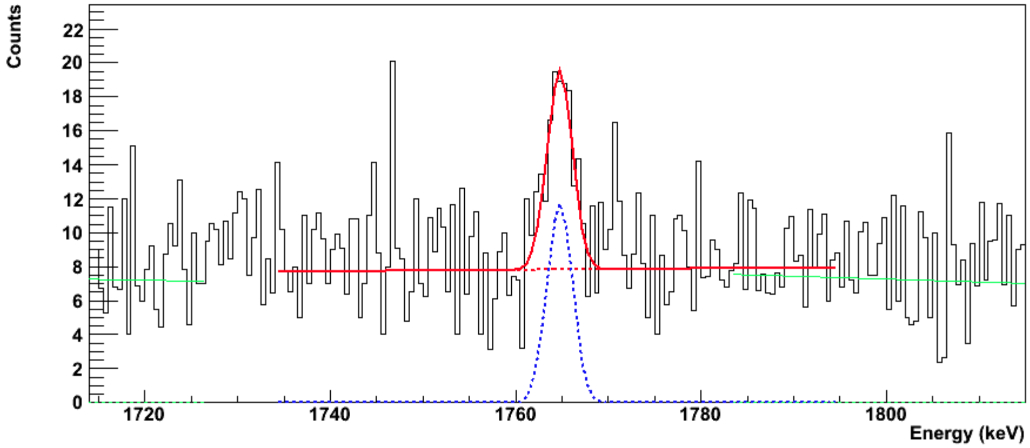

FIGURE 5.20. 1765 keV energy peak from ^{214}Bi in the lower cryostat

of ^{232}Th and ^{238}U in the electroformed copper. The analysis shows the backgrounds in Cascades are unlikely coming from the electroformed copper components. This assumption is based upon the knowledge that commercially available Oxygen-Free High Conductivity (OFHC) copper has ^{232}Th and ^{238}U content much lower than the concentrations resulting from the analysis. Additionally, as stated previously, assay of PNNL copper shows values of <0.6 μBq/kg for ^{232}Th and <1.3 μBq/kg for ^{238}U. The origin of the backgrounds is likely to be in the plastics and other small parts of the cryostat, such as LFEPs, LFEP sockets, wiring, wiring feedthroughs in the coldplate, copper rods of the crystal mounts, etc. A definitive statement about the origin of the background cannot be made because the majority of these small parts were not screened to the necessary level of radiopurity, since the screenings were performed above ground on commercial non-low background counters.

Although the copper for the Cascades detector was not electroformed in a MAJORANA-like clean-room environment, this is very unlikely the primary cause of such large activity levels of primordial contamination in the cryostat of Cascades. Rather, as suggested above, these high levels indicate that parts other than the copper of the cryostat are contaminated by ^{232}Th and ^{238}U. Furthermore, these small parts are not identical for each cryostat. For instance, different plastic was used for the crystal mounts of the upper and lower arrays (UHMW HPDE versus PCTFE respectively). Additionally, six of the seven crystals of the upper array were supplied by a different manufacturer and could have different levels of primordial radiation. This would perhaps explain the difference in activities of the two cryostats. Although they were electroformed separately, the electroforming procedure remained the same and the activity numbers would not be expected to differ by so much. Even more importantly, these small parts are positioned very close to the crystals. It is possible activity levels to the order of μBq/kg were reached, but that these close positions are resulting in very high efficiencies for the emitted gammas of isotopes ^{228}Ac, ^{208}Tl and ^{214}Bi, which would result in high activity numbers. These small parts are different for the lower and upper cryostats and also help explain the inconsistencies in the activities of the copper. There were also some last-minute additions to the detector, such as lining the inner lead shield with OFHC copper to absorb bremsstrahlung x-rays, that could be contributing to the background.

It is important to note the upper activity limits in Tables 5.1 and 5.2 were obtained taking into account statistical uncertainties only; this also helps explain the larger-than-error-bars discrepancies between some of the upper activity limits determined by analyzing γ-rays of the same isotope, which should have approximately the same activity value. If systematic errors were included, upper activity limits would be much larger. Sources of systematic errors in the Cascades detector could include, amongst others, uncertainty on the signal efficiency, the energy scale, the data acquisition system, the cosmic muon veto system and the simulations. Simulations were performed as a close approximation only and with an idealized geometry. Crystals were constructed identically to one another in the GEANT4 model, when in fact their dimensions varied slightly (probably by $\sim$1 - 2 mm). Other details, such as the inner copper shield and the copper mounts of the crystal, were not coded in the model. Another source of systematic error lies in the Melusine software, especially when analyzing peaks of very small intensity. Tweaking the parameters sometimes resulted in large differences in peak counts and background estimates, and it became arbitrary as to which results were more accurate.

Table 5.1 shows numbers that are more or less consistent with one another. An initial level of ^{232}Th of 4.26±0.33 mBq/kg is calculated with the 911 keV energy peak of ^{228}Ac. As expected, this activity is reduced with the production of ^{212}Bi, 36% of which feeds into ^{208}Tl. With this branching ratio, we get a projected ^{208}Tl activity level of $<$1.53±0.12 mBq/kg (the lower limit is present because some nitrogen purging is taking place), assuming the activity of ^{228}Ac is correct. However, the analysis reveals two levels of ^{208}Tl that differ moderately from one another. The 585 keV peak carries a value of 1.40±0.10 mBq/kg with a S/N ratio of 2.02, while the 2615 keV peak measures at 2.37±0.21 mBq/kg with a 16.0 S/N ratio. These differences could be attributed to a number of uncertainties, such as the exclusion of systematic error analysis or poor fitting estimates from the Melusine software due to the high number of cosmic-generated peaks in the background. On the other hand, the levels of ^{238}U are more consistent with one another as expected, since they are calculated from isotopes that do not branch out; the upper activity limits vary from 5.98 mBq/kg to 7.14 mBq/kg.

Since the copper was electroformed separately, and the high activity numbers suggest there is a lot of primordial activity coming from small parts, we do not expect the activities of both cryostats to be the same. As expected there is a drop from the activity level of ^{228}Ac (1.63±0.21 mBq/kg) to ^{208}Tl (0.85 ±0.12 mBq/kg). Taking into account the 36% branching ratio, we expect a ^{208}Tl level of $<0.59\pm0.072$ mBq/kg with the purging of radon gas by nitrogen, which is a little higher than the calculated ^{208}Tl level. The ^{238}U upper limits also offer some discrepancy with 3.39 mBq/kg for the 609 keV energy peak and 5.97 mBq/kg for the 1765 keV energy peak. It is hard to gauge with such low S/N ratios which isotopes (^{228}Ac, ^{208}Tl or ^{214}Bi) offer more accurate results due to the poor energy resolution of the cryostat.

5.2. SENSITIVITY OF A $0\nu\beta\beta$-DECAY ^{130}TE EXPERIMENT

As seen in Chapter 1, an equation measuring the discovery potential or sensitivity of a next-generation $0\nu\beta\beta$-decay experiment can be derived by requiring that:

$$C_{\beta\beta} = n_\sigma\sqrt{B}\ , \tag{20}$$

where $C_{\beta\beta}$ is the number of $0\nu\beta\beta$-decay events, n_σ is the desired standard deviation of the measurement, and B is the number of background counts in the region of interest. In the case of a ^{130}Te experiment, the source does not play the part of the detector, so Equation 20 is derived to measure the sensitivity of this experiment such that [24]:

$$T^{0\nu}_{1/2}(n_\sigma) = \frac{4.16\times10^{26}y}{n_\sigma}\left(\frac{M\varepsilon a}{W}\right)\sqrt{\frac{t}{b\Delta E}}\,, \tag{21}$$

where ϵ is the event-detection efficiency, a is the isotopic abundance in the source material, W is the molecular weight of the source material (g/mol), M is the total mass of the source (kg), b is the background rate in counts (keV-y)$^{-1}$ of the detector, and ∆E is the spectral resolution of the experiment in keV. The factor 10^{26} results from Avogrado's number and from expressing the relation as a half-life (years).

In Equation 21, a confidence level of three sigma (n_σ = 3), a run time of 10 years, and a sample of ^{130}Te powder with density ρ= 5900 kg/m^3 and 90% enrichment were selected as parameters for the sensitivity calculation. Since the energy resolution of the lower array was so poor, the energy resolution curve from the upper cryostat was used to optimize the experiment (see Figure 5.21). Calculations revealed the detectors energy resolutions were 1.62 keV and 2.10

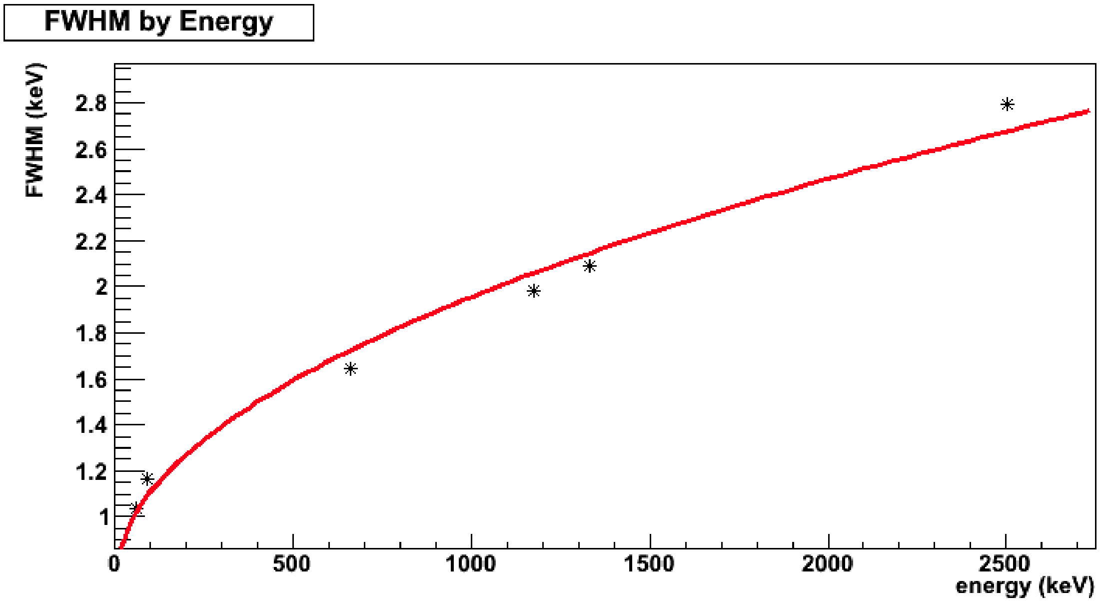

FIGURE 5.21. Resolution curve of upper cryostat

keV for the 536 keV and 1257 keV ROIs respectively. In order to calculate the optimum energy windows, an optimum ROI of 1.2 FWHM was once again assumed [24], which resulted in calculated optimum energy windows of 2.16 keV for the 536 keV ROI and 2.94 keV for the 1257 keV region of interest. To account for the fact the full peaks were not included in the ROIs, the detector efficiencies for ^{130}Te were reduced accordingly by a factor of 0.838 [24].

Background rates for the ROIs were determined by examining the peaks of interest in the 16.59-day background spectrum, as seen in Figures 5.22 and 5.23. This revealed background rates of approximately 5453 counts (keV-y)$^{-1}$ and 1467 counts (keV-y)$^{-1}$ for the 536 keV and 1257 keV ROIs respectively.

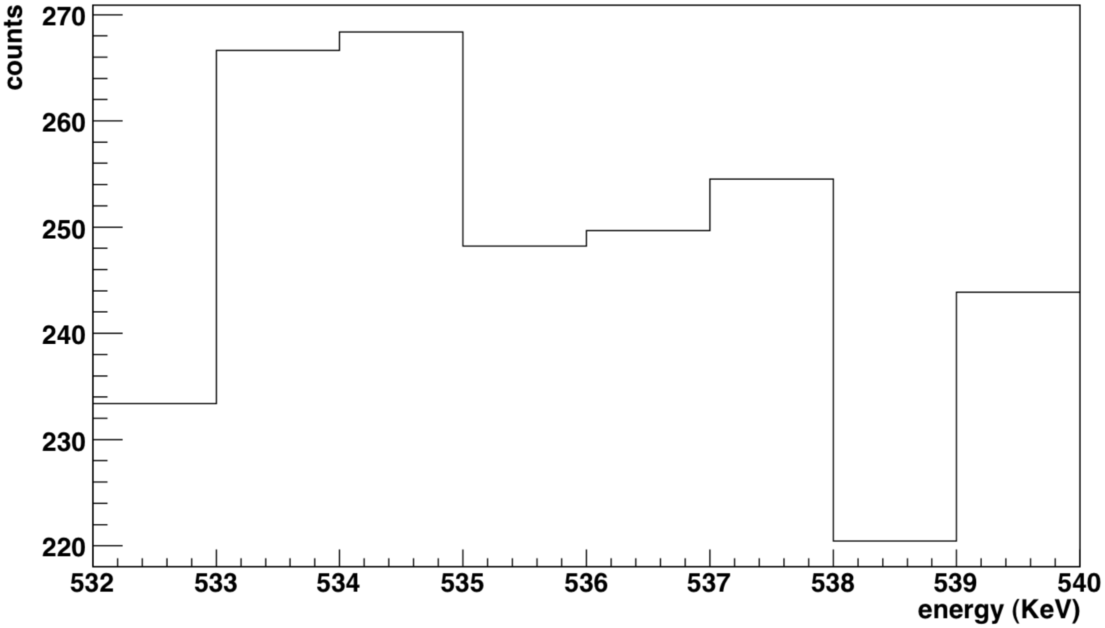

FIGURE 5.22. Background rate of a 16.59-day run in the 536 keV ROI

Predicting the sensitivity of the experiment in coincidence mode is more challenging since the current measurement of the background had a null result. It is possible that a longer background measurement would yield different results, but in this case, a 16.59-day background measurement resulted in no counts in the coincidence plane region of interest. If the number of observed events n_{obs} is zero, the standard confidence belt approach for upper confidence

FIGURE 5.23. Background rate of a 16.59-day run in the 1257 keV ROI

limits suggests fixing an upper 90% C.L. of 2.3 events for μ + b, where μ and b are the number of signal and background events [36]. Assuming that a total background of 2.3 counts would be detected in a 16.59-day experimental measurement, this results in a worse case for the coincidence background rate of 50.6 counts/yr. To obtain the best case scenario, a total background spectrum of 2.3 counts is presumed for the entire run of the experiment (t = 10 years), yielding a background rate of 0.23 counts/yr. The omission of the energy resolution term in Equation 21 and (keV)$^{-1}$ units in the background rates is justified by the rarity of these particular coincidence events. The worst-case and best-case sensitivity limits for an experiment designed to detect the 536 keV and 1257 gammas in coincidence can then be calculated.

With these numerous values, a range of half-life bounds ($\tau_{1/2}$) for the different parameters of the experiment searching for the 536 keV and 1257 keV gammas separately as well as in coincidence are obtained using Equation 21.

The parameters (diameter d and thickness σ of a ^{130}Te disk of associated mass M and detection efficiency ϵ) yielding the largest sensitivities are shown in Table 5.3.

TABLE 5.3. ^{130}Te disk parameters yielding the highest discovery potential searching for the 536 keV, 1257 keV and coincident γ-rays for a 10 yr-experiment

Experiment	σ(cm)	d(cm)	Mass (kg)	ϵ %	$\tau_{1/2}$ (yr)
536 keV peak	5	29.5	20.2	1.86	9.34×10^{21}
1257 keV peak	5	29.5	20.2	1.21	1.03×10^{22}
Coinc. (worse case)	3	29.5	12.1	0.041	1.80×10^{21}
Coinc. (best case)	3	29.5	12.1	0.041	2.68×10^{22}

In Table 5.3, the highest half-life value of the $0\nu\beta\beta$-decay of ^{130}Te to the first 0^+_1 excited state of ^{130}Xe is 2.68×10^{22} years. Hence the experiment that would reach the highest discovery potential should be designed by placing a 12.1-kg ^{130}Te powder sample of diameter d = 29.5 cm and thickness σ = 3 cm in between the HPGe arrays of Cascades and searching for the 536 keV and 1257 γ-rays in coincidence.

Tellurium-130 is ideal from the point of view that the $2\nu\beta\beta$-decay to the first 0^+_1 excited state of ^{130}Xe is very suppressed by the loss of phase space, although $0\nu\beta\beta$-decay is somewhat suppressed as well. A better isotope to use would be ^{100}Mo, since the $2\nu\beta\beta$-decay of ^{100}Mo is not suppressed and dominates over 0ν-decay. Furthermore, using ^{100}Mo in a bolometer coincidence experiment in which the electron energies are also recorded would allow to distinguish between 0ν and $2\nu\beta\beta$-decay processes.

5.3. SUMMARY

As seen in Tables 5.1 and 5.2, the measured activities in Cascades are higher than what could be expected for by the copper cryostats by three orders of magnitude. Although the copper was not electroformed in a clean room environment like MAJORANA, these high numbers indicate other small parts, such as plastic, wiring, LFEPs, copper mounts, etc. are contaminated by primordial activity at a higher than desirable level and are a main source of primordial background. This contamination is more efficiently detected by parts close to the crystal and appears to be skewing the activity results with a larger margin. Evidently, reducing the radioactivity of these small parts should be considered far more important than reducing the impurities present in the copper.

Due to the generalization of the Melusine software fitting and background subtraction estimates, larger than desired uncertainties are also most likely present in the peak areas used to calculate the activities. Additionally, the background spectrum of Figure 5.3 shows that despite the underground depth, active shielding and passive shielding of Cascades, there is still a large number of peaks resulting from the cosmic-ray activation of the copper and germanium present in the spectrum. These secondaries can reduce the S/N ratios of the energy peaks of interest and create more uncertainties in their fit. Building the detector as an idealized geometry in GEANT4, or not coding last-minute additions to the detector, such as copper lining in the lead shield, could also partially lie at the source of these discrepancies.

A 10-year experiment designed to measure the $0\nu\beta\beta$-decay of ^{130}Te to the first 0_1^+ excited state of ^{130}Xe with Cascades would allow half-lives to the order of 10^{22} to be probed, specifically $\tau_{1/2}$ = 2.68×10^{22} years at best. Running this experiment would therefore neither confirm nor improve the lower limit of $\tau_{1/2} > 9.4\times10^{23}$ years determined in 2012 [4]. It could, however, confirm the experimental $2\nu\beta\beta$-decay value of $\tau_{1/2} > 2.3\times10^{21}$ years determined in 2001 by low-background HPGe detectors [13]. In conclusion, the code developed in this dissertation can be applied to many other isotopes that can $\beta\beta$-decay to excited states of the daughters in both 0ν and 2ν modes.

CHAPTER 6

CONCLUSION

6.1. SUMMARY OF THESIS

One of the goals of this dissertation was investigating the efficiency of background mitigation techniques to reduce natural levels of ^{238}U and ^{232}Th in the MAJORANA experiment: an array of HPGe detectors isotopically enriched to 86% in ^{76}Ge with a total mass of hundreds of kilograms with goals of searching for the $0\nu\beta\beta$-decay of ^{76}Ge to ^{76}Se. This was attempted with Cascades, a HPGe array constructed at PNNL, consisting of 14 HPGe crystals housed in two cryostats made of copper electroformed with the same process that will be used in MAJORANA. Additionally, experimental applications of the Cascades detector were studied by predicting the sensitivity for a $\beta\beta$-experiment using as an example simulations of ^{130}Te, an even-even nucleus that can undergo $0\nu\beta\beta$-decay to the first 0_1^+ excited state of ^{130}Xe producing three possible γ-cascades as it transitions to the ground state. There are many other isotopes that could be measured with the method developed in this thesis.

In Chapter 1, the general properties of neutrinos and the motivations behind studying $\beta\beta$-decay were presented. The observation of parity violation, possible violation of lepton-number symmetry, the extreme mass differences between neutrinos and their charged leptons, the existence of exotic particles such as right-handed gauge bosons and of the Majoron, the absolute mass and nature of the neutrino, and what role the neutrino would play as a Majorana particle in the baryon assymmetry of the universe via leptogenesis are all important aspects of neutrino physics that could be probed with $\beta\beta$-decay experiments.

The success of a next-generation $0\nu\beta\beta$-decay experiment, such as MAJORANA, heavily depends on its capability to mitigate background caused by cosmogenic activity and primordial radiation present in all materials. Sources of background and techniques to increase the signal-to-noise ratios of events were presented in Chapter 2. Using ultra-pure materials through effective zone refinement and crystal growth methods, and electroforming copper to build the cryostat for Cascades, were discussed as necessary to reach low levels of ^{238}U and ^{232}Th in the background, two long-lived primordials that contaminate regions of interest by decaying into a series of products and emitting various α-particles, β-particles, γ-rays, neutrons and other nuclei of a wide energy range.

In Chapter 3, the structure and construction of Cascades was discussed in detail along with its ROOT-based analysis package, Melusine. Measures to mitigate background sources for Cascades were discussed, such as passive and active shielding, depth underground, copper electroforming and a radon enclosure that remains at this writing incomplete.

In Chapter 4, the construction of a GEANT4 model of Cascades was presented and validated with a ^{137}Cs calibration source. Simulations of the ^{238}U and ^{232}Th decay chains were performed to predict levels of primordial radiation in Cascades. Additionally, the properties of the $0\nu\beta\beta$-candidate ^{130}Te were discussed. Simulations of its most probable coincident signature (two 536 keV and 1257 keV γ-rays emitted with a strong angular correlation) were presented with sample disks of varying diameter and thickness placed in between the two HPGe arrays.

In the first part of Chapter 5, the simulations of primordial radiation were compared to actual background data from Cascades to analyze the reduction in background due to the copper electroforming process and gauge whether additional sources of primordial activity were present in the detector. Activity levels of ^{238}U and ^{232}Th were quantified by analyzing the following peaks: 911 keV from ^{228}Ac, 583 keV and 2615 keV from ^{208}Tl, 186 keV from ^{226}Ra, and 609 keV and 1764 keV from ^{214}Bi. The analysis discovered levels of about three orders of magnitude higher than the best ICPMS assay of copper electroformed at PNNL of 0.6 μBq/kg in ^{232}Th and 1.3 μBq/kg in ^{238}U at this writing. Although the copper was not electroformed in a clean room environment like MAJORANA, these high levels indicate other small parts, such as plastic, wiring, LFEPs, copper mounts, etc. are contaminated by primordial radiation at higher than desirable levels. These small parts are positioned very close to the crystals, which renders the detection efficiency of the primordials much higher than in reality and gives inaccurate large activities. Other sources of uncertainty are systematic, such as the fact simulations are based on an idealized geometry and the inaccuracy of the Melusine software when fitting peaks of very low intensity. Additionally, the fitting could be skewed by additional background resulting from the cosmic-ray activation of germanium and copper.

In the second part of Chapter 5, sensitivity bounds were placed on measuring the $0\nu\beta\beta$-decay of ^{130}Te to the first 0_1^+ excited state of ^{130}Xe using simulated efficiencies and observed background rates in the 1257 keV and 536 keV regions of interest. Careful analysis revealed the current lower limit of $\tau_{1/2} > 9.4\times10^{23}$ years for the 0ν rate could not be probed, for a best-case scenario experiment running for 10 years revealed a $0\nu\beta\beta$-decay half-life of $\tau_{1/2}$ = 2.68×10^{22} years. The experiment could verify, however, the $2\nu\beta\beta$-decay value of $\tau_{1/2} > 2.3\times10^{21}$ years determined in 2001 by low-background HPGe detectors [13]. The present work developed the techniques that will allow Cascades to be used for the measurement of a number of $\beta\beta$-decay half-lives for decays to the excited states of the daughter isotopes.

6.2. CONTRIBUTIONS

The main contributions of this thesis can be summarized as follows:

- Upper bounds on primordial radiation levels were determined in Cascades, a HPGe multi-crystal array and cryostat constructed with electroformed copper similar to that electroformed for MAJORANA. It was deduced there were some levels of primordial activity present in the smaller parts of Cascades, which could appear higher due to the close position of these small parts to the crystals. More emphasis should therefore be placed on reducing the radioactivity of these small parts, along with more effective screening.

- Parameters of an experiment probing the $0\nu\beta\beta$-decay of ^{130}Te to the first excited 0_1^+ state of ^{130}Xe with Cascades were optimized, with the understanding that the method developed in this thesis can be used for many other $\beta\beta$-decay candidates.

- A successful model of the Cascades detector was built with GEANT4 and is accessible for future simulations of the cryostat, such as for radioactive samples positioned between the two HPGe arrays (with or without angular correlations) and for probing the half-lives of other rare decays.

BIBLIOGRAPHY

[1] C. E. Aalseth, T. W. Hossbach, and H. S. Miley. An improved cooled FET assembly for ultra-low-background germanium spectrometers. In *Nuclear Science Symposium Conference Record, 2004 IEEE*, volume 3, pages 1937 –1938 Vol. 3, October 2004.

[2] E. Aguayo, J.E. Fast, E.W. Hoppe, and et al. The MAJORANA demonstrator.

[3] B. Ananthanarayan and Ritesh K. Singh. Direct observation of neutrino oscillations at the sudbury neutrino observatory. *Current Science*, 83:553, 2002.

[4] E. Andreotti et al. Double-beta decay of ^{130}Te to the first 0^+ excited state of ^{130}Xe with CUORICINO. *Phys.Rev.*, C85:045503, 2012.

[5] Domingo Ricardo Artusa. The CUORICINO neutrinoless double-beta decay experiment to search for the neutrino mass scale. Master's thesis, University of South Carolina, 2004.

[6] F. T. Avignone, R. L. Brodzinski, and Evans Jr. Search for the double-beta decay of ^{76}Ge. *Phys. Rev. C.*, 34:666 – 677, 1986.

[7] Frank. Avignone. Private communication.

[8] Frank T. Avignone. *A Modern Nuclear Laboratory Course*. University of South Carolina Press, 1975.

[9] F. T. Avignone III, G. S. King III, and Yu. G. Zdesenko. Next generation double-beta decay experiments: metrics for their evaluation. *New Journal of Physics*, 7:6, 2005.

[10] Frank T. Avignone III, Steven R. Elliott, and Jonathan Engel. Double beta decay, majorana neutrinos, and neutrino mass. *Reviews of Modern Physics*, 80(2), 2008.

[11] J. N. Bahcall. Neutrinos from the sun. *Scientific American*, 221:22 – 37, 1969.

[12] Iulian Catalin Bandac. *A Search for $2\nu\beta\beta$-Decay to the First Excited 0^+ State of ^{130}Xe with the CUORICINO Detector*. PhD thesis, University of South Carolina, 2006.

[13] A. S. Barabash, F. Hubert, Ph. Hubert, and V. I. Umatov. Search for the double-beta decay of ^{130}Te to excited states in ^{130}Xe. *Physics of Atomic Nuclei*, 65(2):231–234, March 2002.

[14] H. A. Bethe and R. F. Bacher. Nuclear physics a. stationary states of nuclei. *Rev. Mod. Phys.*, 8(2):82, Apr 1936.

[15] R. Brodzinski, H. Miley, J. Reeves, and F. Avignone. Low-background germanium spectrometry: The bottom line three years later. *Journal of Radioanalytical and Nuclear Chemistry*, 193(1):61–70, 05 1995.

[16] R. L. Brodzinski. Low-level gamma-ray spectrometry. *Journal of Physics G: Nuclear and Particle Physics*, 17, 1991.

[17] R. L. Brodzkinski, H. S. Miley, J. H. Reeves, and F. T. Avignone. Low-background germanium spectrometry: The bottom line. *Journal of Radioanalytical and Nuclear Chemistry*, 160(2):355–362, December 1991.

[18] R. L. Brodzkinski, H. S. Miley, J. H. Reeves, and F. T. Avignone. Low-background germanium spectrometry: the bottom line three years later. *Journal of Radioanalytical and Nuclear Chemistry*, 193:61, 1995.

[19] Aalseth C. E. Material purity: Ultra-low background, ICPMS assay, and lead surface preparation for the MAJORANA project.

[20] David O. Cadwell. *Current Aspects of Neutrino Physics*. Springer-Verlag, 2001.

[21] G. L. Cassiday, J. W. Keuffel, and J. A. Thomson. Calculation of the stopping-muon rate undeground. *Phys. Rev. D.*, 7:2022 – 2031, 1973.

[22] The CERN Collaboration. http://root.cern.ch/drupal/.

[23] M. W. Cooper, C. E. Aalseth, D. A. Haas, and et. al. Digital data acquisition graphical user interface. In *Proceedings of the Monitoring Research Review 2010: Ground-Based Nuclear Explosion Monitoring Technologies*, pages 577 – 584.

[24] Aalseth. Craig. Private communication.

[25] Jason A. Detwiler. *Measurement of Neutrino Oscillation with KamLAND*. PhD thesis, Stanford University, 2005.

[26] Guilhem Douysset, Tomas Fritioff, Conny Carlberg, Ingmar Bergström, and Mikael Björkhage. Determination of the ^{76}Ge double beta decay Q value. *Phys. Rev. Lett.*, 86(19):4259–4262, May 2001.

[27] S. R. Elliott and P. Vogel. Double beta decay. *Annual Review of Nuclear and Particle Science*, 52:115, 2002.

[28] Amand Faessler and Fedor Simkovic. Double beta decay. *J. Phys. G: Nucl. Part. Phys*, 24(12):2139, December 1998.

[29] Enrico Fermi. Versuch einer theorie der beta-strahlen i. *Zeitschrift für Physik*, 88:161, 1934.

[30] Ettore Fiorini and et.al. A search for lepton non-conservation in double beta decay with a germanium detector. *Physics Letters*, 25:602–603, 1967.

[31] Richard B. Firestone and Virginia S. Shirley. *Table of Isotopes, Eigth Edition*. Wiley-Interscience, 1998.

[32] Joseph A. Formaggio and C. J. Martoff. Backgrounds to sensitive experiments underground. *Annu. Rev. Nucl. Part. Sci*, 54:361–412, 2004.

[33] Y. Fukuda and et. al. Evidence for oscillation of atmospheric neutrinos. *Physical Review Lettters*, 81(8):1562 – 1567, 1998.

[34] M. Fukugita and A. Suzuki. *Physics and Astrophysics of Neutrinos*. Springer-Verlag, 1994.

[35] W. H. Furry. On transition probabilities in double beta-disintegration. *Phys. Rev.*, 56(12):1184–1193, December 1939.

[36] C. Giunti. Statistical interpretations of the null result of the KARMEN 2 experiment. 1998.

[37] M. Goepert-Mayer. Double beta-disintegration. *Physical Review*, 48:512, 1935.

[38] Paolo Gorla. *Optimization of the CUORE Detector Performance*. PhD thesis, Universit Degli Studi di Milano Bicocca, 2005.

[39] R. N. Hall and T. J. Soltys. High purity germanium for detector fabrication. *IEEE Trans. Nucl. Sci.*, 18:160 – 165, February 1971.

[40] G. Heusser. Cosmic ray-induced background in ge-spectrometry. *Nuclear Instruments and Methods in Physics Research B*, 83:223 – 228, 1993.

[41] G. Heusser. Low radioactivity background techniques. *Annu. Rev. Nucl. Part. Sci*, 45:543 – 590, 1995.

[42] G. Heusser and et. al. Proc. of intern. conf. isotop enviromn. studies.

[43] Todd. Hossbach. Private communication.

[44] Todd W. H. Hossbach. *Improving the Physics Impact of Next-Generation* ^{76}*Ge Neutrinoless Double-Beta Decay Experiments*. PhD thesis, University of South Carolina, 2000.

[45] E. L. Hull, R. H. Phel, J. R. Lathrop, P. L. Mann, R. B. Mashburn, and et. al. P-type point contact germanium detectors for low-level counting.

[46] M. Ivanovich and R. S. Harmon. *Uranium Series Diseequilibirum: Applications to Earth, Marine and Environmental Sciences*. Oxford: Clarendon, 1992.

[47] K. Kazkaz, C. E. Aalseth, and T. W. et. al. Hossbach. Mega: a low-background radiation detector. In *Nuclear Science Symposium Conference Record, 2003 IEEE*, volume 1, pages 87 – 91, 2003.

[48] M. E. Keillor, C. E. Aalseth, A. R. Day, and et. al. Design and construction of an ultra-low-background 14-crystal germanium array for high efficiency and coincidence measurements. *Journal of Radioanalytical and Nuclear Chemistry*, 282:703 – 708, 2009.

[49] M. E. Keillor, C. E. Aalseth, A. R. Day, and et. al. Initial results: An ultra-low-background 14-crystal germanium array. *2010 Monitoring Research Review: Ground-Based Nuclear Explosion Monitoring Technologies*, 2010.

[50] M. E. Keillor, C. E. Aalseth, A. R. Day, and et. al. Cascades: An ultra-low-background germanium crystal array at pacific northwest national laboratory. *AIP Conf. Proc.*, 208:1412, 2011.

[51] M. E. Keillor, C. E. Aalseth, A. R. Day, and et. al. A germanium array for sample measurements: recent results and new analysis methods. *2012 Monitoring Research Review: Ground-Based Nuclear Explosion Monitoring Technologies*, 2012.

[52] H. V. Klapdor-Kleingrothaus and et.al. Neutrinoless double beta decay: Status of evidence. *Foundations of Physics*, 32:1181–1223, 2002.

[53] Glenn F. Knoll. *Radiation Detection and Measurement, Third Edition*. John Wiley Sons, 2000.

[54] D. Lal and B. Peters. Cosmic ray produced radioactivity on the earth. *Handbuch Der Physik*, 46:551 – 612, 1967.

[55] Michael F. L'Annunziata. *Radioactivity: Introduction and History*. Elsevier Science, 2007.

[56] H. S. Miley, R. L. Brodzinski, J. H. Reeves, and et al. Achieving low backgrounds in a variety of situations.

[57] Further Reductions of Radioactive Backgrounds in Electroformed Copper for Ultra-low Background Radiation Detectors. Aalseth, c. e. and farmer, o. t. and fast, j. e. and et. al. *Computer Physics Communications*, March 2001.

[58] J. L. Orrell, C. E. Aalseth, J. F. Amsbaugh, and et. al. Operation of a high purity germanium crystal in liquid argon as a compton suppressed radiation spectrometer. *Nucl.Instrum.Meth.*, A579:91 – 93, 2007.

[59] Marisa Pedretti. *The Single Module for CUORICINO And CUORE Detectors: tests, Construction and Modelling*. PhD thesis, Universit Degli Studi drll'Insubria, 2004.

[60] E. M. Pell. Effect of li-b ion pairing on li+ ion drift in si. *Journal of Applied Physics*, 31:1675, 1960.

[61] Bogdan Povh, Klaus Rith, Christoph Scholz, and Frank Zetsche. *Particles and Nuclei, Fifth Edition*. Springer, 2006.

[62] H. Primakoff and S. P. Rosen. Double beta decay. *Rep. Prog. Phys.*, 22:121, 1959.

[63] Matthew Redshaw, Brianna J. Mount, Edmund G. Myers, and III Avignone, Frank T. Masses of Te-130, Xe-130 and double beta-decay Q-value of Te-130. *Phys.Rev.Lett.*, 2009.

[64] Barabash A. S. Double beta decay experiments: Past and present achievements. *ArXiv e-prints arXiv:hep-ex/0608054 v1*, 2006.

[65] P. A. Sackinger, R. A. Brown, and J. J. Derby. A finite element method for analysis of fluid flow, heat transfer and free interfaces in czochralski crystal growth. *International Journal for Numerical Methods in Fluids*, 9:453 – 492, April 1989.

[66] J. A. Simpson. Elemental and isotopic composition of the galactic cosmic rays. *Annu. Rev. Nucl. Part. Sci*, 33:323 – 382, December 1983.

[67] The GEANT4Collaboration. http://geant4.cern.ch/.

[68] The MAJORANA Collaboration. The proposed MAJORANA ^{76}Ge double-beta decay experiment. http://majorana.pnl.gov.

[69] The MAJORANA Collaboration. The MAJORANA neutrinoless double-beta decay experiment: Pre-conceptual design proposal. http://majorana.pnl.gov.

[70] The MAJORANA Collaboration. Overview of the MAJORANA neutrinoless double-beta decay experiment. Technical report, Brown University, Institute for Theoretical and Experimental Physics, Joint Institute for Nuclear Research, Lawrence Berkley National Laboratory, Lawrence Livermore National Laboratory, Los Alamos National Laboratory, Oak Ridge National LAboratory, Osaka University, Pacific Northwest NAtional Laboratory, Queen's University, Traingle University Nuclear LAboratory, University of Chicago, University of South Carolina, University of Tennessee, University of Washington, 2005.

[71] Kai Vetter. Recent developments in the fabrication and operation of germanium detectors. *Annu. Rev. Nucl. Part. Sci*, 57:363–404, 2007.

[72] Petr. Vogel. Private communication.

[73] G. A. Warren, L. E. Smith, C. E. Aalseth, and et al. Generalized multicoincidence analysis methods. *IEEE Transactions on Nuclear Science*, 53:351 – 355, 2006.

[74] C. F. v. Weizsäcker. Zur theorie der kernmassen. *Zeitschrift für Physik A Hadrons and Nuclei*, 96(7):431–458, 1935.

[75] C. S. Wu, E. Ambler, R. W. Hayward, D. D. Hoppes, and R. P. Hudson. Experimental test of parity conservation in beta decay. *Phys. Rev.*, 105:1413–1415, Feb 1957.